Julius-Maximilians-Universität Würzburg

Fakultät für Biologie

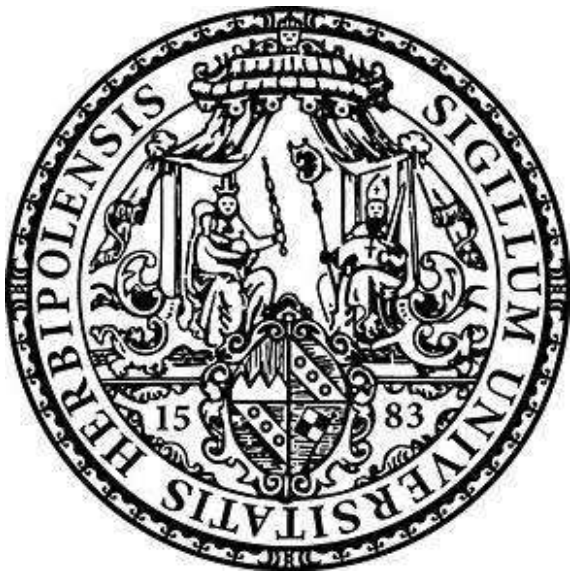

Influence of oncolytic vaccinia viruses on metastases of human and murine tumors

Dissertation

zur Erlangung des naturwissenschaftlichen Doktorgrades der Julius-Maximilians-Universität Würzburg

vorgelegt von Juliane Meir
aus Schleiz

Würzburg, Juli 2015

Eingereicht am: _____

Mitglieder der Prüfungskommission:

Vorsitzender: _____

Erstgutachter: _____
(Prof. Dr. A. A. Szalay)

Zweitgutachter: _____
(Prof. Dr. T. Dandekar)

Tag des Promotionskolloquiums: _____

Doktorurkunde ausgehändigt am: _____

Table of Contents

Summary **1**

Zusammenfassung **4**

1 Introduction **7**

1.1 Cancer 7

1.2 Formation and meaning of lymph node metastases 8

1.2.1 The lymphatic system 8

1.2.2 The metastatic process 10

1.2.3 Cancer stem cells and the epithelial-mesenchymal transition are involved in the metastatic process 12

1.2.4 Metastases as a therapeutic target 15

1.3 Vaccinia virus 16

1.3.1 Vaccinia virus as an oncolytic agent 16

1.3.2 Taxonomy 17

1.3.3 Morphology 18

1.3.4 Replication cycle 19

1.3.5 The VACV isolate LIVP 1.1.1 and recombinant vaccinia virus construct GLV-1h68 21

1.4 Two tumor models as examples of metastatic cancer 23

1.4.1 Cervical carcinoma 23

1.4.2 Melanoma 27

1.5 Aims of this work 30

2 Material **33**

2.1 Chemicals and Enzymes 33

2.2 Buffers and Solutions 35

2.3 Used cell lines and cell culture media 36

2.3.1 Cell lines 36

2.3.2 Cell culture media 36

2.4 Synthetic oligonucleotides 37

2.5 Kits 37

2.6 Antibodies 37

2.6.1 Antibodies for histology ---37
2.6.2 Antibodies for FACS analysis ---38
2.7 Recombinant viral construct GLV-1h68 and the LIVP 1.1.1 clone ...38
2.8 Laboratory animals ...38
2.9 Consumption items ...39
2.10 Equipment ...40
2.11 Software ...41
3 Methods ...42
3.1 Cell biological methods ...42
3.1.1 Culturing of adherent growing cells ---42
3.1.2 Cell Counting via Neubauer hemocytometer ---43
3.1.3 Freezing and thawing of cells ---43
3.2 Virological methods ...43
3.2.1 Infection of different cells lines with Vaccinia Virus ---43
3.2.2 Replication assay ---44
3.2.3 Standard viral plaque assay ---44
3.2.4 Cell viability assay ---45
3.3 Mouse experiments ...46
3.3.1 Subcutaneous (s.c.) implantation of tumor cells ---46
3.3.2 Footpad (f.p.) implantation of B16F10 melanoma cells ---46
3.3.3 Anesthesia of mice with isoflurane ---47
3.3.4 Vaccinia virus injection in tumor-bearing mice ---47
3.3.4.1 Intravenous (i.v.) virus injection ...47
3.3.4.2 Intratumoral (i.t.) virus injection ...47
3.3.5 Injection of IgG ---47
3.3.6 Fluorescence imaging of tumors and metastases ---48
3.4 Analysis of viral titers in tumors and metastases ...48
3.5 Histological analysis of tumors, lymph nodes and organs ...49
3.5.1 Cryosectioning of tumors and lymph nodes ---49
3.5.2 Immunohistochemical staining of cryosections ---49
3.5.3 Agarose sections of lymph nodes and tumors ---49
3.5.4 Immunohistochemical staining of agarose sections ---50

3.5.5 Analyses of digital fluorescence images----------50
3.5.5.1 Quantification of section labeling 50
3.5.5.2 Measurement of fluorescence intensity 50
3.5.5.3 Determination of lymph and blood vessel density 51
3.6 RNA isolation from tumors, metastases and organs and analysis by RT-PCR.....51
3.6.1 RNA isolation ----------51
3.6.2 DNA digestion and RNA concentration measurement----------52
3.6.3 cDNA synthesis----------52
3.6.4 Polymerase chain reaction (PCR) ----------53
3.6.5 DNA agarose gel electrophoresis ----------54
3.7 Preparation of single-cell suspensions and FACS analysis 55
3.7.1 Preparation of single-cell suspensions ----------55
3.7.2 Staining of immune cells in tumor and lymph node single-cell suspensions --------55
3.7.3 Flow cytometric analyses----------56
3.7.4 Determining the growth rate of cells of a single-cell suspension ----------56
3.8 Statistical analysis 56
4 Results 57
4.1 Characterization of metastases formation and virotherapy in the human C33A cervical cancer model 57
4.1.1 Enlarged lymph nodes after subcutaneous implantation of C33A cells----------57
4.1.2 Comparison of GLV-1h68 infection of C33A and C33A-RFP cells in vitro ----------59
4.1.2.1 Insertion of RFP does not impair the replication of GLV-1h68 in C33A–RFP cells..... 59
4.1.2.2 Insertion of RFP does not impair the GLV-1h68-mediated lysis of C33A–RFP cells..... 61
4.1.3 Monitoring of tumor and lymph node metastases formation after subcutaneous implantation of C33A-RFP cells----------62
4.1.3.1 Tumor volume is increasing from week to week after implantation of C33A-RFP cells 63
4.1.3.2 Lumbar and renal lymph node metastases appeared and increased over time according to tumor volume 64
4.1.3.3 Lymph nodes at distant sites can reveal RFP signal..... 65
4.1.3.4 Tumor cells migrate via the lymphatic and haematogenous route 67
4.1.3.5 RFP signal is found in lungs and kidneys confirming the haematogenous spread of tumor cells 69
4.1.3.6 Histological analysis of lungs and kidneys revealing the origin of RFP signal . 70
4.1.4 Combating tumors and metastases with the oncolytic vaccinia virus GLV-1h68 ---72
4.1.4.1 Influence of vaccinia virus GLV-1h68 on C33A-RFP tumors..... 72

4.1.4.2 Influence of GLV-1h68 on C33A-RFP lymph node metastases 74
4.1.4.3 Regression of RFP signal in kidneys after virus administration 76
4.1.5 Tumor and lymph node colonization by GLV-1h68 ----------77
4.1.6 Histological and FACS analysis of C33A tumors and lymph nodes ----------78
4.1.6.1 Higher necrotic areas in tumors compared to lymph nodes 79
4.1.6.2 Higher proliferative status in lymph node metastases compared to primary tumor 79
4.1.6.3 Immune cell status in tumors and lymph node metastases 81
4.1.6.4 Lymph and blood vessel density in tumors and lymph node metastases 82
4.1.6.5 Vascular permeability in tumors and lymph node metastases 84
4.2 Characterization of metastases formation and virotherapy in the murine B16F10 melanoma model 85
4.2.1 Comparison of GLV-1h68 and LIVP 1.1.1 infection of B16F10 cells *in vitro* ----------85
4.2.1.1 Replication of GLV-1h68 and LIVP 1.1.1 in B16F10 cells 85
4.2.1.2 LIVP 1.1.1 lyses B16F10 cells more efficiently than GLV-1h68 87
4.2.2 *In vivo* experiments ----------89
4.2.2.1 Comparison of different implantation techniques: subcutaneous vs footpad 89
4.2.2.2 Comparison of footpad implantation in FoxN1 nude and C57BL/6 mice 92
4.2.2.3 Characterization of tumor and lymph node metastases formation after footpad implantation of B16F10 cells 93
4.2.2.4 Comparison of different virus administration routes: intravenous vs. intratumoral 96

5 Discussion 98

5.1 Characterization of metastases formation and virotherapy in the human C33A cervical cancer model 98
5.1.1 The human cervical cancer cell line C33A as a new metastatic model ----------98
5.1.2 Insertion of RFP in C33A cells has no effects on infection, replication and cell lysis by GLV-1h68 ----------99
5.1.3 C33A-RFP cells form tumors and migrate to lymph nodes after subcutaneous implantation ---------- 100
5.1.4 C33A cells use the lymphatic as well as the haematogenous route of migration 101
5.1.5 Successful therapy of primary C33A-RFP tumors and metastases with the oncolytic vaccinia virus GLV-1h68 ---------- 103
5.1.6 Preferential colonization of primary tumors compared to lymph node metastases by GLV-1h68 ---------- 104
5.1.7 Histological analysis reveal the differences between primary tumor and lymph node metastases ---------- 105
5.1.8 Conclusion ---------- 107

5.2 B16F10 as a promising tool to analyze oncolytic virus therapy in an immune competent mouse model 108

5.2.1 LIVP 1.1.1 is more efficiently infecting, replicating in and lysing B16F10 cells compared to GLV-1h68 in cell culture ---------- 108

5.2.2 Implantation of B16F10 cells into the footpad of immunocompetent C57BL/6 mice as a model to study metastases ---------- 109

5.2.3 Formation of tumors and sentinel lymph node metastases after implantation of B16F10 cells in the footpad ---------- 110

5.2.4 Intratumoral virus injection leads to higher titers in tumors and lymph node metastases compared to intravenous injection ---------- 111

5.2.5 Outlook ---------- 112

6 References 113

7 Appendix 127

7.1 Abbreviations 127

7.2 Danksagung 130

7.3 Eidesstattliche Erklärung 132

7.4 Lebenslauf ..... **Fehler! Textmarke nicht definiert.**

7.5 Publikationsliste 133

Summary

Cancer is one of the leading causes of death worldwide. However, it is supposed, that about 90% of all deaths due to cancer are not caused by the primary tumor, but by the direct and indirect effects of metastases. Therefore, it is of major importance to successfully treat not only the primary tumor, but also metastases. The currently used treatment modalities for metastatic diseases are more or less the same like for the primary tumor. However, tumors and metastases often differ in their properties and therefore, treatment is not always successful. In contrast, those therapeutic agents can even promote formation and growth of metastases. Hence, it is indispensable to find novel treatment options for metastatic disease. One promising candidate represents the oncolytic virus therapy with vaccinia viruses.

The major aim of this work was to analyze two different cell lines regarding their metastatic abilities and finally to investigate whether oncolytic vaccinia viruses are useful therapy options. The cell lines used were the human cervical cancer cell line C33A implanted into immune-compromised mice and the murine melanoma cell line B16F10, implanted into immune-competent mice.

The initial point of the investigations in the first part was the observation of enlarged lumbar und renal lymph nodes in C33A tumor-bearing mice 35 days post implantation of C33A cells subcutaneously into the abdominal flank of immune-compromised nude mice. Subsequently, the presence of human cells in enlarged lymph nodes was demonstrated by RT-PCR using primers specific for human β-actin. To facilitate the monitoring of cancer cell spreading, the gene encoding for the red fluorescence protein (RFP) was inserted into the genome of C33A cells by lentiviral transduction, creating C33A-RFP cells. In cell culture experiments, it was possible to demonstrate that this insertion did not negatively affect the susceptibility of the cells to virus infection, replication and virus-mediated cell lysis. The analysis of the dynamic of the metastatic process in a xenografted mouse model revealed the continuous progression of lumbar (LN) and renal (RN) lymph node metastasis after C33A-RFP tumor cell implantation. Both, the lymph node volume as well as the amount of RFP-positive LNs and RNs was increasing from week to week in accordance with the gain of the primary tumor volume. Moreover, the metastatic spread of cancer cells in lymph vessels between lumbar and renal lymph nodes was

visualized by fluorescence microscopy. Additionally, the haematogenous way of cancer cell migration was demonstrated by RFP-positive cancer cells in blood vessels next to the LN-RN connecting lymph vessel. The haematogenous route of spreading was confirmed by detecting micrometastases in lungs of tumor-bearing mice.

The next step was to investigate whether the recombinant oncolytic vaccinia virus GLV-1h68 is a suitable candidate to cure not only the primary tumor but also metastases. Therefore, GLV-1h68 was systemically injected into C33A-RFP tumor-bearing mice 21 days after tumor cell implantation. It was demonstrated that after another 21 days, the volume of the primary tumor was drastically reduced, and additionally the volume and the amount of RFP-positive lumbar and renal lymph nodes were significantly decreasing compared to the untreated control group. Subsequently, this process was analyzed further by investigating the colonization pattern in the C33A-RFP model. By this, it was shown that first the primary tumor was colonized with highest detectable virus levels, followed by LN and RN lymph nodes. Histological analyses revealed the proliferative status of tumor cells in the tumor and lymph nodes, the amount of different immune cell populations and the vascular permeability in primary tumors and lymph nodes having an influence on the colonization pattern of the virus. Whereby, the vascular permeability seems to have a crucial impact on the preferential colonization of tumors compared to lymph node metastases in this tumor model.

In summary, C33A turned out to be a useful model to study the formation of metastases. Further on, GLV-1h68 was shown to be a powerful tool in fighting primary tumors and metastases in the xenografted C33A model. However, a metastatic model in which the influence of the immune system on tumors and especially on tumor therapy can be analyzed would be preferable. Therefore, the aim of the second part was to establish a syngeneic metastatic mouse model.

Accordingly, the murine melanoma cell line B16F10 was analyzed in immunocompetent mice. First, the highly attenuated GLV-1h68 virus was compared to its parental strain LIVP 1.1.1 concerning infection, replication and cell lysis efficacy in cell culture. LIVP 1.1.1 was more efficient than GLV-1h68 and was subsequently used for following mouse studies. Comparative studies were performed, comparing two different implantation sites of the tumor cells, subcutaneously and footpad, and two different mouse strains, FoxN1 nude and C57BL/6 mice.

Implantation into the footpad led to a higher metastatic burden in lymph nodes compared to the subcutaneous implantation site. Finally, the model of choice was the implantation of B16F10 into the footpad of immune-competent C57BL/6 mice. Furthermore, it was inevitable to deliver the virus as efficient as possible to the tumor and metastases. Comparison of two different injection routes, intravenously and intratumorally, revealed, that the optimal injection route was intratumorally. In summary, the murine B16F10 model is a promising model to study the effects of the immune system on vaccinia virus-mediated therapy of primary tumors and metastases.

Zusammenfassung

Weltweit ist Krebs eine der häufigsten Todesursachen des Menschen. Allerdings wird angenommen, dass ca. 90 % dieser Todesfälle nicht auf den Primärtumor zurückzuführen sind, sondern durch den direkten und indirekten Einfluss von Metastasen verursacht werden. Deshalb ist es wichtig, eine Therapieform zu wählen, die sowohl den Primärtumor als auch Metastasen bekämpft. Bei den derzeit eingesetzten Behandlungsmethoden für Metastasen handelt es sich weitestgehend um die gleichen Therapieformen die auch zur Bekämpfung des Primärtumors eingesetzt werden. Allerdings unterscheiden sich Primärtumor und Metastasen häufig in ihren Eigenschaften, weshalb die Therapie oft keinen Erfolg bei Metastasen zeigt und im schlimmsten Fall sogar deren Neubildung und Wachstum fördern kann. Deswegen ist es von immenser Bedeutung, neue Therapieformen zu entwickeln, die speziell auch auf die Wirksamkeit gegen Metastasen zugeschnitten sind. Eine vielversprechende Möglichkeit hierfür stellt die onkolytische Virustherapie dar.

Das Hauptziel dieser Arbeit war es, zwei verschiedene Tumorzelllinien hinsichtlich ihrer metastatischen Fähigkeiten zu untersuchen und anschließend zu überprüfen, ob onkolytische Vaccinia-Viren zur Therapie dieser Metastasen beitragen können. Bei den hierfür untersuchten Zelllinien handelte es sich um die menschliche Zervixkarzinomzelllinie C33A, implantiert in immunsupprimierte Mäuse und um die murine Melanomzelllinie B16F10, implantiert in immunkompetente Mäuse.

Ausgangspunkt der Untersuchungen im ersten Teil der Arbeit, bildete die Beobachtung, dass nach der subkutanen Implantation von C33A-Zellen in die abdominale Flanke von immunsupprimierten Nacktmäusen die lumbalen und renalen Lymphknoten der tumortragenden Mäuse vergrößert waren. Die Untersuchung dieser vergrößerten Lymphknoten mittels RT-PCR, unter zu Hilfenahme von spezifischen Primern für humanes β-Aktin, wies tatsächlich humane Zellen in allen lumbalen und der Hälfte der renalen Lymphknoten nach. Darum sollte im nächsten Schritt das metastatische Verhalten dieser Zellen genauer untersucht werden. Hierfür wurde mittels lentiviraler Transduktion, das für das rotfluoreszierende Protein kodierende Gen in C33A-Zellen integriert. In Zellkulturexperimenten konnte nachgewiesen werden, dass die Insertion sich nicht negativ auf die Infektion, Replikation und Zelllyse der Viren

auswirkte. Anschließende Mausexperimente zeigten den Verlauf der Metastasierung der lumbalen und renalen Lymphknoten. Sowohl das Volumen als auch die Anzahl an RFP-positiven Lymphknoten nahm nach Implantation von Woche zu Woche zu und korrelierte mit der Zunahme des Primärtumorvolumens. Darüber hinaus konnte die Migration der Tumorzellen in Lymphgefäßen zwischen dem lumbalen und renalem Lymphknotenpaar mit Hilfe der Fluoreszenzmikroskopie sichtbar gemacht werden. Zusätzlich konnte die Metastasierung über die Blutbahn nachgewiesen werden, da sich RFP-positive Zellen in dem Blutgefäß neben dem Lymphgefäß, das die lumbalen und renalen Lymphknoten miteinander verbindet, befanden. Die hämatogene Verbreitung wurde auch dadurch bestätigt, dass in den Lungen der tumortragenden Mäuse Mikrometastasen detektiert werden konnten.

Im nächsten Schritt wurde untersucht, ob das rekombinante Vaccinia-Virus GLV-1h68 in der Lage ist, nicht nur den primären Tumor zu bekämpfen, sondern auch Metastasen. Dafür wurde tumortragenden Mäusen systemisch eine einzelne Dosis GLV-1h68 21 Tage nach Tumorzellimplantation injiziert. Daraufhin reduzierte sich nicht nur das Volumen des Primärtumors innerhalb von weiteren 21 Tagen auf die Ausgangsgröße, sondern auch das Volumen und die Anzahl der RFP-positiven lumbalen und renalen Lymphknoten nahm ab, im Vergleich zur unbehandelten Kontrolle. Die Analyse der Kolonisierungsdynamik von Primärtumor und Metastasen durch GLV-1h68 zeigte, dass zuerst der Primärtumor kolonisiert wurde, gefolgt von LN und RN. Des Weiteren war der virale Titer in Tumoren zu jedem Zeitpunkt höher als in den metastasierten Lymphknoten. Histologische Untersuchungen des tumorösen Gewebes zeigten, dass der proliferative Status der Tumorzellen, die Menge verschiedener Immunzellpopulationen und die vaskuläre Permeabilität einen Einfluss auf die Kolonisierung durch GLV-1h68 haben. Dabei wird angenommen, dass vor allem die vaskuläre Permeabilität den größten Einfluss auf die Kolonisierungsreihenfolge hat.

Zusammenfassend kann gesagt werden, dass C33A ein hilfreiches Model ist, um die Bildung von Metastasen sowie die onkolytische Virustherapie dieser in einem immunsupprimierten Model zu untersuchen. Aus klinischer Sicht allerdings wäre es wünschenswert, ein Model zu haben, in dem auch der Einfluss des Immunsystems auf die Tumortherapie untersucht werden kann. Deswegen war das Ziel im zweiten Teil der Arbeit die murine Melanomazelllinie B16F10 im immunkompetenten Mausmodell als metastatisches System zu etablieren. Als erstes wurde in

Zellkulturexperimenten überprüft, wie geeignet GLV-1h68 ist, um die murinen Zellen zu infizieren, in ihnen zu replizieren und sie anschließend zu lysieren und mit dem parentalen Virus LIVP 1.1.1 verglichen. Dabei stellte sich heraus, dass LIVP 1.1.1 effizienter und geeigneter ist als GLV-1h68. Deswegen wurde in weiteren Versuchen das parentale Virus LIVP 1.1.1 verwendet. Bevor diese Experimente durchgeführt wurden, wurden Studien durchgeführt, bei denen 2 verschiedene Implantationsstellen, subkutan und in die Fußsohle, und 2 verschiedene Mausstämme, FoxN1 nude und C57BL/6, verglichen wurden. Dabei stellte sich heraus, dass nach Implantation in die Fußsohle mehr Lymphknotenmetastasen entstanden als nach subkutaner Implantation. Im weiteren Verlauf wurde die Implantation von B16F10-Zellen in die Fußsohle von C57BL/6-Mäusen bevorzugt, um eine verlässliches Metastasenmodel zu generieren. Im Folgenden wurden zwei verschiedene Injektionswege untersucht, intravenös und intratumoral, wobei sich die intratumoral Injektion als geeigneter erwies, um effizient so viel Virus wie möglich in Tumore und Metastasen zu bringen. Generell handelt es sich hierbei um ein geeignetes Model, um die Wirkungen des Immunsystems auf Vaccinia-Virus-vermittelte Therapie von Primärtumor und Lymphknotenmetastasen zu untersuchen.

1 Introduction

1.1 Cancer

Cancer is one of the leading causes of morbidity and mortality worldwide, with approximately 14 million new cases and 8.2 million cancer-related deaths in 2012.[1] In Germany there are 500,000 new cases of cancer and 221,000 cases of death per year.[2]

Cancer is no distinct disease pattern but a general term for malignant tumors and neoplasms, which can occur in almost every part of the body.[1] However some parts are more effected than others, among them: lung, liver, stomach, gastrointestinal tract, breast and esophagus. There are also gender-specific differences. Men are often affected by prostate cancer while breast and cervical cancer are among the leading cancer forms in women. In general, there are three different types of cancer: carcinomas are derived from epithelial cells, while sarcomas develop from cells originating in the mesenchyme.[3] Both types of cancer are forming solid tumors, while leukemia and lymphoma (the third type of cancer) arise from hematopoietic cells and are therefore non-solid.

There are different reasons for cancerogenesis, like the lifestyle or the environment of a person. For example nutrition, smoking, drinking alcohol as well as ultraviolet radiation (UVR) are increasing the risk to develop cancer.[4–7] Other factors are microorganisms like bacteria and viruses. It is known that there is a correlation between *Helicobacter pylori* infection und gastric cancer, between *human papilloma virus (HPV)* and cervical cancer or between hepatitis C virus and liver cancer.[8–10] Only a small amount of affections are due to familial or genetic dispositions which do sometimes lead to tumors even in newborns.

Generally, malignant tumors arise by accumulation of progressive genetic abnormalities. The affected genes can be divided into two categories: proto-oncogenes and tumor-suppressor genes. Proto-oncogenes encode for proteins which affect cell growth, cell division and differentiation and become cancerous oncogenes by mutation.[11] This results in permanent activation and increased expression of the gene product. Among them are signal transduction proteins, cellular growth factors and their receptors as well as transcription factors. These mutations are so called “gain-of-function mutations”. They are dominant, that means one mutated allele is sufficient to induced uncontrolled cell growth and division. In contrast to

oncogenes tumor-suppressor genes are recessive, which means both alleles must be mutated. In this case it is a “loss-of-function mutation”, leading to a dampening or repressive effect on the regulation of the cell cycle, promotion of apoptosis or regulation of DNA repair.

During carcinogenesis cells accumulate corresponding mutations and therefore acquire different tumor cell characteristics, called the “hallmarks of cancer”.[12] These include a high proliferation rate induced by independency of external growth-stimulatory signals and insensitivity towards growth-inhibition factors. Furthermore resistance to cell death as well as enabled replicative immortality contributes to uncontrolled cell division. Nutrition and oxygen supply is provided by tumor-induced angiogenesis. Additionally, tumor cells are able to invade surrounding tissue and metastasize to distant organs and lymph nodes. Other hallmarks are the reprogramming of energy metabolism and evading the immune system.

The treatments used for cancer therapy depends upon the type, location, and grade of cancer as well as the person's health and wishes. The main options are surgery, chemotherapy and radiation for both, primary tumors and metastases. But these therapies often have limitations and severe side effects. Therefore enormous effort is put into the development of novel therapeutic agents and innovative approaches are currently under investigation in preclinical and clinical studies. The most prominent novel therapies include targeted molecular therapies, anti-angiogenic therapies, immuno-therapies, gene therapies or the use of oncolytic viruses.

1.2 Formation and meaning of lymph node metastases

1.2.1 The lymphatic system

The lymphatic system is part of the immune system and consists of primary and secondary lymphatic organs and of a network of thin walled lymphatic vessels which carries the lymph. The only primary lymphatic organ is the thymus.[13] The thymus is the place where T lymphocytes mature and proliferate. The secondary organs are lymph nodes, the spleen, tonsils and mucosa-associated lymphoid tissue (MALT). Those organs maintain mature naive lymphocytes and initiate an adaptive immune response by antigen activation of lymphocytes. The lymphatic circulation begins with blind ending highly permeable lymph capillaries which are abundant in the dermis of the skin and in connective tissue. Here, they take up extravagated tissue fluid by an increase of interstitial fluid pressure. The lymph contained in capillaries is then drained into

pre-collector lymphatic vessels and further via the sieving mechanism of the lymph nodes into larger lymphatic collecting vessels.[14] Finally, the fluid, as well as interstitial proteins and cells, are transferred back into the venous circulation via the thoracic duct.[15] The thoracic duct is the largest and most important lymphatic vessel and is the main connection between the lymph and the blood system.

Lymph nodes are an important part of the lymphatic system. They are kidney or oval shaped and range in size from a few millimeters to about 1–2 cm. Their amount ranges from approximately 300-700 nodes in the human body. Large amounts can be found in the inguinal region, behind the ear, axillary or along the aorta. Their function is the filtration of lymph fluid and they operate as collecting stations for antigens. The nodes next to an organ, the first filter station, are called regional lymph nodes. From there, the fluid flows to collecting lymph nodes. The regional nodes are normally those which get first metastasized in a person suffering from cancer. They are therefore called sentinel or draining lymph nodes.

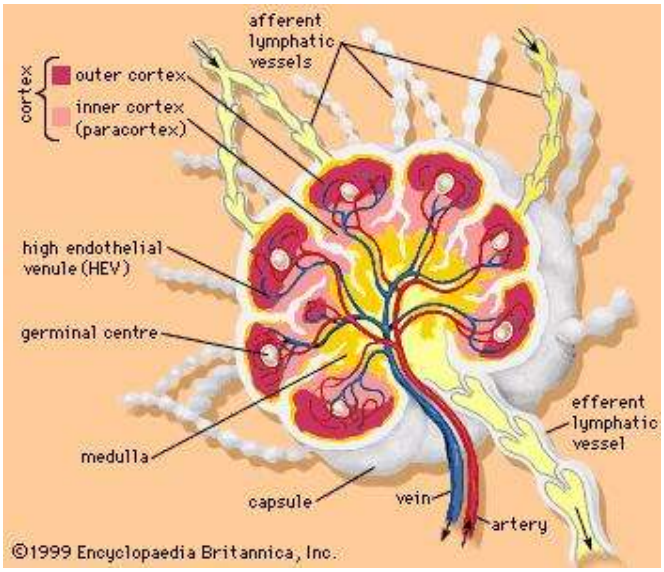

Figure 1-1 Lymph node structure: The lymph enters the lymph node via the afferent lymphatic vessels. Afterwards the lymph is channeled around, across the parenchyma and towards a medullary network of sinuses. Finally the lymph leaves the node via the efferent lymphatic vessel, located at the hilus. This is the venue where an afferent and an efferent blood vessel penetrate the capsule as well (taken from [16]).

The structure of a lymph node can be seen in Figure 1-1. The lymph node is surrounded by a capsule composed of collagenous tissue and inside, the capsule extends to form trabeculae, subdividing the node in small compartments.[17] Histologically, the lymph node can be divided into two parts: the cortex and the medulla. The cortex can be further divided into the

paracortex (the T cell area), and the more superficial B cell area that consists of primary follicles and (after antigen challenge) germinal centers.[18] The medulla is a labyrinth of lymph-draining sinuses, which are parted by medullary cords. They contain many plasma cells as well as some macrophages and memory T cells. The lymph enters the node through one of the several afferent lymph vessels (*Vasa afferentia*) into the sub-capsular sinus. Afterwards the lymph is channeled around, through trabecular sinuses, across the lymph node parenchyma and towards a medullary network of sinuses. Finally the lymph leaves the node through an efferent lymph vessel (*Vas efferens*) at the hilus, the venue where also an afferent and an efferent blood vessel penetrates the capsule.

1.2.2 The metastatic process

The ability to metastasize is a hallmark of malignant tumors. Metastasis is a complex multistage process whereby malignant tumor cells spread from the tumor origin throughout the body and establish new colonies in organs at a distant site.

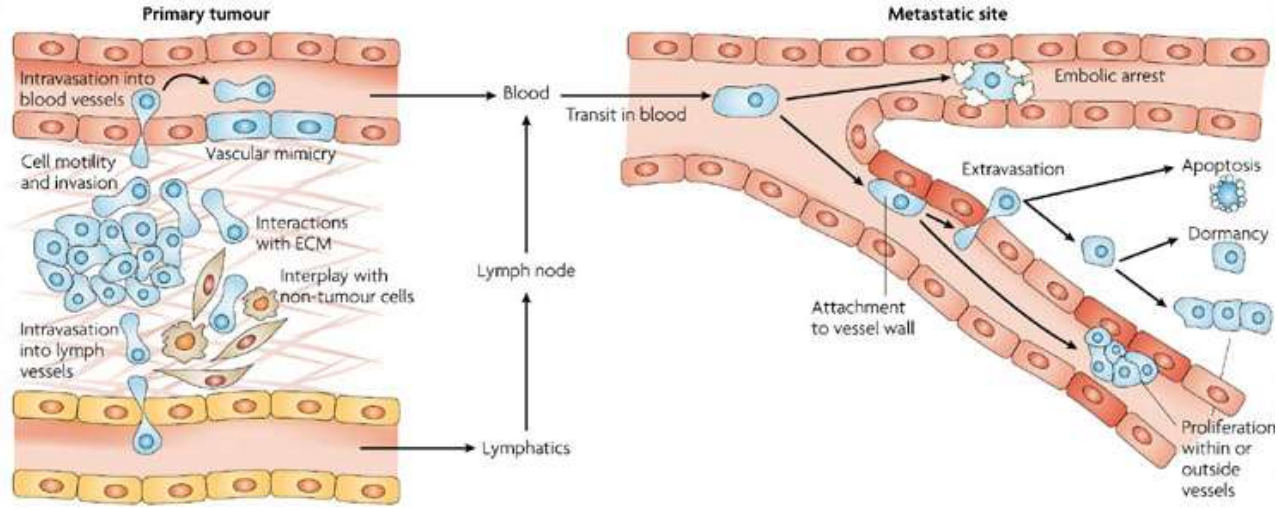

Figure 1-2 The Metastatic process: A tumor cell, which initiates a new metastatic colony must first detach from the primary tumor mass and invade the local host tissue stroma. Here, the tumor cell interacts with the extracellular matrix (ECM) and non-tumor cells. Cells can either enter lymph vessels and are then transported to regional lymph nodes or they enter blood vessels and are transported to other organs. At the metastatic site the cells become arrested in capillaries or venules of the affected organ and extravagate into the surrounding parenchyma. Here, the cells need to adapt to the new micro-milieu or change to environment to suit their own needs. Finally they divide to form new metastases (taken from Sahai *et al*. [19]).

In general there are three different major routes of metastatic spread: the lymphatic route via lymph vessels, the haematogenous route via blood vessels, and the transcoelomic spread via

body cavities. Additionally, some types of cancer, e.g. pancreatic cancer, head and neck cancer and prostate cancer can infiltrate along nerves.[20,21] By the lymphatic spread tumor cells migrate through the lymph to lymph nodes and ultimately to other parts of the body. This is typically the beginning of dissemination of carcinomas, while haematogenous metastases occur at later time points.[22] In contrast, sarcomas preferentially spread via blood vessels. The transcoleomic dissemination via the peritoneal or ascitic fluid is a feature of only a small group of tumors, including ovarian carcinomas or nephroblastoma.[23,24]

The multistage process of metastasis is seen in Figure 1-2.[19,22,25,26] The first step of this procedure is the detachment of tumor cells from the primary tumor. This is promoted by the reduction of intercellular adhesion due to a loss of E-cadherin, a direct mediator of cell–cell adhesive interactions. Disrupting the expression of E-cadherin led to early invasion and metastasis in a pancreatic carcinoma model in a transgenic mouse model.[27] The next step for tumor cells is to invade the local host tissue stroma. Thereby they interact with extracellular matrix (ECM) components such as collagen fibers and interplay with non-tumor cells including fibroblasts and macrophages. Those interactions are primarily mediated by integrins and help to form a path for migration. Afterwards, tumor cells enter the circulation by penetrating local lymphatic and blood vessel. This process is facilitated by formation of new angiogenic and lymphatic vessels mediated by the tumor. Carcinomas first invade lymph vessels and form lymph node metastases while haematogenous metastases occur later on. Sarcoma cells directly migrate through blood vessels. Within the vessels the tumor cells have to survive different challenges, amongst others, shear stress and interaction with leukocytes. Fidler *et al*. demonstrated that only 1% of all tumor cells survive longer than 24 hours within the blood circulation.[28] Arrived at the metastatic site the tumor cells can either arrest as emboli in narrow vessels or they can attach to the vessel wall. Here, they either extravagate and enter the parenchyma of the new organ, or in some cases the tumor cells proliferate within the vessel and the increased mass of cells promote the disruption of the endothelium and tumor cells enter the surrounding tissue.[29] Once reached the parenchyma many cancer cells undergo apoptosis and some enter the state of dormancy, thus metastases occur many years after tumor removal.[30] This has to be taken into account concerning tumor therapy. However, some tumor cells directly form new colonies including formatting a vascular network and creating a microenvironment promoting their survival and proliferation.

Tumor cell movement is driven by different factors. The first factor is physically. The interstitial pressure in tumors is significantly higher compared to that in normal tissues, so the fluids flow from the tumor into vascular vessels in the surrounding tissues.[31] Within the lymph tumor cells are transported to regional lymph nodes where they can form metastases. Another important factor is chemokine-receptor-mediated chemotaxis. One example is the chemokine CCL21 which is expressed by lymphatic vessels.[32,33] Receptors for this ligand are CCR7 and CXCR4 which are expressed on metastatic cells of many carcinomas, e.g. breast carcinoma.[34] Indeed, the presence of CCR7 on metastatic cells strongly correlates with the incidence of lymph node metastases, indicating a receptor-ligand interaction resulting in cell migration. This process is a paracrine chemotaxis. However, an autocrine chemotaxis has been described as well.[33] CCR7-positive cells are able to secret CCR7 ligands supporting the migration of more CCR7-positive tumor cells in direction of lymph vessels. Both, the paracrine as well as the autocrine chemotaxis are important processes involved in tumor cell migration.

Although, theoretically tumor cells can reach every distant organ by travelling via lymph and blood vessels, usually metastases occur at typical sites dependent on the type of tumor. Already in 1889 Paget discovered in 735 women with breast cancer *post mortem* that the organ distribution of metastases was non-random.[35] Hence, he suggested that metastasis is not a random event. Instead he developed the “seed and soil” hypothesis. That means, some tumor cells (the seed) grow preferentially in a special microenvironment of selected organs (the soil). Therefore, metastases only arise when the suitable seed is implanted into the appropriate soil. Although, this was confirmed by Sugarbaker who injected tumor cell suspension from different types of tumors into the same site in rats and observed that each tumor type established its own pattern of metastases,[36] the hypothesis is not true for all kinds of tumor.[37]

1.2.3 Cancer stem cells and the epithelial-mesenchymal transition are involved in the metastatic process

It is supposed, that both, cancer stem cells (CSC) as well as the epithelial-mesenchymal transition (EMT) are playing a major part within the metastatic process.

The cancer stem cell model of tumors indicates that there is a small subset of cancer cells, the CSCs, which are supposed to be self-sustaining with the ability to self-renew and sustain tumor growth.[38] The main features of those CSCs are continuous regeneration, pluripotency,

tumorigenicity and their rare appearance. Continuous regeneration means that CSC can undergo a symmetrical self-renewing cell division, resulting in identical daughter stem cells that retain self-renewal capacity, making the cell line immortal. Pluripotency is the asymmetrical self-renewing cell division causing one stem cell and one more differentiated daughter cell, which share similar features with the tissue of origin. This accounts for both, the similarity between tumors and the tissue of origin as well as the heterogeneous phenotype of many tumors. Those daughter cells (non-CSCs) are dividing with a higher frequency and account therefore for the main part of tumor mass. Tumorigenicity is the ability that one single CSC is supposed to be enough to operate as a germ cell to form a malignant tumor. This is not true for non-CSCs. However the percentage of CSC on the whole tumor mass is very small. Another feature characterizing CSCs is their high resistance against exogenous agents, such as cytostatic drugs or radiation.[39]

The epithelial-mesenchymal transition is a process by which epithelial cells lose their cell-cell adhesion, and gain migratory and invasive properties and by this acquire a mesenchymal phenotype. This is a very important process in early embryonic development and plays also a key role during cancer invasion and metastasis.[40] By now three different types of EMT are known. [41] The first two types happen during embryogenesis and after organogenesis, respectively. Type 3 EMT is part of the metastatic process, whereby epithelial carcinoma cells leave a primary tumor nodule, migrate to a new tissue site, and reform as a secondary tumor nodule. Recently the connection between EMT and CSC has been discovered. The EMT program results in the development of tumor cells with a migrating phenotype and CSC characteristics, like tumorigenicity and resistance against therapeutic agents. This was so far confirmed by several groups.[40,42,43]

In Figure 1-3 the hypothesis about the involvement of EMT and migrating CSCs (MCSCs) in the metastatic process is pictured, demonstrated on colon cancer as an example. Brabletz *et al*. postulate, that the initial step of metastasis is the induction of EMT by aberrant signals.[44] By induction of EMT so-called migrating cancer stem cells develop, which display an invasive phenotype and stem cell characteristics. Those MCSCs can dissociated from the tumor mass, invade the lymphatic or blood circulation and form new colonies in distant organs. The MCSC concept might be the explanation for a lot of established facts.

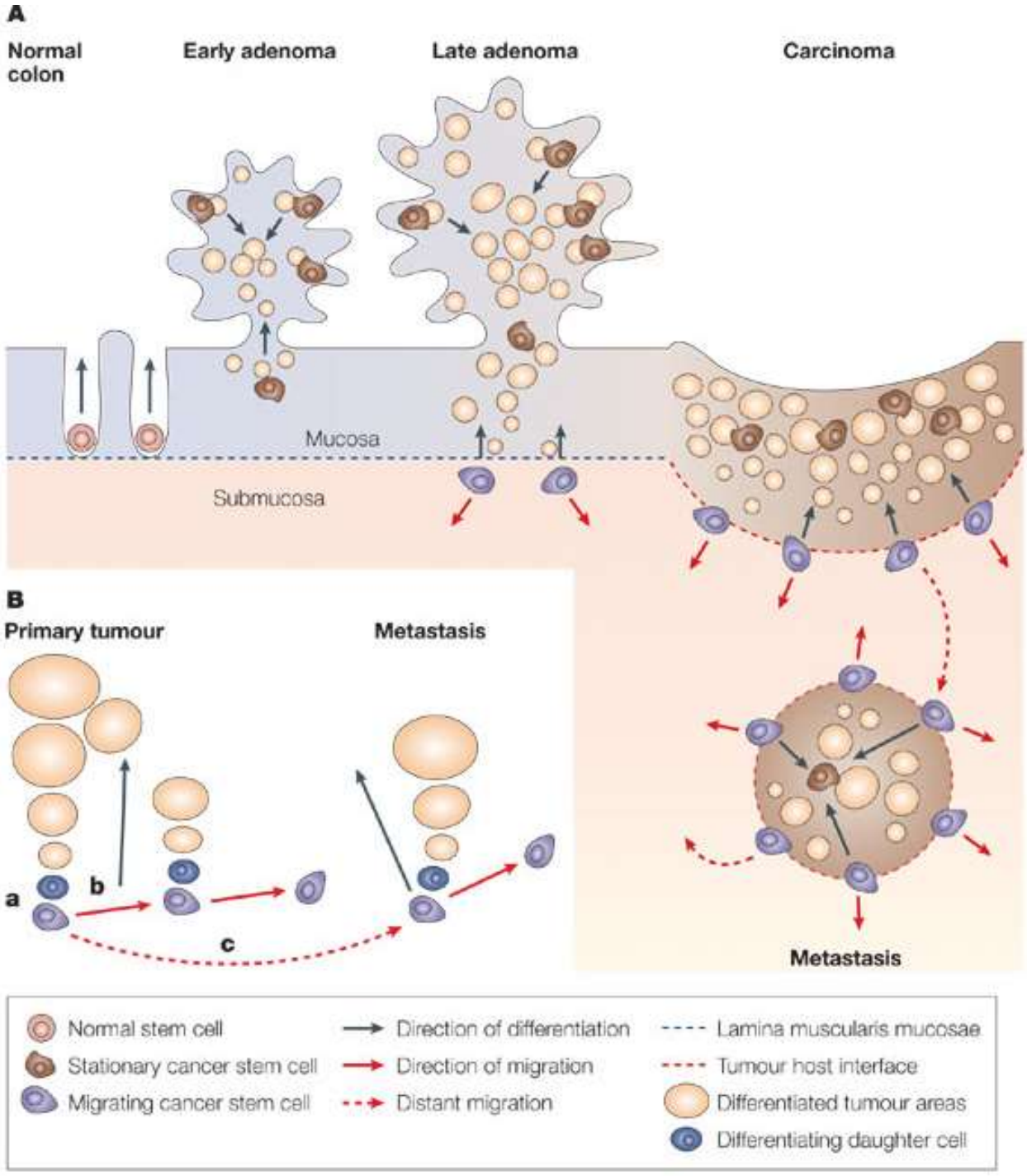

Figure 1-3 Hypothesis about involvement of EMT and MCSCs in the metastatic process (example colon carcinoma): [A]. Normal stem cells are located in basal crypt areas of normal mucosa. By induction of EMT in tumor cells, including stationary cancer stem cells (SCSCs), tumor cells become mobile migrating cancer stem cells (MCSCs) which finally form metastases. [B] Potential function of MCSCs in carcinomas (primary tumor) and metastases: **a**. MCSC divides asymmetrically, producing one daughter cell which starts proliferation and differentiation. **b.** The remaining MCSC either migrates a short distance before undergoing a new asymmetric division, adding mass to the primary tumor **c.** or starts long-distance dissemination through blood or lymph vessels to produce a metastasis after subsequent asymmetric division at its new location. Therefore the basic mechanisms are the same for primary carcinomas and metastases (Taken from Brabletz *et al*. [44]).

Like seen in Figure 1-3 benign colon adenomas grow within the mucosa layer, and detachment of single tumor cells and EMT are not apparent. This is indicating that adenomas are unlikely to have MCSCs and therefore this would be an explanation why adenomas do not metastasis. EMT first becomes evident during the transition of adenoma to carcinoma when the tumor crosses the boundary of the lamina *muscularis mucosae* and metastases first appear from this stage onwards. Furthermore, the amount of CSCs in the tumor correlates with the strength of EMT induction and this is strongly connected to the incidence of metastases and survival. Most of the CSCs are located at the tumor-host interface. When a metastasis is growing, a new tumor is arising, which generally imitates the morphology of the primary tumor. That means, based on the MCSC-model, either the MCSCs are dividing asymmetrically at the site of metastasis or the EMT-process is inverted. This is called the mesenchymal-epithelial transition (MET).[45] The result in both cases is the development of differentiated non-CSCs, making up the main part of metastasis´ tumor mass due to their high proliferation rate.

All in all the CSCs and EMT play an important part in the metastatic process and should therefore be taken into consideration in tumor therapy, especially due to the high resistance of CSCs against exogenous agents. Therefore a main focus has to be put on the development of therapeutics against CSCs and EMT to successfully reduce the metastatic burden. First studies are ongoing to identify therapeutic agents especially for CSCs.[46]

1.2.4 Metastases as a therapeutic target

Like already mentioned in chapter 1.1, 8.2 million people die from cancer every year worldwide. It is estimated that more than 90% of deaths are due to the direct or indirect effects of metastases.[47,48] Although, lymph node metastases are rarely life-threatening they are important for staging the disease and therefore, incidence of metastasis is strongly connected to patient´s prognosis. So the main attention has to be put on metastases when thinking about a successful therapy of advanced tumors. Unfortunately, tumor therapy can promote growth of metastases even more instead of suppress metastatic formation. One example for this is adjuvant radiotherapy which is used for local growth control. However, this can promote metastasis via the tumor bed effect, which means that tumors recur at the irradiated site, associated with high metastasis incidence and poor prognosis.[48,49]

Nevertheless, treatment for metastatic cancer is currently comparable to those used for primary tumors and includes mainly radiation and chemotherapy while surgery is hardly performed on metastatic lesions.[48] This is due to the assumption that metastases are similar to primary tumors and tumor growth control is also effectively suppressing metastatic formation. However, current research revealed that there are rather extreme molecular differences between metastases and primary tumors.[50] Therefore, therapy is often not effective against metastases and has to be more adapted to metastatic properties.

One new approach is the application of nanoparticles.[51] Those nanoparticles can be used as carriers for small-molecule drugs or biomacromolecules, like proteins or small interfering RNA (siRNA) [52–55] or they can be used for thermoablative therapy (the heating of tissue in order to kill tumor cells) by activating nanoparticles, located in the diseased tissue by magnetic fields or infrared light.[56,57] Those nanoparticles can be used to target all three sites: the primary tumor, the organ affected by metastases and also moving cancer cells. Different particles have already reached the clinics, for example, protein nanoparticles containing paclitaxel are approved to treat metastatic breast cancer.[58] Another example is the inhibition of tumor lymph angiogenesis and therefore lymphatic metastases, for example by down-regulation of lymphangiogenic cytokines and/or their interaction with receptors.[59] The disadvantage is that those therapies may only be suitable at an early stage of disease before metastases have been developed.

Another point which has to be considered in fighting metastases is that in many cases they first have to be discovered before appropriate therapy is possible. Here, oncolytic viro therapy might be a new innovative tool. The aim is that after one single intravenous administration the virus would accumulate exclusively in all tumors cells/tissues, replicate there and destroy everything, the primary tumor, metastases and circulating tumor cells. Therefore, exact previous diagnosis is not necessary any more.

1.3 Vaccinia virus

1.3.1 Vaccinia virus as an oncolytic agent

Vaccinia virus (VACV) is known for a long time in medical history. In 1796 Edward Jenner, an English physician and scientist, discovered that cow pox can protect people from human pox after inoculation into the skin.[60] He called this process *vaccination* and the material he used

vaccine both coming from the Latin word *vacca* which means cow. Ever since the virus was investigated very well and in the 20th century the virus was used by the WHO in a worldwide smallpox eradication program until the pox were officially declared eradicated in 1980.[61] Consequently, the virus is very well characterized and a lot is known about its biology and pathogenesis including its behavior in humans.[62]

The vaccinia virus has many advantages that make it a safe and promising oncolytic agent. First of all the viral DNA is not integrated into host DNA because the virus replicates exclusively in the cytoplasm in mini-nuclear structures called viral factories.[62] Second, the large genome and strong promoters enable it to express at least up to 25,000 base pairs of foreign DNA, so the expression of multiple transgenes becomes possible.[63] Third, they replicate and lyse cells rapidly compared with other virus species releasing as many as 10,000 IMV particles within 24 hours.[64] Forth, wild-type VACV has been shown to have a natural tropism for tumor cells while leaving healthy tissue unharmed, which might at least in part rely upon a leaky tumor vasculature, possibly necessary for the extravasation of virions into tissues.[65]

Generally, there are three different ways to use the virus as an agent to fight cancer. One possibility is to use the virus as a vector to specifically insert therapeutic genes in tumor cells. One example is a vaccinia virus, carrying the tumor suppressor gene p53.[66] The next way is using the virus as a vector for cancer immunotherapy.[64] The goal is to stimulate immune responses which target and eliminate existing tumor cells as well as establish a long-term antitumor memory. The last possibility is the direct lyses of infected tumor cells. Premise is that the virus efficiently infects exclusively tumor cells replicates within and lyses the cells. Specificity can be increased by the deletion of different genes, e.g. thymidine kinase, which is described in detail in chapter 1.3.5.

1.3.2 Taxonomy

Vaccinia virus belongs to the family of *Poxviridae.* Those viruses are double-stranded DNA viruses which replicate exclusively in the cytoplasm. They can be divided into two subfamilies: the *Chordopoxvirinae* which infect vertebrates and the *Entomopoxvirinae* which solely infect insects.[67] The subfamily *Chordopoxvirinae* can be subdivided into eight genera, comparable in morphology and host tropism. Of main importance for humans are *Orthopoxviridea*. Two representatives of these genera are the exterminated human pathogen Variola virus, which

caused the small pox, and the vaccinia virus, which was used in the variola virus vaccinie and is now a widely used model virus in laboratories.[68]

1.3.3 Morphology

The brick-shaped vaccinia virus particles are approx. 300 x 240 x 120 nm in size and belong to the largest known DNA viruses.[64] The genome consists of a linear double-stranded DNA of approx. 192 kbp length, encoding for about 200 genes, and is associated with a number of virus-encoded proteins, including RNA polymerase, enzymes for RNA capping, methylation and polyadenylation and a transcription factor.[64]

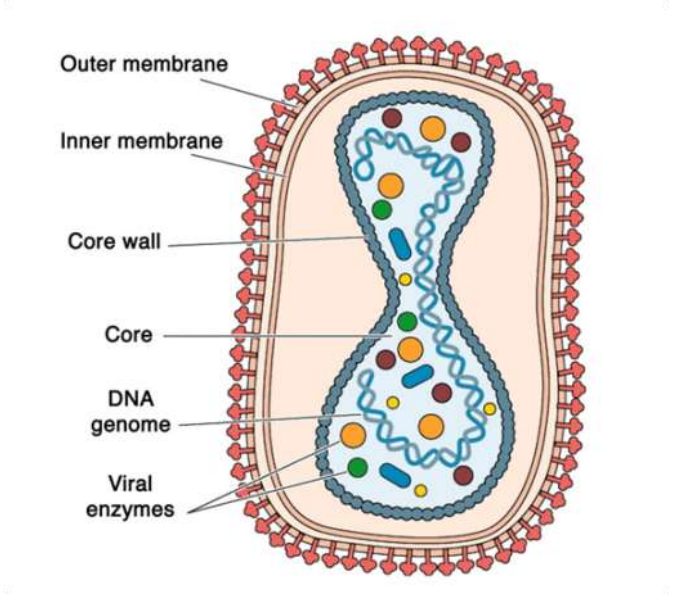

Figure 1-4 Morphology of a IMV particle of vaccinia virus: The IMV is surrounded by a single membrane layer. Inside the virion the nucleus is located, containing the viral genome and viral proteins (taken from Harrison *et al*. [67]).

During the vaccinia virus replication cycle a distinction between four different types of virions, which differ in structure, function, localization within the cell and in the produced amount, can be made.[68] As seen in Figure 1-4 the brick-shaped IMV (*intracellular mature virus*) has a single lipid double layer with more than 12 different viral proteins surrounding the core including the viral genome and enzymes. By lyses of infected cells those infectious IMV are released. They spread within the organism and also from host to host. Within infected cells, some of those viral particles are wrapped by a double layer of intracellular membranes derived from the early endosomes or trans-golgi network to form IEV (*intracellular enveloped virus*).[68,69] Bound to microtubules the IEV move to the cell surface where the outer viral membrane fuses with the

cytoplasm membrane, revealing a cell associated viral particle, the CEV (*cell-associated enveloped virus*). Important for cell-to-cell spread is the actin tail formation induced by the CEVs which drive the virion away from the cell.[69] CEVs are identical to EEVs (*extracellular enveloped virus*) except that latter are released from the cell surface. EEVs are responsible for infection and spreading from cell to cell and from host to host as well (as seen in Figure 1-5).[68]

1.3.4 Replication cycle

The vaccinia virus replication cycle is illustrated in Figure 1-5. Both, the IMVs and the EEVs are able to attach to and enter the susceptible host cell. The full mechanism by which the virus enters the cell is not yet completely understood, but different viral surface proteins which are involved in this process have been identified. These include A27, H3 and D8 which interact with glucosoaminoglycans (GAGs) respectively.[71–74] After attachment to the cell there are two different ways how the IMV can enter. The first way is that the IMV membrane fuses with the plasma membrane in a pH-independent manner followed by release of the core into the cytoplasm.[75] The second way is that the IMV is endocytosed and so the viral and the vesicular membrane fuse.[76] The mechanism how the EEV enters the cell is difficult to analyze due to the low amount of EEV produced by most VACV strains and by the fragility of the EEV membrane.[77] The main challenge by infection with EEV is that two viral membranes have to disrupt to release the viral core into the cytoplasm. An electron microscopic study revealed, that after attachment of the EEV to the host cell the outer viral membrane is disrupted by a ligand-induced non-fusogenic reaction, followed by the fusion of the inner viral membrane with the plasma membrane.[78] After successful host cell entry, the primary uncoating takes place and the viral core is released to the cytoplasm associated with changes in cell function, morphology and metabolism called cytopathic effects (CPEs).[79]

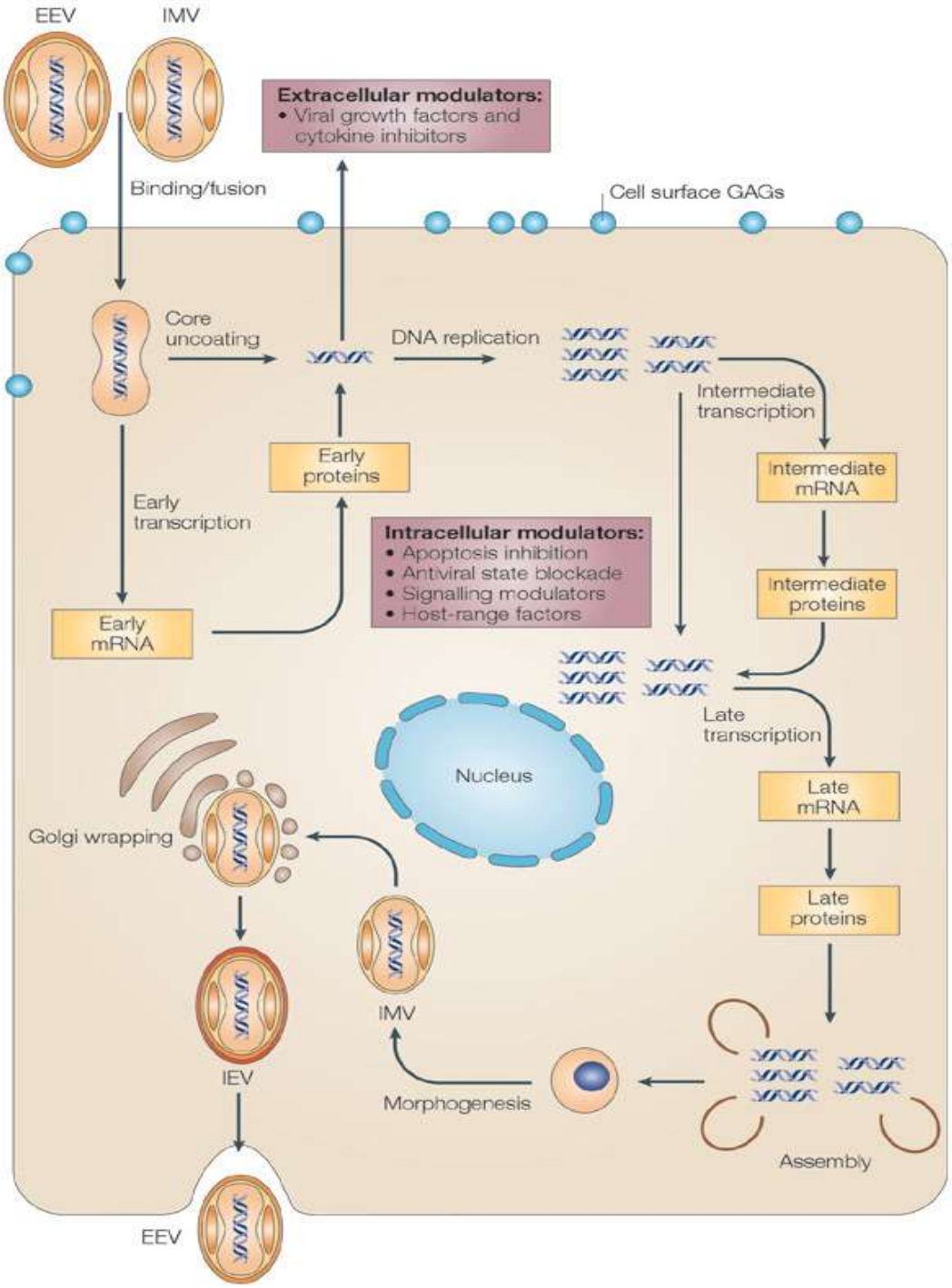

Figure 1-5 Vaccinia virus replication cycle: The viral particle gets inside the cell. By this, the core, containing the genome, is released into the cytoplasm. By transcription of early genes the genome gets discharged from the core, thus DNA replication can start. After transcription of intermediate and late genes the assembly of new immature viral particles, containing the replicated viral genome and proteins necessary for early transcription, takes place. Those particles are developing to IMV which are then transported to the trans-golgi network where they obtain two more membranes. The now called IEV are transported via microtubules to the cell surface where the outer membrane fuses with the cell membrane. Afterwards, the virions either stay attached to the surface as CEV or they dissociate as EEVs (taken from McFadden [70]).

Early transcription of viral mRNAs which are similar to host mRNAs already starts in the viral core driven by the DNA-dependent RNA polymerase and viral transcription factors.[70] Approximately half of all viral genes are expressed during the early phase of infection. The early proteins are either important for DNA synthesis or have similar sequences to cellular growth factors and can induce proliferation of neighboring host cells or interact with the host immune defense mechanism to help the virus to escape it. Those early proteins also induce the second uncoating which results in a release of the genome associated with a nucleoprotein complex from the core. This process is supposed to be initiated by a viral trypsin-like protease which forms holes in the core.[68] Thereby the DNA is released into the cytoplasm where it can serve as a template for DNA replication. This happens within so called mini-nuclei (virus factories) which are surrounded by membranes originated from the endoplasmatic reticulum and exist until the beginning of virus morphogenesis.[68,80] The newly synthesized DNA molecules serve as templates either for DNA replication or for transcription of intermediate genes. In this process both are involved, proteins of the early phase as well as cellular proteins. Intermediate genes encode for different proteins including those necessary for late gene transcription. The late genes encode for proteins necessary for the formation of new virions and proteins which will be incorporated into the new virus particles.[67] Once these factors are synthesized the assembly of new viral particles begins. First immature virions are assembled. Those are round particles surrounded by a membrane possibly acquired from the cellular secretory pathway. These particles mature to brick shaped IMVs which are released by cell lysis only. Some of this particles can obtain a second double membrane originated from the trans-golgi or early endosomal compartment to form the IEVs. These viral particles are then transported to the cell surface via microtubules.[81] The IEVs fuse with the plasma membrane to form CEVs. These either remain attached to microvilli or dissociate from the membrane as EEVs. By this, virus spread within the whole organism or from host to host is promoted.[67,81]

1.3.5 The VACV isolate LIVP 1.1.1 and recombinant vaccinia virus construct GLV-1h68

Two VACV strains which are promising tools for oncolytic virotherapy, used in this thesis, are the recombinant VACV GLV-1h68 and its parental strain LIVP 1.1.1.

The VACV isolate LIVP 1.1.1 was derived from LIVP (Lister strain, Institute of Viral Preparations, Moscow, Russia).[82] Sequencing revealed the presence of different mutations in several genes including that for the thymidine kinase.[83] LIVP 1.1.1 was found to be able to infect both, human and canine cancer cells in cell culture and in tumor-bearing nude mice, respectively.[82,83]

The recombinant vaccinia virus GLV-1h68 (Figure 1-6) has been derived from the LIVP wild-type strain. It was designed by Genelux Corporation, San Diego, USA, to locate, colonize and destroy cancer cells specifically, and not harming healthy tissues and organs.[84]

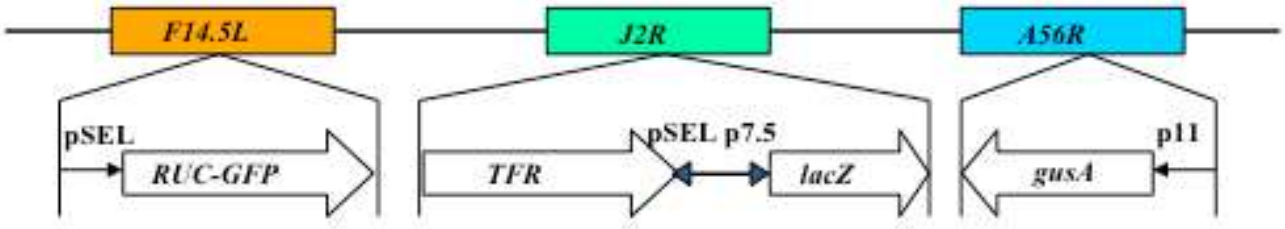

Figure 1-6: The recombinant VACV GLV-1h68: The wild type LIVP strain was used to generate the recombinant vaccinia virus GLV-1h68. Three different gene cassettes (encoding for RUC-GFP, lacZ and gusA) were inserted into three different loci (F14.5L, J2R and A56R).

GLV-1h68 was constructed by inserting three expression cassettes. The gene, encoding for Renilla luciferase–*Aequorea* green fluorescent protein (RUC-GFP) fusion under control of a synthetic early/late promoter, was cloned into the F14.5L loci. *ß-galactosidase* (lacZ) was inserted into the thymidine kinase (TK) coding J2R loci under the control of the early/late promoter p7.5 and *ß-glucuronidase* (gusA) into the hemagglutinin (HA) coding A56R loci controlled by the viral promoter p11. Furthermore the expression cassette for a transferrin receptor was inserted into the J2R loci as well but in reverse orientation.[84]

All three deletions caused by the insertions of the three different gene cassettes lead to a decreased toxicity and to an increased specificity of the virus to selectively replicate in and lyse tumor cells.[84] The thymidine kinase catalyzes the synthesis from desoxythymidinphosphate and is therefore important for the synthesis of new DNA molecules. The deletion in the gene encoding for this enzyme results in a high dependence of the virus from cellular thymidine kinases. The fact that TK levels are higher in tumor cells compared to normal tissue cells [85] results in a high tumor specificity of the virus. Furthermore the deletion of the TK leads to a decreased virulence of the virus.[86] Deletion of A56R encoding for hemagglutinin also results in a stronger attenuated virus while the protein itself is not necessary for viral replication.[87,88] F14.5L

encodes for a small conserved transmembrane protein which can be found in IMV as well as in membranes of infected cells.[89,90] The deletion also results in decreased vaccinia virus pathogenicity. All these deletions together result in high tumor specificity of the virus and a decreased virulence making GLV-1h68 a promising tool for successful and safe oncolytic virotherapy.

Additionally, GLV-1h68 offers great theranostic potential by combining diagnostic and therapeutic properties. On the one hand, the insertion of RUC-GFP fusion protein allows the visualization of infected tissues and the monitoring of tumor regression by live imaging. On the other hand, GLV-1h68 infects and lyses both tumor cell in cell culture as well as tumors in a xenograft mouse model. By this the virus is able to infect and destroy a lot of different tumor types. Among them: human solid breast tumors, human hepatocellular carcinomas, human prostate tumors, malignant pleural mesothelioma and squamous cell carcinomas but also canine and feline mammary carcinomas and murine melanoma.[84,91–97]

Hence, the tumor shrinking activity of the virus was not only shown in different human xenograft mouse models but also different clinical trials phase I with GL-ONC 1 (GLV-1h68) are already ongoing.[98]

1.4 Two tumor models as examples of metastatic cancer

1.4.1 Cervical carcinoma

According to the WHO cervical cancer is the 4th most common cancer in women worldwide.[99,100] There were about 528,000 cases of cervical cancer in 2012, and 266,000 cases of death. Therefore, cervical cancer is responsible for about 8% of all female cancer related deaths. Almost 80% of all cases occur in developing countries. Fortunately both, the incidences as well as mortality rate were decreasing in the past. In several western countries, where screening programs have been long established, cervical cancer rates have decreased by as much as 65% over the past four decades [101] but with a still high mortality rate of about 52% a lot of effort has to be put on the development of screening and better treatment programs.

Cervical cancer types are characterized by the cells they are originated. The most common type of cervical cancer is the squamous cell carcinoma.[102] It accounts for about 85-90% of all cases of cervical cancer. Those cells are the main part of the epidermis of the skin, making this cancer a

type of skin cancer. The second most common form is the adenocarcinoma which arises from cells that make up glands in the cervix. It forms about 10-15% of all cases. Additionally there are some rare forms like the adenosquamous carcinoma which has characteristics of both, squamous cell and adenocarcinoma, or neuroendocrine tumors, which arise from cells of the endocrine and nervous systems.

At the early stages of disease most women are free of symptoms.[103] Sometimes vaginal bleeding, vaginal discharge and contact bleeding as well as pain during sexual intercourse can occur. In advanced disease, metastases may be present in the aortic and mediastinal nodes, the lungs and skeleton.[104]

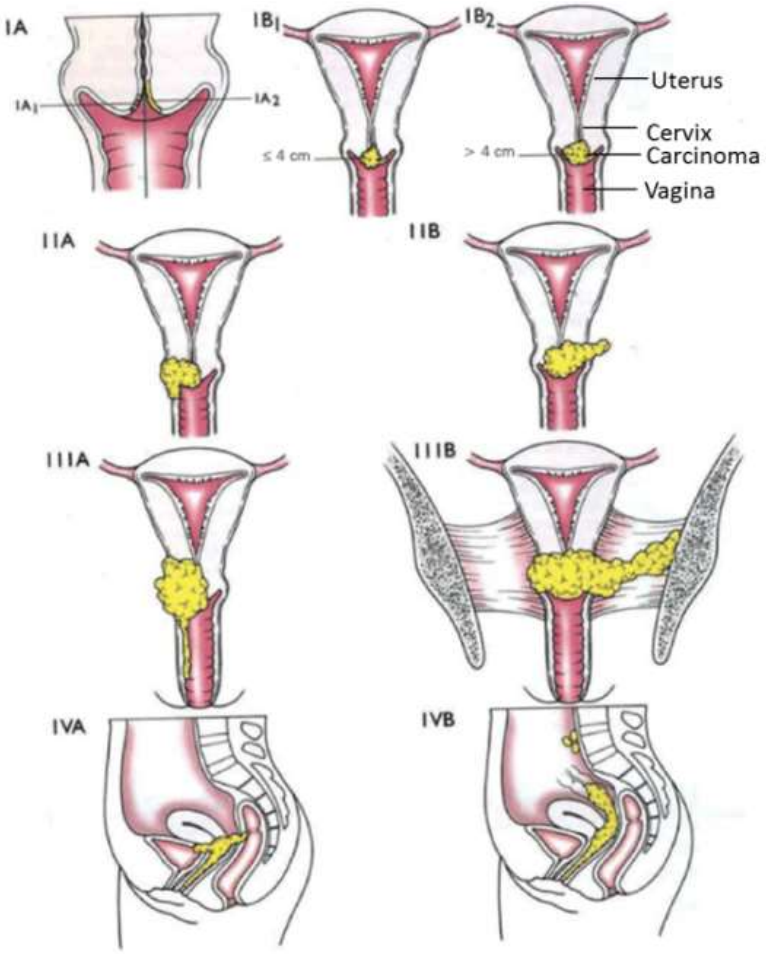

Figure 1-7 Staging of cervical carcinoma according to the International Federation of Gynecology and Obstetrics: Cervical cancer can be divided into four stages (I-IV) according to the invasiveness and presence or absence of metastases (modified from Camisão *et al*. [105]).

Cervical cancer is staged by the International Federation of Gynecology and Obstetrics (FIGO) staging system, which is based on clinical evaluation.[104] Only the following diagnostic tools are

allowed to determine the stage: palpation (feeling with the fingers), inspection, colposcopy, endocervical curettage, hysteroscopy, cystoscopy, proctoscopy, intravenous urography, and X-ray examination of the lungs and skeleton. There are five different stages (0-IV) (as seen in Figure 1-7) and survival is connected to the stage of cancer.[102,104]

- Stage 0 (Carcinoma *in situ*; preinvasive carcinoma): The carcinoma is limited to the surface layer of the cervix.
- Stage I: The carcinoma is confined to the uteri. This stage can be, like all other stages subdivided into two parts:
  - ✓ Stage IA: The diagnosis is based on microscopic examination of removed tissue, preferably a cone biopsy, which must include the entire lesion. The depth of invasion must not be larger than 5 mm taken from the base of the epithelium from which it originates and the horizontal spread must not be wider than 7 mm. The 5-year survival rate is between 90-95%.
  - ✓ Stage IB: This stage includes clinically visible lesions limited to the cervix uteri or pre-clinical cancers greater than stage IA. The 5-year survival rate has decreased to 80-85% in this case.
- Stage II: In this case the cervical carcinoma has invaded beyond the uterus, but has not extended to the pelvic wall or to the lower third of the vagina.
  - ✓ Stage IIA: This is without parametrial invasion. Survival rate is between 50 and 65%.
  - ✓ Stage IIB: This is with parametrial invasion. The survival rate is between 40 and 50%:
- Stage III: At this stage the 5-year survival rate has decreased to 25-30%.
  - ✓ Stage IIIA: The tumor is not yet extended onto the pelvic sidewall but has grown into the lower third of the vagina.
  - ✓ Stage IIIB: The tumor is extended to the pelvic wall and/or can cause hydronephrosis or non-functioning kidney.
- Stage IV: At this stage metastasis takes place. Therefore the 5-year survival rate has dropped beyond 5%.
  - ✓ Stage IVA: The tumor has extended beyond the true pelvis or has clinically invaded the mucosa of the bladder and/or rectum.

- ✓ Stage IVB: Tumor cells have spread to distant organs.

The most important risk factor which increases the chance to develop cervical cancer is first of all infection with the human papilloma virus (HPV). But also smoking and the intake of oral contraceptives (OCs) are discussed as risk factors.[106–109] Already in the middle of the 1970th Harald zur Hausen postulated a correlation between the genital wart causing HPV and the development of cervical cancer. In the 1980th he and his colleagues identified the subtypes HPV16 and HPV18 in the majority of cervical cancer biopsies.[110–112] In the following decades the association between HPV infection and cervical cancer was proven progressively and although, HPV 16 and 18 are responsible for about 70% of all cervical cancer cases, more HPV subtypes have been identified as cancerogenic. All in all fifteen HPV types were classified as high-risk types (HPV 16, 18, 31, 33, 35, 39, 45, 51, 52, 56, 58, 59, 68, 73, and 82); 3 were classified as probable high-risk types (HPV 26, 53, and 66); and 12 were classified as low-risk types (HPV 6, 11, 40, 42, 43, 44, 54, 61, 70, 72, 81, and CP6108).[113] Generally HPV DNA is detectable in more than 95% of all cervical cancer biopsies and HPV negative cervical cancers form just a small amount.

The most promising tool to prevent cervical cancer is currently vaccination against HPV. The first vaccination agent *Gardasil* was introduced in 2006 and protects against HPV types 16 and 18, but also against two HPV types (6 and 11) which cause almost all cases of genital warts.[114,115] *Cervarix* is used in the EU since 2007 and was approved by the FDA in 2009. This vaccine protects also against HPV 16 and 18.[116]

The treatment of cervical cancer depends on the stage and whether the woman wants to have children. If fertility should be preserved and the tumor is at stage IA1 without lymphovascular space involvement at the pathological examination, negative margins, and normal endocervical curettage a conization, which is an excision of a cone-shaped sample of tissue from the mucous membrane of the cervix, is the treatment of choice.[117] Another fertility preserving method at stages IA2 and IB1 is a trachelectomy, a surgical removal of the uterine cervix. During surgery spread of tumor cells to lymph nodes has to be always evaluated thus a laparoscopic lymph node dissection is performed before trachelectomy. If the lymph nodes are negative the trachelectomy can be performed. If the lymph node biopsy is positive or the tumor is at a higher stage or the woman does not want to have children, a hysterectomy is done. This is the removal

of the uterus as well as removal of the cervix, ovaries, fallopian tubes and other surrounding structures, associated with lymphadenectomy. For locally advanced (stage IIB–IVA) or high-risk early-stage cervical carcinoma chemotherapy with cisplatin and radiotherapy should be considered as standard treatment.[118] All in all, treatment of early stage and non-metastasized tumors is easy and the survival rates are high. The main problem is treating metastases and once they occur, survival rates decrease drastically. Therefore the development of new treatment tools for metastases is necessary.

1.4.2 Melanoma

Melanoma is a type of skin cancer, which develops from melanocytes and can occur at any part of the body containing those cells.[119] Generally, one can distinguish between cutaneous melanoma which arises from epidermal melanocytes of the skin, representing the most common site of origination and non-cutaneous melanoma from melanocytes lining the choroidal layer of the eye, respiratory, gastrointestinal or genitourinary mucosal surfaces.

According to the WHO there are between 2-3 million new cases of non-melanoma skin cancer globally every year but only 132,000 new cases of melanoma making it the less common type of skin cancer. However, malignant melanomas are responsible for about 75% of all skin cancer related death, making it also one of the most aggressive and rapidly increasing types of cancer.[120,121] About 80% of all cases of malignant melanoma arise in North America, Europe, Australia and New Zealand and the disease predominantly occurs in white-skinned populations, so called Caucasians.[102] The incidence between men and women is very similar with slightly higher rates in men.[122] However, the incidence is higher in young women compared to men, whereas at later ages more men develop melanoma compared to woman with a median age of 58 years in women and 65 years in men in Germany.[123]

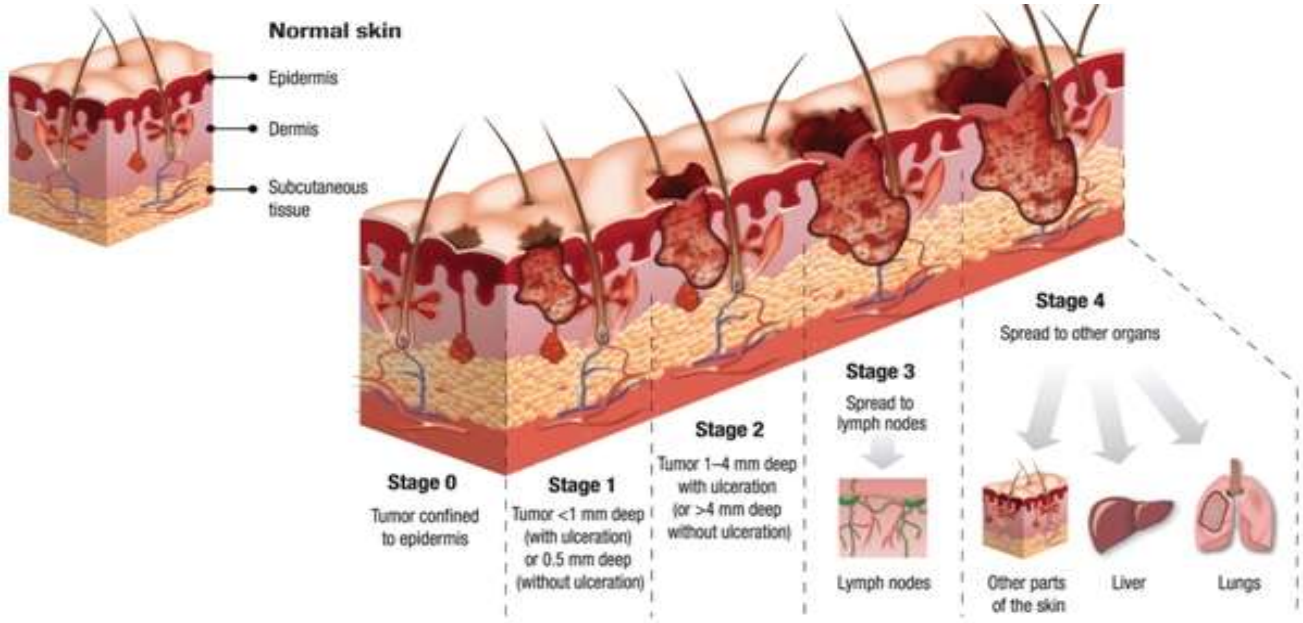

Figure 1-8: The 5 different stages of melanoma: Melanoma can be divided into five stages according to the invasiveness, ulceration and presence or absence of metastases (taken from[124]).

Like already mentioned for cervical cancer, survival of melanoma is strongly connected to the stage at which the tumor is diagnosed as well. One can distinguish between 5 different stages (0- 4) which are classified with aid of the TNM system (T= tumor thickness, N= number of regional lymph nodes, M= distant metastases).[125] The different classifications according to the TNM-system can be seen in Figure 1-8.

- Stage 0 (melanoma *in situ*): The melanoma cells are located only in the top surface layer of the epidermis and have not started to spread into deeper layers (Tis). The survival is almost 100%
- Stage 1 (invasive melanoma): The tumor thickness is less than 1 mm (T1). The covering layer of skin over the tumor can be either not ulcerated (stage IA) or ulcerated (stage IB). Tumors between 1 to 2 mm without ulceration (T2) also belong to this category. The melanoma is only stuck to the skin and there is no sign that it has spread to lymph nodes or other parts of the body. Melanomas at this stage are well curable and the 5-year and 10-year survival rates range from 93-97%.
- Stage 2 (high risk melanoma): There are also no lymph node or distant metastases at this stage. This stage can be separated in three parts:
  - ✓ Stage IIA: Tumor is 1-2 mm (T2) and ulcerated or 2-4mm (T3) and not ulcerated.
  - ✓ Stage IIB: Tumor is 2-4 mm and ulcerated or larger than 4mm and not ulcerated.

- ✓ Stage IIC: Tumor is larger than 4 mm (T4) and ulcerated.

  At this stage the tumor is also well curable and the survival rate ranges from 45-79% dependent on the subclass

- Stage 3: This stage can also be divided into three parts dependent on the amount of positive regional lymph nodes (up to 3, N1-3) and whether there are small areas of melanoma cells in the skin or lymph channels close to the main melanoma. The survival rate is between 24 and 70%, again dependent on the subclass.
- Stage 4: The melanoma cells have spread elsewhere in the body, away from the primary site and regional lymph nodes. The most common organs for melanomas to spread are the lungs, liver or brain or distant areas of the skin. At this stage the survival rate is with 7-19% very low.

The strongest melanoma risk factors are UVR, genetic background and a fair skin/red hair phenotype. Epidemiological studies revealed that intensive UVR exposure and heavy sunburns, especially at childhood are strongly connected to a high risk developing melanoma.[126] Furthermore, UV radiation from tanning in sunbeds seems to increase the risk of melanoma.[127] The whole mechanism how UVR causes melanoma is not yet fully understood but it contributes to DNA damages, induction of reactive oxygen species (ROS), alterations in cutaneous immune function and production of growth factors which may than lead to melanoma.[128] Further, different genes, like *CCM1*, *CCM2* and *CCM3,* have been identified, which are responsible for an increased risk of melanoma.[129] Another risk factor are special melanocortin 1 receptor gene variants which is not only associated with melanoma but also with a red hair/fair skin phenotype which have the highest chance to develop melanoma.[130,131]

Like already mentioned the survival is extremely dependent on the stage of tumor. Therefore it is very important to detect the melanoma as early as possible especially before metastases have developed. In Germany, for example, a melanoma screening at a dermatologist can be performed every two years starting at the age of 35. The most important aspect of diagnosis is visually by the ABCDE mnemonic (Figure 1-9).[132] The abbreviations stand for: **A**symmetrical skin lesions, irregular **B**order, multiple **C**olors, **D**iameter greater than 6 mm and **E**volving over time. If there is a suspicious pigmented lesion a biopsy should be performed. Therefore, the whole lesion, including some healthy surrounding tissue, is excised. It is important to document the

dimension of the tumor because together with histological analysis, staging and prognosis can be determined. Depending on the stage a sentinel lymph node biopsy is performed as well.

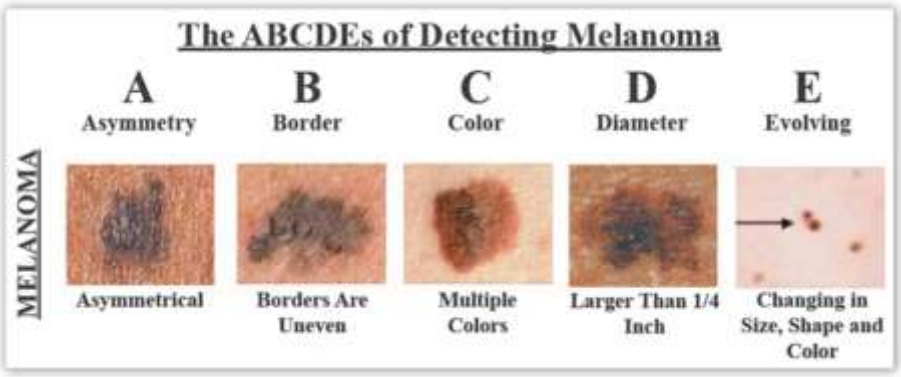

Figure 1-9 The ABCDE mnemonic to diagnose melanoma: : Asymmetrical skin lesions, irregular **B**order, multiple **C**olors, **D**iameter greater than 6 mm, **E**volving over time (modified from [133]).

Thus, surgery is a good option to remove primary tumors, but it is difficult to successfully treat metastases because melanoma cells have a high resistance to cytotoxic agents.[134] This is supposed to be due to the fact that melanocytes arise from highly motile cells, which have enhanced survival properties and which are not affected by drug-induced apoptosis. So far, there are only few FDA approved therapies for metastatic melanoma like *Dacarbazine*, high dose interleukin-2 (HD IL-2) or *Ipilimumab*, which are also used as a combination therapy.[135,136] However all of the three therapy options have very low response rates (10-15% and 6-10%, respectively), prolong the overall survival just for a few month and especially HD IL-2 has a severe toxicity. More promising seem to be BRAF inhibitors which are already tested in clinical trials, because 40-60% of all melanoma contain a mutation in the BRAF gene.[135] Nevertheless, there is no completely successful therapy for metastatic melanoma. Therefore much effort has to be put on developing new agents to threat those tumors. One promising tool seems to be oncolytic viruses, like the vaccinia virus.[96]

1.5 Aims of this work

In the past, the therapeutic effect of GLV-1h68 on different tumor models was described.[84,91-95,97] Unfortunately, so far, there is only one metastatic model among them, the prostate cancer cell line PC-3.[92,137] Hence the aim of this thesis was to establish new metastatic models to analyze the influence of GLV-1h68 on metastases.

The first model which was analyzed in this thesis was the human cervical cancer cell line C33A. Previous experiments indicated that this cell line might have metastatic abilities. To facilitate monitoring and closer investigation of the metastatic behavior, the gene encoding for the red fluorescence protein had to be stably inserted into the cell genome by lentiviral transduction. The resulting C33A-RFP cells had to be subsequently tested in cell culture experiments to check whether the insertion has altered the susceptibility of the cells to infection, replication and cell lysis by GLV-1h68. Afterwards a time course study had to be performed to determine the metastatic potential and pattern of metastatic spread to lymph nodes and other organs after tumor cell implantation in immune compromised nude mice in detail. Therefore, fluorescence imaging, histologic and microscopic techniques had to be applied. Further on, it was essential to analyze whether the cells spread via the lymphatic or the haematogenous route or even use both ways and whether RFP signal can be detected in other organs.

The next aim was to investigate whether GLV-1h68 is a suitable tool for treatment of both, the primary tumor and metastases of the C33A xenograft model. Therefore, the virus had to be administered systemically in tumor bearing mice at a time point, when metastases were fully established. The main focus was on the regression of lymph node metastases. Furthermore, it will be investigated whether there were differences in colonization efficiency of GLV-1h68 between tumors and lymph node metastases. If this is the case, the reasons for this had to be analyzed by histological and FACS analysis.

The C33A-model can be a valuable model to study metastatic spread and virus therapy on metastases, but the disadvantage of this model was that the influence of the immune system on virus and virus therapy cannot be included. Therefore, it was necessary to find a cell line, which can be studied in an immune-competent mouse background. The ambition was to find a model which displays the conditions in a human cancer patient, so that the results can more directly be transferred into the clinics. A valuable cell line might be the murine melanoma cell line B16F10, which was already described to be metastatic.[96] First of all, it had to be determined whether GLV-1h68 was suitable for therapy of this cell line, or whether the parental strain LIVP 1.1.1 was more efficient in infection, replication and cell lysing in cell culture. The more efficient virus had to be used in following studies. Afterwards, comparative studies were performed, to find the optimal implantation site -subcutaneous or into the footpad- to generate the highest metastatic

burden and to check whether this was a suitable model in immune-competent mice. Additionally, the optimal virus injection route had to be identify to confirm that as much virus as possible reaches tumors and metastases as fast as possible without clearing or inhibition by the immune system.

2 Material

2.1 Chemicals and Enzymes

Chemicals	Company
Activation Reagent PMS (for XTT)	Biotium, Hayward, USA
Acetic acid ($C_2H_4O_2$)	Merck, Darmstadt, Germany
Acetone	Carl Roth, Karlsruhe, Germany
Agarose Low Melt	AppliChem, Darmstadt,Germany
2,3-bis-(2-methoxy-4-nitro-5-sulfophenyl)-2H-tetrazolium-5-carboxanilide, disodium salt (XTT)	Biotium, Hayward, USA
Bromphenol blue	Sigma, Steinheim, Germany
1x BSS	Sigma, Steinheim, Germany
Carboxymethylcellulose (CMC)	Sigma, Steinheim, Germany
Crystal violet	Sigma, Steinheim, Germany
DMEM High Glucose (4,5g/l)	Sigma, Steinheim, Germany
Diaminoethanetetraacetic acid (EDTA)	Serva, Heidelberg, Germany
Dimethyl sulfoxide (DMSO)	Sigma, Steinheim, Germany
Disodium phosphate hydrate (Na_2HPO_4*$12H_2O$)	Merck, Darmstadt, Germany
Ethanol (96%)	Chemical dispensing, University Würzburg, Germany
Ethanol (p.a.)	Riedel deHaen, Seelze, Germany
Fetal Calf Serum (FCS)	Sigma, Steinheim, Germany
Formaldehyde (37%)	Sigma, Steinheim, Germany
Gentamycin	PAA, Pasching, Austria
Glycerol	Merck, Darmstadt, Germany
Glycine	Roth, Karlsruhe, Germany
Hoechst dye (33258)	Sigma, Steinheim, Germany
Isoflurane	Abbott, Ludwigshafen, Germany
Isopropanol	Roth, Karlsruhe, Germany

Isopropanol (RNase-free)	AppliChem, Darmstadt, Germany
MB Taq DNA Polymerase	Miverva Biolabs GmbH, Berlin, Germany
β-Mercaptoethanol	Roth, Karlsruhe, Germany
Methanol	Roth, Karlsruhe, Germany
Mowiol	Roth, Karlsruhe, Germany
Paraformaldehyde (PFA)	PAA, Pasching, Austria
1x PBS	Sigma, Steinheim, Germany
Penicillin/Streptomycin	Sigma, Steinheim, Germany
Phusion™ DNA-Polymerase	New England BioLabs, Ipswich, USA
Propidium iodide	Sigma, Steinheim, Germany
RNase-ExitusPlus	AppliChem, Darmstadt, Germany
RNA-Later	Qiagen, Hilden, Germany
RPMI-Medium 1640	Sigma, Steinheim, Germany
Sodium hydroxide (NaOH)	Merck, Darmstadt, Germany
Sodium carbonate (Na_2CO_3)	Merck, Darmstadt, Germany
Sodium chloride (NaCl)	Roth, Karlsruhe, Germany
Tissue – Tek®OCT™ *Compound*	Sakura Finetek GermanyGmbH, Staufen, Germany
Tris-Base, pH 10-11,5	AppliChem, Darmstadt, Germany
Tris-HCl, pH 3,5-5	Roth, Karlsruhe, Germany
Triton X-100	Sigma, Steinheim, Germany
Trypan blue	Sigma, Steinheim, Germany
Trypsin-EDTA	Sigma, Steinheim, Germany
Trizol-Reagent	Invitrogen, Darmstadt, Germany
Tween 20	Roth, Karlsruhe, Germany
Water (RNase-free)	AppliChem, Darmstadt, Germany

2.2 Buffers and Solutions

Agarose histology buffer		0.1%	Triton X-100
		1x	PBS (pH 7.2)
Blocking buffer for agarose histology		0.3%	Triton X-100
		5%	FCS
		1x	PBS (pH 7.2)
CMC medium		7.5 g	CMC
		500 ml	DMEM
		1%	Penicillin/Streptomycin
		10%	FCS
Crystal violet staining solution		1.3 g	Crystal violet
		50 ml	Ethanol
		300 ml	Formaldehyde (37%)
	ad	1 l	dH_2O
DEPC-H_2O		1 l	H2O
		1 ml	DEPC-Reagent
5x DNA running buffer		2 ml	500 mM EDTA
		5 ml	Glycerin
		1 ml	Bromphenol blue (1%)
	ad	10 ml	H2O
Mounting medium for agarose histology		60% (w/v)	Glycerol
		1x	PBS
4% PFA		4 g	PFA in warm dH_2O
	ad		NaOH until solution clears
		10 ml	10x PBS pH 7.4
	ad	100 ml	dH_2O
10x PBS		81.8 g	NaCl
		2 g	KCl
		29 g	$Na_2HPO_4*12H_2O$
		2 g	KH_2PO_4
PBS^{++}		500 ml	1x PBS
		0.35 mM	$CaCl_2$
		0.25mM	$MgCl_2$
PBST		1 l	1xPBS
		0.1%	Tween 20

10x TBT (pH 7.4)		97.6 g	NaCl
		7.25 g	Tris-base
		30 g	Tris-Cl
		50 ml	Tween-20
	ad	1 l	dH_2O
10x TBE buffer		108 g	Tris-base
		55 g	Boric Acid
		40 ml	0.5 M EDTA (pH 8.0)
	ad	1 l	dH_2O

2.3 Used cell lines and cell culture media

2.3.1 Cell lines

B16F10	murine melanoma cell line
C33A	human cervical carcinoma cell line
C33A-RFP	human cervical carcinoma cell line labelled with the red fluorescence protein
CV-1	African green monkey kidney fibroblast cells (*Cercopithecus aethiops*)

2.3.2 Cell culture media

B16F10	500 ml DMEM High Glucose (4,5g/l) 25 ml FCS 5 ml Penicillin/Streptomycin
C33A	500 ml DMEM High Glucose (4,5g/l) 50 ml FCS 5 ml Gentamycin
C33A-RFP	500 ml DMEM High Glucose (4,5g/l) 50 ml FCS 5 ml Gentamycin 5 µg/ml Blasticidin (freshly added to the media, media change ever 2-3 days)
CV-1	500 ml DMEM High Glucose (4,5g/l) 50 ml FCS 5 ml Penicillin/Streptomycin

All infection media were supplemented with 10 ml FCS instead. For freezing cells 10% DMSO was added to 90% culture media.

2.4 Synthetic oligonucleotides

Humane β-Actin:	Forward-Primer: 5'-CCT CTC CCA AGT CCA CAC AG-3' Reverse-Primer: 5'-CTG CCT CCA CCC ACT C-3'
Murine β-Actin:	Forward-Primer: 5'-CGT CCA TGC CCT GAG TC-3' Reverse-Primer: 5'-GCT GCC TCA ACA CCTCAA C-3'

All primers were synthesized by Metabion, Martinsried, Germany.

2.5 Kits

DNA-freeTM Kit	Ambion, Austin, TX, USA
RevertAid TM First Strand cDNA Synthesis Kit	Fermentas, St. Leon-Rot, Germany
RNeasy Mini Kit	Qiagen, Hilden, Germany

2.6 Antibodies

2.6.1 Antibodies for histology

Primary Antibody	Origin	Company
Anti-Lyve1 (IgG; polyclonal)	rabbit	Abcam Cambridge, UK, (ab14917)
Anti-CD31/mouse (IgG; monoclonal)	hamster	Millipore, Billerica, US (MAB1398Z)
Secondary Antibody	**Origin**	**Company**
anti-hamster Cy5 (Dylight 649)	donkey	Jackson Immuno Research, Suffolk,UK
anti-hamster Cy2	donkey	Jackson Immuno Research, Suffolk, UK
anti-rabbit Cy5 (Dylight 649)	donkey	Jackson Immuno Research, Suffolk, UK
anti-rabbit Cy2	donkey	Jackson Immuno Research, Suffolk, UK
anti-rat Cy5 (Dylight 649)	donkey	Jackson Immuno Research, Suffolk, UK
anti-rat Cy2	donkey	Jackson Immuno Research, Suffolk, UK

2.6.2 Antibodies for FACS analysis

Specificity	Conjugate	Clone	Isotype	Company
α-CD11b	APC	M1/70	Rat IgG2b	eBioscience, Frankfurt, Germany
α-CD19	PerCP-Cy5.5	6D5	Rat IgG2a	eBioscience, Frankfurt, Germany
α-CD45	PerCP-Cy5.5	30-F11	Rat IgG2b	eBioscience, Frankfurt, Germany
α-CD49b	APC	DX5	Rat IgM	eBioscience, Frankfurt, Germany

Isotype Controls	Conjugate	Clone	Company
Rat IgG2a κ	PerCP-Cy5.5	eBR2a	eBioscience, Frankfurt, Germany
Rat IgG2b κ	APC	eB149/10H5	eBioscience, Frankfurt, Germany
Rat IgG2b κ	PerCP-Cy5.5	eB149/10H5	eBioscience, Frankfurt, Germany
Rat IgM κ	APC		eBioscience, Frankfurt, Germany

2.7 Recombinant viral construct GLV-1h68 and the LIVP 1.1.1 clone

For this study the oncolytic vaccinia viruses GLV-1h68 and LIVP 1.1.1 were used. Both viruses were described in detail at chapter 1.3.5.

2.8 Laboratory animals

For all *in vivo* experiments with C33A and C33A-RFP female athymic nude FoxN1^{nu} and additionally for B16F10 experiments immunocompetent C57BL/6JOlaHsd mice were used. The animals were purchased from Harlan (Rossdorf, Germany).

The FoxN1 mouse model is characterized by an autosomal recessive mutation in the nu locus on chromosome 11. This leads to a completely hairless phenotype in the mice. The nude mutation has also a profound effect on thymic development, but does not affect the lymphoid compartment. Adult mice retain a nonfunctional cystic thymic rudiment, leading to an absence of mature T lymphocytes**.** B cell function is normal in athymic nude FoxN1 mice. Due to the defects in the immune system of the mouse, athymic nude FoxN1 mice are suited as adequate laboratory animals in oncology, immunology and additional fields of biomedical research.

Another advantage of the used mouse model is that xenotransplants will not be rejected by the mouse.

C57BL/6 is the most widely-used inbred strain and has a fully developed immune system. It serves as a background for many induced and genetically-modified models. It is commonly used for a number of different research purposes, including toxicology, immunology, aging and cancer research.

Figure 2-1 Used mouse strains: Left: Phenotypic appearance of FoxN1^{nu} mice; right: Phenotypic appearance of C57BL/6JOlaHsd

The animals were kept in small groups of 3 to 6 animals with a 12 hour day-night rhythm by dimmed light in sterile cages. All animal experiments were carried out in accordance with protocols approved by the "Regierung von Unterfranken" in Würzburg, Germany.

2.9 Consumption items

Consumption items	Company
Aseptic filter (0.2 µl & 0.45 µl)	Schleicher&Schuell, Dassel, Germany
Alcoprep	Triad Group, Inc., Hartland, WI, USA
Cannulae	Braun, Emmenbrücke, Switzerland
Cell culturing flasks (25 cm², 75 cm² and 175 cm²)	Greiner, Frickenhausen, Germany
Cryo tubes	Greiner, Frickenhausen, Germany
Gloves (Semperguard Latex)	Semperit, Wien, Austria
Microscope cover glasses	Marienfeld, Lauda-Königshofen, Germany
Microscope cover glasses (round)	Hartenstein, Würzburg, Germany
Microscope slide	Roth, Karlsruhe, Germany
Microscope slides, Polysine™	Menzel GmbH, Braunschweig, Germany

Parafilm	Hartenstein, Würzburg, Germany
Pipet tips	Sarstedt, Nümbrecht, Germany
Razor blade	Wilkinson Sword GmbH, Solingen, Germany
Sample tubes (0.5 ml, 1.5 ml, 2 ml)	Sarstedt, Nümbrecht, Germany
Sample tubes (15 ml & 50 ml)	Greiner, Frickenhausen, Germany
Serological piper (5 ml, 10 ml, 25 ml, 50 ml)	Greiner, Frickenhausen, Germany
Syringe	Becton, Heidelberg, Germany
Well plates (6-well, 24-well, 96-well)	Greiner, Frickenhausen, Germany

2.10 Equipment

Equipment	Company
Anesthetic device	Berthold Technologies, Bad Wildbad, Germany
Autoclave	Webeco, Selmsdorf, Germany
Axiovert 25 inverse microscope	Zeiss, Oberkochen, Germany
Axiovert 40 CFL inverse microscope	Zeiss, Oberkochen, Germany
Axiovert 200M inverse microscope	Zeiss, Oberkochen, Germany
Biofuge fresco	Heraeus, Hanau, Germany
Cell culture incubator	RSBiotech, Irvine, UK
Cryotom 2800 Frigocut	Reichert & Jung, Heidelberg, Germany
DNA gelelectrophorese chamber	BioRad, Munich, Germany
ELISA photometer SunriseTM	TECAN Group, Männedorf, Germany
Flow hood Lamin	AirKendro, Langenselbold, Germany
Glassware	Schott, Mainz , Germany
Infrared lamp	Petra, Burgau, Germany
Neubauer counting chamber	Marienfeld, Lauda-Königshofen, Germany
Maestro *In Vivo* Imaging System	CRi, Woburn, USA
MZ 16 FA stereo fluorescence microscope	Leica, Wetzlar, Germany
PCR cycler	Schleicher & Schuell, Dassel, Germany

Pipetboy comfort INTEGRA	Bioscience GmbH, Fenwald, Germany
Sonifier Branson 450	Heinemann, Schwäbisch Gmünd, Germany
Special accuracy weighing machine	Kern, Balingen-Frommern, Germany
Sunrise asbsorbance reader	TECAN, Crailsheim, Germany
Table centrifuge minispin	Eppendorf, Hamburg, Germany
Table shaker	Heidolph, Schwabach, Germany
Thermomixer Comfort	Eppendorf, Hamburg, Germany
Vibratom VT1000S	Leica, Wetzlar, Germany

2.11 Software

Adobe Photoshop CS4	Image Processing
Adobe Illustrator CS4	Image Processing
Axiovision 4.5	Image acquiring (inverted microscope, Zeiss)
CFlow Plus	FACS analysis
Image J Software Quantification	Image Processing and Signal
Leica Confocal 2.1	Image acquiring (Confocal microscope, Leica)
Leica IM1000 4.0	Image acquiring (Stereomicroscope, Leica)
Maestro 2.10.Software Cri	*In vivo* and *ex vivo* imaging
Metamorph Imaging	Image acquiring (inverted microscope, Leica)
Microsoft Word 2007	Word processing
Microsoft Excel 2007	Diagrams and Statistics
Microsoft PowerPoint 2007	Image Processing

3 Methods

3.1 Cell biological methods

3.1.1 Culturing of adherent growing cells

All cell culture experiments have been performed under a laminar flow hood to ensure sterile conditions. Before use all materials were autoclaved and disinfected with 70% ethanol. To avoid bacterial and yeast contamination, antibiotics, such as penicillin, streptomycin and gentamycin were added to the culturing media. FCS was heat inactivated (30 min, 56 °C) prior using.

All cell lines used in this work were cultured in cell culturing flasks possessed with a special coated surface to improve cell adhesion and proliferation. The cells were cultured under constant conditions of 37 °C in a 100% humidified, 5% CO_2 incubator to maintain optimal growth conditions. To ensure a gentle treatment of the cells, the used media, washing solutions and trypsin were pre-warmed to 37 °C.

To avoid the formation of bi- or multilayers, which slow down or arrest growth, cells were passaged before reaching 100% confluence. Therefore the media was removed and the cells were washed gently with 10 ml BSS to get rid of dead cells and cell debris. The BSS was replaced by EDTA-Trypsin and cells were incubated for a few minutes at 37 °C in the incubator. Trypsin is an endopeptidase which cleaves peptide chains specifically at lysin, arginine and modified cysteine residues. This cleavage causes a proteolytic detachment of the cells from the surface of the culturing flask. Subsequently the proteolysis was inhibited by adding 10 ml culturing media, containing the trypsin inhibitors Ca^{2+} and Mg^{2+}. The media was pipetted repeatedly over the surface of the flask to ensure cells were detached from the surface and from each other. A required amount of cell suspension was transferred to a new flask, containing 40 ml fresh media in case of big flasks and 25 ml in case of intermediate flasks.

In case of C33A-RFP cells, it was necessary to add 5 µg/ml blasticidin directly to the media. C33A-RFP cells are a stable transfected cell line, expressing the red fluorescence protein, which was inserted into the genome of C33A cells together with a blasticidin selection marker. To sustain the selection pressure for RFP positive cells, blasticidin has to be added. Blasticidin containing media was renewed every 2-3 days.

3.1.2 Cell Counting via Neubauer hemocytometer

In many experiments a definite number of cells is needed. To determine the amount of cells in a suspension an improved Neubauer counting chamber was used. A coverslip was placed onto the counting chamber and 10 µl of cell suspension were pipetted under the coverslip. The chamber consists of a grid of 4 squares in the corner each of them divided into 16 squares. The cells in 4 of these squares in a row in each corner were counted. The total cell number per milliliter was calculated using the following formula:

$$cell\ count/ml = counted\ cells\ x\ 10^4\ \ x\ dilution\ factor\ of\ suspension$$

3.1.3 Freezing and thawing of cells

For freezing, the cells were cultured in flasks until they reached 80-90% confluence. After washing the cells with 10 ml BSS, cells were harvested using 5 ml trypsin-EDTA. Afterwards the total cell count was determined and the cell suspension was centrifuged at 1,300 rpm for 5 min. The supernatant was discarded and cells were resuspended in freezing medium to obtain aliquots of $5x10^6$ cells/ml. The cell suspension was transferred to cryo tubes, stored over night at -80 °C and then transferred to liquid nitrogen (-178 °C).

Before thawing the cells, medium in a 75 cm^2 flask was prewarmed and cells were kept at room temperature until the aliquot was defrosted. The cell suspension was transferred to the flask and cells were cultured in an incubator. 24 hours later the cell density was checked and the medium was either renewed or cells were splitted.

3.2 Virological methods

3.2.1 Infection of different cells lines with Vaccinia Virus

24 hours before infection cells were seeded in appropriate well plates and incubated at 37 °C in a 5% CO_2 atmosphere. They were infected at approx. 95% confluence. First of all, the cells in one well were harvested by trypsinization and counted to determine the cell number. The needed amount of virus was calculated using the following formula:

$$\frac{Cell\ count\ x\ MOI}{viral\ titer} = required\ amount\ of\ viral\ stock\ solution$$

The MOI (multiplicity of infection) specifies how much virus is used for the infection in relationship to the cell count. MOI 1 means an infection rate of 1 virus particle per cell. The virus titer is defined as pfu (plaque forming units)/ml.

Viruses are stored at -80 °C. Prior to infection, viruses were thawed in a 37 °C water bath and vortexed for 10 sec to separate virus aggregates. The calculated amount of virus was transferred into the required amount of infection medium (250 µl/well for a 24 well plate, 50 µl/well for a 96 well plate), containing 2% FCS. Culture medium was removed from the wells, cells were washed with BSS and the infection medium with the desired virus concentration was pipetted into the wells. The plates were incubated for 1 h at 37 °C in a humidified 5% CO_2 incubator with gentle agitation every 20 min. Afterwards, the infection medium was replaced by fresh growth medium containing 10% FCS.

3.2.2 Replication assay

To measure the replication efficiency of vaccinia virus in tumor cell lines, cells were seeded in a 24 well plate and 24 hours later infected with GLV-1h68 or LIVP 1.1.1 at different MOIs. For each time point the cells of three wells were infected.

2, 8, 24, 48 and 72 hours after infection the supernatant was collected, frozen in liquid nitrogen and stored at -80 °C. Cells were trypsinised after washing with BSS, and centrifuged at 8,000 rpm at room temperature for 4 min. The supernatant was removed and the pellets were frozen and stored at -80 °C as well. Prior to analysis by standard viral plaque assay, the pellets were resuspended in 1 ml PBS and three freeze and thaw cycles in liquid nitrogen were accomplished with both, cells and supernatant.

3.2.3 Standard viral plaque assay

To determine the viral titer of a suspension a standard plaque assay was performed. For this, CV-1 cells were plated in 24 well plates and cultured until they reached 100% confluence. Prior titration samples were sonicated thrice for 30 sec and 10-fold serial dilutions up to 10^{-6} were prepared in CV-1 infection medium containing 2% FCS.

For titration the CV-1 medium was removed and replaced by 250 µl of the diluted cell suspension. Cells were incubated for 1 h and agitated gently every 20 min. Afterwards they

were covered with 1 ml carboxymethylcellulose (CMC) solution and incubated for another 48 hours at 37 °C in a 5% CO_2 atmosphere. CMC solution is a viscous medium which limits virus spread and restricts virus growth to foci of cells at the sites of initial infection.

Cells were stained by adding 250 µl crystal violet solution per well. After 24-48 h of incubation at room temperature the plates were carefully washed with water and lysed cells can be identified by colorless plaques. One plaque represents one infectious virus particle. All samples were titrated in duplicates and results of each infection were averaged to obtain better accuracy. Plaques were counted and the final titer in pfu/ml was calculated with the following formula:

$$pfu/ml = \frac{number\ of\ counted\ plaques\ (pfu)}{dilution\ factor\ x\ infection\ volume\ (ml)}$$

3.2.4 Cell viability assay

The XTT assay is a fast colorimetric method for the measurement of cell survival and proliferation. In this thesis the influence of viral infection on the survival rate of human and murine tumor cells was analyzed.

XTT (2,3-bis-(2-methoxy-4-nitro-5-sulfophenyl)-2H-tetrazolium-5-carboxanilide sodium salt) measures cell viability based on the activity of mitochondrial enzymes in living cells. The XTT agent is reduced by the succinate dehydrogenase system of the mitochondrial respiratory chain to a solubly orange colored product which only takes place in living cells. The amount of this product generated from XTT is proportional to the number of living cells and can be easily quantified by measuring absorbance at the wavelength of 450 nm.

To determine the influence of either GLV-1h68 or LIVP 1.1.1 on cell viability, cells were seeded in 96-well plates to 95% confluence. After 24 h cells of three wells per time point were infected with virus using an MOI of 0.1 and 1.0 in case of C33A cells and MOI 1 and 5 in case of B16F10 cells. 24, 48, 72 and 96 h after the infection of cells, 50 µl XTT solution were added to the medium and cells were incubated for 2 h at 37 °C in a 5% CO_2 atmosphere. Thereafter, the intensity of the orange dye was measured at a wavelength of 450 nm using a reference wavelength of 650 nm. Uninfected cells were used as a reference and considered as 100% viable.

3.3 Mouse experiments

All animal experiments were approved by the government of Unterfranken, Germany, and conducted according to the German animal protection guidelines.

3.3.1 Subcutaneous (s.c.) implantation of tumor cells

For implantation cells were grown up to 80-90% confluence and harvested by trypsinization. The cell suspension was centrifuged for 5 min at 800 rpm and room temperature and cells were washed with PBS twice. After the second washing step, cells were counted and the cell pellet was resuspended in an adequate volume of PBS. The final concentration was $5x10^6$ C33A-RFP cells and $2x10^5$ B16F10 cells, respectively, in 100 µl PBS.

The tumors were generated by subcutaneous injection of the cell suspension into the right abdominal flank of 6-7 week-old female athymic FoxN1 nude mice, for both C33A-RFP and B16F10. C33A-RFP tumor growth was measured two times weekly and B16F10 tumor growth was measured daily in two dimensions using a digital caliper. Tumor volume was calculated using the following formula:

$$tumor\ volume\ (mm^3) = length\ (mm) x\ width\ (mm)^2 x\ 0{,}52$$

3.3.2 Footpad (f.p.) implantation of B16F10 melanoma cells

Prior implantation cells were prepared as described above (chapter 3.3.1). The injection volume was 20 µl containing $2x10^5$ B16F10 cells.

Cells were implanted in 5-6 week old female C57BL/6 mice or 6-7 week old female athymic FoxN1 nude mice. Prior treatment mice were anesthetized by a mixture of isoflurane and oxygen. 20 µl of cell suspension were then injected to the hind footpad. To prevent extravasation of the cell suspension out of the footpad and up the leg, gentle pressure was applied on the limb just above the foot during cell injection. Tumor size was measured every day and calculated with the formula described above. Weight was measured every day and general fitness was checked.

3.3.3 Anesthesia of mice with isoflurane

For *in vivo* imaging and tumor cell and virus injection into the footpad, respectively, the mice had to be anesthetized. The anesthesia was performed using isoflurane, an anesthetic with hypnotic and muscle-relaxing effects. Mice were put in a knockout box and a mixture of isoflurane together with oxygen was administered to the mice. The animals were maintained in an anesthesia module aerated with 1.5-3% isoflurane/oxygen.

3.3.4 Vaccinia virus injection in tumor-bearing mice

The oncolytic vaccinia viruses GLV-1h68 and LIVP 1.1.1 were injected into tumor-bearing mice to see on the one hand whether they have any influence on metastasis formation and tumor growth and on the other hand if the viruses are able to replicate in tumors and metastases.

3.3.4.1 Intravenous (i.v.) virus injection

Dependent on the experiment mice were injected 18 days after implantation in case of B16F10 tumor-bearing mice, and 21 or 42 days post implantation in case of C33A-RFP tumor-bearing mice, intravenously with one single dose of $2x10^7$ pfu of VACV LIVP 1.1.1 (B16F10 mice) or $1x10^7$ pfu of GLV -1h68 (C33A mice) in 100 µl PBS, into the tail vein. The control group was injected with a single dose of 100 µl PBS. To avoid side infections, injection sites were disinfected with Alco-Preps before. To relieve the injection, mice were irradiated with an infrared lamp for 10 minutes before injection.

3.3.4.2 Intratumoral (i.t.) virus injection

For intratumoral virus injection in B16F10 footpad tumor-bearing mice, mice were anesthetized prior treatment by a mixture of isoflurane and oxygen. Afterwards, one single dose of $2x10^7$ pfu of LIVP 1.1.1 was injected in 20 µl PBS into the tumor at the footpad. Gentle pressure was applied on the limb just above to foot during injection to prevent extravasation. Prior and after treatment, injection sites were disinfected to prevent side infections.

3.3.5 Injection of IgG

Non-specific rat-IgG was used to analyze the permeability of blood vessels in C33A-RFP tumors and metastases. Therefore, 10 mg/kg rat-IgG were injected intravenously into C33A-RFP tumor-bearing mice. 4 hours post injection mice were sacrificed and tumors and lymph node metastases were excised for further histological analysis.

3.3.6 Fluorescence imaging of tumors and metastases

With the aid of different imaging methods it was possible to detect C33A-RFP tumors and metastases by visualization of RFP, expressed by C33A tumor cells. This was done either with the Leica stereo fluorescence microscope with digital CCD-camera or with the Maestro EX imaging system. With the Maestro EX imaging system, RFP signal of tumors can be monitored on living mice, after anesthesia with isoflurane. Unfortunately, this system is not sensitive enough to perform deep tissue imaging. To detect cavernous metastases, the mice had to be sacrificed prior imaging. The abdomen had to be opened and organs, like liver, stomach and gut, had to be removed. Imaging of both, tumors and metastases, with the stereo fluorescence microscope was done *post mortem.* Images were evaluated using Photoshop and Image J, in case of the stereo fluorescence microscope and in case of the Maestro EX Imaging system with the corresponding Maestro Software v2.4.

3.4 Analysis of viral titers in tumors and metastases

To analyze the viral titer in tumors and metastases of C33A-RFP and B16F10 tumor-bearing mice, respectively, the amount of viral particles was determined by standard plaque assay. Prior to this procedure, mice have to be sacrificed, tumors and metastases have to be excised and surrounding muscle and connective tissues have to be completely removed. To later determine the titer per gram organ, metastases and tumors were weighted. First, the tumorous tissue was roughly minced with a scalpel and afterwards homogenized in PBS. This was done mechanically with the FastPrep FP120 Cell Disruptor at a speed of 6,000 rpm for 30 sec, repeated 2-3 times, in special tubes filled with ceramic beads. For complete homogenization 3-4 cycles à 30 sec were performed. To avoid protein degradation it was important to keep the samples on ice between single homogenization steps. Afterwards, samples were sonicated 3x30 sec to completely disrupt tissue aggregates. Finally, the homogenates were centrifuged at 10,000 rpm for 5 min and the supernatants were transferred into new tubes. The samples were stored at -80 °C till analyzed with a standard plaque assay as described above in chapter 3.2.3.

3.5 Histological analysis of tumors, lymph nodes and organs

3.5.1 Cryosectioning of tumors and lymph nodes

For histological analysis, tumors and a part of the backbone containing the renal and lumbar lymph nodes were excised and fixed in 4% paraformaldehyde/PBS, pH 7.4 overnight at 4°C. This and all following steps were performed in the dark as far as possible to prevent photo bleaching of RFP. The next day, tumors and lymph nodes were washed in PBS under mild agitation. They were transferred to 10% sucrose in PBS and stored overnight at 4 °C. Next, they were incubated for 3 h in 30% sucrose at room temperature for dehydration. Dehydration was terminated when the tumors and backbones were fallen to the bottom. Afterwards they were incubated in a solution consisting of 50% Tissue Tek in PBS for another 2 h and then placed in an embedding mold and covered with Tissue Tek. They were kept at RT for an hour allowing air bubbles to ascent and disappear. Following the molds were placed on dry ice and stored at -80 °C after they were completely frozen.

Sectioning was performed using a cryotome. 10 µl thick coronal sections were transferred on polylysin covered glass slides and stored at -80 °C until analysis.

3.5.2 Immunohistochemical staining of cryosections

Cryosections were dried at RT and then placed in aceton at -20 °C for 10 min for fixation and dried again at RT. Afterwards the slices were incubated with the primary antibody in appropriate dilutions in PBS at RT in a humidity chamber for 1 h. Next, they were washed three times for 5 min in PBS followed by incubation with the secondary antibody and Hoechst (stock solution: 50 mg/ml, 1:400) for 1 h in a humidity chamber. After another three washing steps in PBS as described above, slices were placed in ethanol for 1 min. After drying the sections at RT they were mounted using Mowiol 4-88 and stored in the dark to prevent bleaching.

3.5.3 Agarose sections of lymph nodes and tumors

Another method for histological analysis are agarose sections. Therefore tumors and lymph nodes were excised and fixed in 4% paraformaldehyde/PBS, pH 7.4 overnight at 4 °C as well. For this method, tumors and lymph nodes were washed several times in PBS in the dark to avoid

bleaching as well. Afterwards they were imbedded in 5% low melt agarose and stored at 4 °C until the agarose was hardened. Tissues were cut into 70 µm slices with a vibratom.

3.5.4 Immunohistochemical staining of agarose sections

First, tissue specimens were permeabilized and blocked in a permeabilisation solution consisting of PBS with 0.2% Triton X-100 und 5% FCS for 1 h at RT. Afterwards, slices were incubated with the primary antibody in the permeabilisation solution overnight. The next day slices were washed thrice with the solution for 10 min followed by a 4 h incubation step with the secondary antibody in PBS with 0.2% Triton X-100 und 5% FCS. Additionally, Hoechst (1:400) was added to stain the nuclei. After another three washing steps the tissue sections were mounted onto glass slides with Mowiol 4-88.

3.5.5 Analyses of digital fluorescence images

3.5.5.1 Quantification of section labeling

Quantification of stained area was done on the one hand to determine the amount of necrotic tissue in tumors and lymph node metastases. Therefore 10 µm cryo sections of tissue samples were stained with Hoechst 33342 to label nuclei. The fraction of a section not stained by Hoechst due to nuclei degradation was defined as necrotic area. On the other hand quantification of stained area was performed to determine the permeability of blood vessels by quantifying extravagated IgG. Hence, digital images of 70 µm agarose sections of tumors and lymph node metastases were stained with an α-IgG antibody and analyzed. For both staining, Hoechst and IgG, images were taken at 10 fold magnification. Two whole sections per tumor and lymph node, respectively, were analyzed. Those RGB-images taken were first converted into 8-bit gray scale images with an intensity range from 0–255 using Photoshop CS04. IgG positive area was directly calculated using ImageJ software. To determine the necrotic area, the non-necrotic, and therefore Hoechst positive area was calculated and subtracted from 100%, also with aid of ImageJ.

3.5.5.2 Measurement of fluorescence intensity

For analysis of Ki67 staining, fluorescence intensity of digital images (x40 magnification) was determined. This was done of 10 µm cryo sections of five tumors, LNs and RNs, respectively. For

each staining, 10 different images per sample were acquired with identical settings. RGB-images were converted into 8-bit gray scale with an intensity range from 0–255 using Photoshop CS04. The fluorescence intensity of Ki-67 staining represents the average brightness of all staining related pixels and was measured using ImageJ.

3.5.5.3 Determination of lymph and blood vessel density

Blood and lymph vessel density was measured in digital images (×100 magnification) of anti-CD31 and anti-LYVE-1 stained 10 µm cryo sections. Eight images per section of tumor, lumbar and renal lymph node, respectively were analyzed per staining (5 tumors per group, 2 sections of each tumor and 8 images per section). To ensure comparability of all images, exposure time was the same for every image. The images were covered with 8 equidistant horizontal lines and all blood or lymph vessels crossing these lines were counted to obtain vessel density which was stated in vessels per defined area.

3.6 RNA isolation from tumors, metastases and organs and analysis by RT-PCR

By isolation and analysis of RNA, the presence of human and murine β-actin in tumors, lymph node metastases, kidneys and lungs was checked. This was done with the aid of a RT-PCR (reverse transcriptase polymerase chain reaction). By this method, cDNA (complementary DNA) is synthesized from mRNA, which is isolated from cells or tissues. This happens by using a specific RNA-dependent DNA polymerase (reverse transcriptase), which triggers enzymatically the conversion from a RNA template into a DNA strand. This DNA can then be amplified by PCR and analyzed using agarose gel electrophoresis.

3.6.1 RNA isolation

For RNA isolation, tumors, lymph node metastases and kidneys were excised and homogenized like already described in chapter 3.4, except, the homogenization was not performed in PBS, but in trizol. Lungs were almost treated the same way, but immediately after excision and before homogenization they were incubated in 1 ml RNA-Later over night at 4 °C. Afterwards lungs can either be homogenized or frozen at –80 °C. This step was done to inactive the RNases which exist in lungs in large amounts. For homogenization 1 ml trizol was added per tissue sample. Additionally, to optimize the amount of isolated RNA from lymph node metastases, 10 µl

β-mercaptoethanol (to inactivate RNases) and 10 µl glycogen were added to lymph node samples. After homogenization 200 µl chloroform was added and samples were inverted repeatedly and incubated for 3 min at room temperature. Afterwards, samples were centrifuged at 9,000 rpm and 4 °C for 15 min. The upper, liquid phase was transferred to a new tube and 500 µl isopropanol was added for RNA precipitation. Again, samples were incubated at RT, for 10 min, followed by centrifugation at 13,000 rpm and 4 °C for 20 min. The supernatant was discarded and the pellet was washed in 1 ml 70% ethanol. After another centrifugation, at 13,000 rpm and 4 °C for 8 min, ethanol was discarded and the pellet was air-dried. Finally, the pellet was resuspended in DEPC water. For tumor samples 150 µl were used, for kidneys 100 µl and for lymph node samples 20 µl.

3.6.2 DNA digestion and RNA concentration measurement

To avoid genomic DNA amplification, a DNA digestion step was performed. Therefore samples were treated with DNA-free™ kit from Ambion, following the manufacturer's protocol. This ensures a specific amplification of cDNA. To determine final RNA concentration tumor, kidney, and lymph node samples were diluted 1:100 in RNAse-free ddH_20. The dilution was then transferred to a cuvette for spectrometry and optical density was measured at a wavelength of 260 nm. RNase free ddH_2O without RNA served as reference indicating the RNA concentration in the solution.

3.6.3 cDNA synthesis

The isolated RNA was transcribed to cDNA by using a reverse transcriptase. Therefore the Revert AidTM First Strand cDNA synthesis kit by Fermentas was used following the manufacture's protocol.

For the cDNA synthesis, Oligo(dT) primers were used, which are complementary to the poly-A tail of mRNAs and bind on their 3' region. After annealing of the primers the reverse transcriptase uses dNTPs to synthesize the corresponding complementary DNA strand. For the synthesis 1 µg RNA and 1 µl primer were used. The following steps were performed according to manufacturer´s guidelines. After incubation for 5 min at 70 °C, 5x reaction buffer, a dNTP mix, 1 µl ribonuclease inhibitor were added and the suspension was incubated for 5 min at 37 °C. After adding 1 µl reverse transcriptase the samples were incubated for 1 h at 42 °C. The

enzymatic reaction was terminated by inactivating the enzyme at 70 °C for 10 min. Afterwards the DNA was amplified by PCR.

3.6.4 Polymerase chain reaction (PCR)

The Polymerase chain reaction is a very sensitive method to amplify any DNA fragment for screening and validating or cloning. Starting with two DNA strands, the total amount of strands after n cycles will be 2^n. Typically, PCR consists of a series of 20-40 repeated cycles. The process is carried out in a thermal cycler, which heats and cools the reaction tubes to achieve the temperatures required at each step of the reaction.

Besides, the DNA template, that contains the DNA region (target) to be amplified, several other basic components are required for a PCR: two primer which determine the beginning and the end of the region to be amplified, a thermally stable DNA polymerase with a temperature optimum at around 70 °C which elongates the newly synthesized DNA strand, deoxynucleoside triphosphates (dNTPs) from which the new DNA strand is synthesized, and a buffer providing a suitable chemical environment.

The PCR process comprises the following steps: denaturation, annealing and elongation. While the denaturation the reaction mix is heated up to 94-98 °C. This causes melting of the DNA template by disrupting the hydrogen bonds between complementary bases, yielding single-stranded DNA molecules. For annealing the temperature is lowered to 45-65 °C and is typically 3-5 degrees below the melting temperature of the primers used. During this step the primers can attach to the single stranded DNA. Afterwards the elongation starts when the DNA polymerase binds to the template where it synthesizes the new DNA strand complementary to the DNA template strand by adding dNTPs, which are complementary to the template in 5' to 3' direction. The time for this step depends on both, the DNA polymerase used and the length of the DNA fragment to be amplified. The optimized temperature in this step is 72 °C.

After the last cycle a final elongation step is performed for 5 min at 72°C. It ensures that any remaining single strand DNA is completely extended. At the end the samples are cooled down to 4 °C to stop the reaction and preserve the DNA.

For efficient primer self-design some rules have to be followed. The length of synthetic oligonucleotides should be between 18-24 base pairs but not longer than 30 bp and the G/C

content must be maintained between 40-60%. It is important that primer sequences are chosen to uniquely select for a region of DNA to avoid the possibility of mishybridization to a similar sequence. Furthermore, palindromes within the primer need to be avoided due to the potential formation of hairpin structures. Additionally pairs of primers should have similar melting temperatures.

In this thesis the following mastermix and reaction program was used:

PCR mastermix:	14.3 µl	H_2O
	5 µl	5x Phusion HF buffer
	1 µl	10 mM dNTP-mix
	0.2 µl	Phusion DNA polymerase
	1 µl	Primer fwd (1:10 diluted)
	1 µl	Primer rev (1:10 diluted)
	1.5 µl	$MgCl_2$
	3 µl	cDNA

PCR program:	1. Denaturation	95 °C; 5 min
	2. Denaturation	95 °C; 30 sec
	3. Annealing	58 °C; 30 sec
	4. Elongation	72 °C 5 sec
	→ 29 repeats, step 2-4	
	5. Elongation	72 °C; 7 min

3.6.5 DNA agarose gel electrophoresis

The DNA gel electrophoresis was used to analyze the DNA fragments of the PCR by their size. Agarose concentration and consequently the density of the agarose gel are dependent on the DNA fragment size. For PCR products, amplified with primers specific for human or murine β-actin, gels with a concentration of 1.6% agarose were used. Therefor agarose was dissolved in 1x TBE buffer. 5 µl ethidium bromide was added per 50 ml buffer. Ethidium bromide intercalates between the DNA bases and enables visualization of DNA bands by UV light. 5 µl

sample buffer was added to the samples and they were filled into the pockets of the gel. Besides samples, a DNA marker was added onto the gel, to measure the size of DNA bands. The size of a DNA fragment is determined in base pairs (bp).

After impressing a direct current field of 80 mA, the negatively charged DNA fragments started to migrate through the agarose polymer network. Due to the fact that larger molecules migrate more slowly through the network like small molecules do DNA bands are fractionated based on their size.

3.7 Preparation of single-cell suspensions and FACS analysis

3.7.1 Preparation of single-cell suspensions

Single-cell suspensions of tumors and lymph nodes were prepared and stained with different antibodies in order to determine the presence of different immune cells by FACS analysis. Therefor tumors and lymph nodes of 4 C33A-RFP tumor-bearing mice, 42 days after tumor cell implantation, were excised, weighted, minced into small pieces with a scalpell and incubated in DMEM High Glucose media supplemented with 2% FCS, 10.000 U/ml Collagenase I and 5 MU/ml DNase I at 37 °C for predigestion. Tumors were incubated for 45 min, lymph nodes for 35 min. Afterwards, tissues were passed through 70 µm nylon mesh filters and transferred to DMEM High Glucose media supplemented with 2% FCS. After centrifugation (1,000 g, 10 min) pellets were resuspended in 2x volume of PBS/2% FCS, regarding to tissue weight. $1x10^6$ cells of the single-cell suspensions were subsequently used for further FACS analysis

3.7.2 Staining of immune cells in tumor and lymph node single-cell suspensions

First of all, to block nonspecific staining, single cells were pre-incubated with 0.5 µg of anti-mouse CD16/32 antibody per one million cells for 20 min on ice. Subsequently, cells were incubated at 4 °C for 40 min in PBS with 2% FCS, after adding 100 µl antibody mastermix of the appropriate monoclonal antibody: α-CD11b- APC and α-CD45- PerCP-Cy5.5 to stain monocytes, α-CD19- PerCP-Cy5.5 to stain B cells and α-CD49b- APC to stain NK cells.

3.7.3 Flow cytometric analyses

Cells were analyzed using Accuri C6 Cytometer and FACS analysis software CFlow Version 1.0.227.4. The following parameters were defined for every measurement:

Counts:	10.000
Core size:	25
Threshold:	400.000
Flow rate:	35 µl/min

Cell debris was excluded from the measurements by defining a proper gate for the cell population of interest by using the forward scatter (FSC), indicating the cell size, and sideward scatter (SSC), indicating the relative cell granularity.

3.7.4 Determining the growth rate of cells of a single-cell suspension

Another $1x10^5$ cells per sample were seeded in 12 well plates in 1 ml DMEM High Glucose media supplemented with 10% FCS and 1% penicillin/streptomycin. After 3, 7 and 9 days cells were harvested using 250 µl trypsin and counted to determine the cell amount.

3.8 Statistical analysis

A two-tailed unpaired Student's *t* test was used for statistical analysis. *P* values of ≤0.05 were considered statistically significant. Asterisks indicate a significant difference between experimental groups (* indicates p ≤0.05; ** indicates p ≤0.01; *** indicates p ≤0.001).

4 Results

This thesis consists of two parts. The first part is about the metastases formation and virotherapy of human C33A cervical cancer cells in an immune compromised nude mouse model, while the second part deals with the murine metastatic model B16F10 in immune competent C57BL/6 mice.

4.1 Characterization of metastases formation and virotherapy in the human C33A cervical cancer model

4.1.1 Enlarged lymph nodes after subcutaneous implantation of C33A cells

So far, the only metastasizing cell line in our lab described was the PC-3 prostate cancer cell line.[92] However, in a study on oncolytic VACV therapy in cervical cancer cells performed by Dr. Simon Schäfer, after subcutaneous implantation of human C33A cells in nude mice an enlargement of lumbar and renal lymph nodes was observed. This enlargement is shown in Figure 4-1.

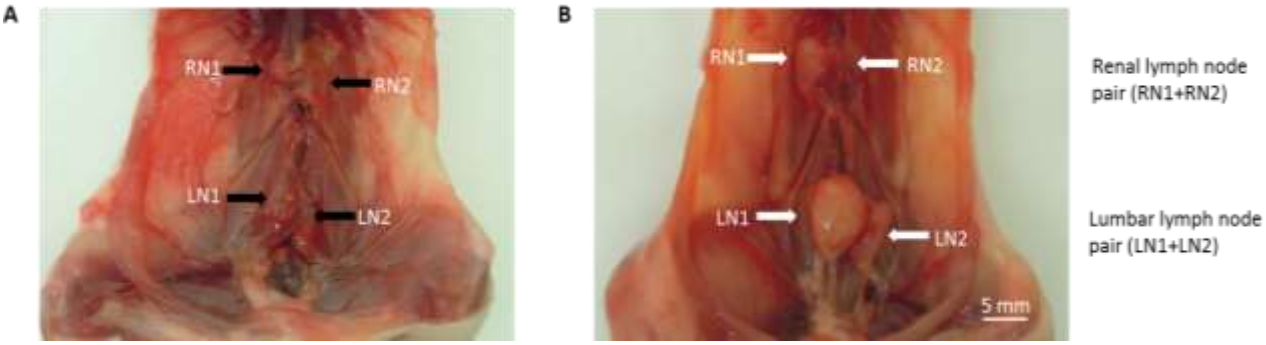

Figure 4-1: Enlargement of lumbar and renal lymph nodes after implantation of C33A cells. [A] Lumbar (LN) and renal (RN) lymph nodes of a non-tumor-bearing mouse (arrows). [B] Lumbar and renal lymph nodes of a tumor-bearing mouse, 35 days after tumor cell implantation (arrows).

To investigate, whether these enlarged lymph nodes are caused by the invasion of human tumor cells or not, lumbar and renal lymph nodes were analyzed for the presence of human cells. This was carried out by RT-PCR of RNA isolated from those lymph nodes and tumors from 4 mice, 42 days post tumor implantation (dpti). After the transcription of RNA into cDNA, the cDNA was amplified using primers for human and murine β-actin, respectively. The specificity of those primers was described previously.[138]

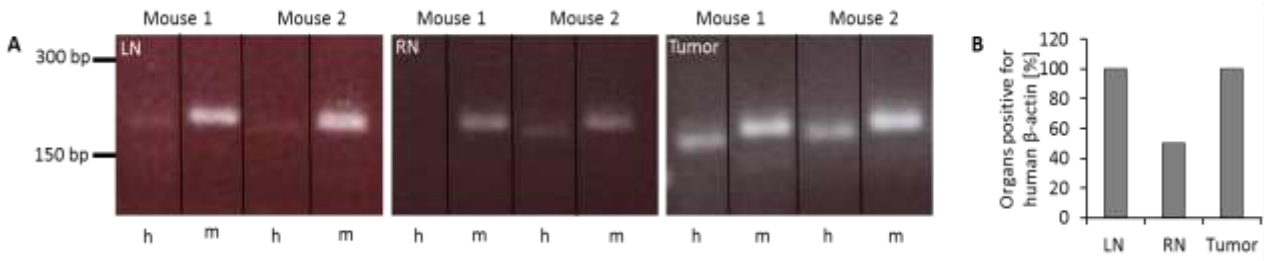

Figure 4-2: RT-PCR of RNA isolated from LNs, RNs, and tumors. RNA was isolated from lumbar and renal lymph nodes and tumors of 4 mice, 42 days after implantation of C33A tumor cells. Afterwards RNA was transcribed into cDNA. cDNA was amplified using either primers for human (h) or murine (m) β-actin. [A] Representative signals of two mice per tested organ are shown (Mouse1 and Mouse 2). [B] Percentage of tested LNs, RNs, and tumors positive for human β-actin.

The signal of human and murine β-actin of LNs, RNs, and tumors of two mice after cDNA amplification with specific primers are shown exemplarily in Figure 4-2[A]. All samples revealed a clear band after amplification of murine β-actin with a size of 216 bp, indicated with an m. Furthermore, it was possible to detect RNA for human β-actin, with a size of 205 bp and indicated with an h, in all tumor samples as well as in all LN samples and at least in 50% of all RNs tested (Figure 4-2 [B]). However, the signal for human β-actin was slightly weaker in all samples compared to the signal of murine β-actin.

Since it was possible to demonstrate that the enlargement of lymph nodes was indeed due to the invasion of human cells, the aim was to characterize the metastatic behavior of these cells. To facilitate the visualization of the metastatic spread more easily, cells were labeled with the red fluorescence protein (RFP). Therefor the cDNA sequence of the red fluorescence protein (*m*RFP1) was inserted by lentiviral transduction into the C33A genome. [139] The resulting cell line C33A-RFP was tested for stable RFP expression by fluorescence microscopy. The images of C33A cells expressing RFP can be seen in Figure 4-3.

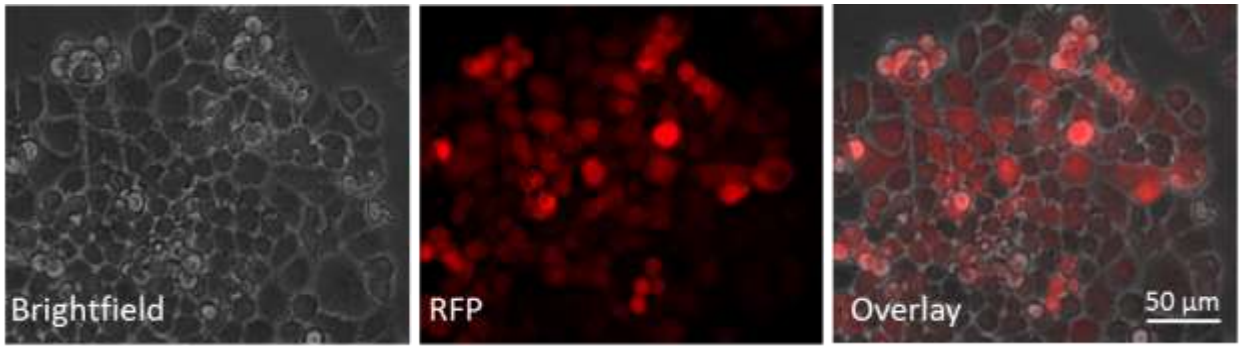

Figure 4-3: RFP-expressing C33A cells: After induction of the red fluorescence protein (RFP) gene by lentiviral transduction into the genome of C33A cells the stable expression of RFP was detectable by fluorescence microscopy.

4.1.2 Comparison of GLV-1h68 infection of C33A and C33A-RFP cells in vitro

Since one aim of this project was to investigate whether GLV-1h68 is an efficient oncolytic tool to treat C33A tumors in mice xenografts, it was necessary to analyze whether the insertion of the RFP gene affects the susceptibility of the cells to viral infection, viral replication and cell lysis *in vitro*. Thus, cell lysis and viral replication after infection with GLV-1h68 in C33A and C33A-RFP cells was compared at different MOI.

4.1.2.1 Insertion of RFP does not impair the replication of GLV-1h68 in C33A–RFP cells

A virus replication assay was performed to determine the ability of GLV-1h68 to efficiently infect and replicate in C33A and C33A-RFP cells in cell culture. For this, cells were infected with the virus at an MOI of 0.1 and 1, respectively, and viral progeny was analyzed at different time points post infection. For better comparison the viral titer was calculated per $1x10^6$ cells.

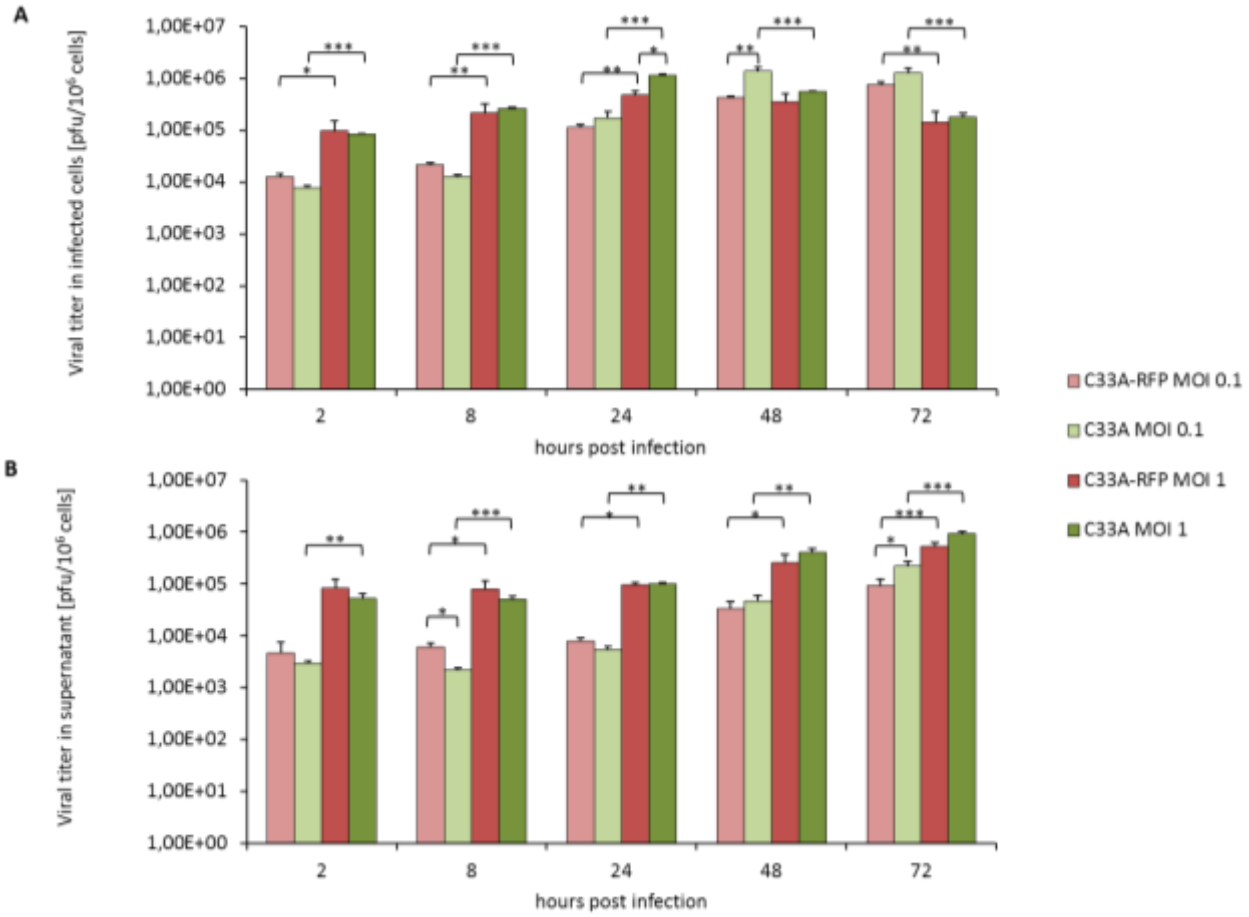

Figure 4-4: Analysis of viral titers in C33A and C33A-RFP cells after infection with GLV-1h68 at a MOI 1 and MOI 0.1, respectively, in cells [A] and supernatants [B]: Cells were seeded in 24-well plates and infected with GLV-1h68 with MOI 0.1 or 1. Two, 8, 24, 48, and 72 hpi cells and supernatants were collected and viral titers were determined in a standard plaque assay. Bar graphs represent mean values and standard deviations of three samples, analyzed in triplicates. (Two tailed, unpaired students t-test: * p >0.05; ** p >0.01; *** p >0.001)

Figure 4-4 [A] displays the viral titer in infected cells at 2, 8, 24, 48 and 72 hours after infection with MOI 0.1 and MOI 1, respectively. In all approaches the viral titer is increasing over time, independent of the cell line or used MOI. The most important finding is that the titers in C33A and C33A-RFP cells were comparable. All in all, the viral titer was slightly higher in C33A cells compared to C33A-RFP cells, except for 2 and 8 hpi, with both MOI 0.1 and MOI 1. Nevertheless, there were no significant differences between the viral titer in both cell lines at any time point, except for 24 hpi in cells infected with MOI 1 and 48 hpi in cells infected with MOI 0.1. The maximal viral titer was reached in MOI 0.1-infected cells 72 hours after infection with $1.3x10^6$ pfu/10^6 cells (± $3x10^5$ pfu/10^6 cells) in C33A cells and $8x10^5$ pfu/10^6 cells (± $8x10^4$ pfu/10^6 cells) in C33A-RFP cells. In contrast, the maximal titer in MOI 1-infected cells was already reached 48

hours after infection with $5.5x10^5$ pfu/10^6 cells (± $2x10^5$ pfu/10^6 cells) in C33A cells and $3.65x10^5$ pfu/10^6 cells (± $1x10^5$ pfu/10^6 cells) in C33A-RFP cells, respectively. Furthermore, the titer in MOI 0.1-infected cells was in the first 24 hours significantly lower compared to cells infected with MOI 1 for both cell lines. At 48 hpi it was the other way round and titers in MOI 0.1-infected cells were significantly higher compared to cells infected with MOI 1, demonstrating an MOI-dependent replication efficiency.

Figure 4-4 [B] shows the viral titer in the supernatant of infected cells. As it was already described for infected cells, the titer was slightly higher in supernatants of infected C33A cells than in the supernatants of C33A-RFP cells. However, also in this case no significant differences were detected, except for 8 hpi, when viral titer in supernatants of C33A-RFP cells infected with MOI 0.1 was significantly higher than those in supernatants of C33A cells, and at 72 hpi, here it was the other way round. For both cell lines and both MOI the viral titer in the supernatant decreased slightly from 2 to 8 hpi but increased afterwards up to 72 hpi reaching titers of $2.2x10^5$ pfu/10^6 cells (± $5.6x10^4$ pfu/10^6 cells) in the supernatants of C33A cells (MOI 0.1), $9.25x10^4$ pfu/10^6 cells (± $3x10^4$ pfu/10^6 cells) in the supernatants of C33A-RFP cells (MOI 0.1), $9.15x10^5$ pfu/10^6 cells (± $1x10^5$ pfu/10^6 cells) in supernatant of C33A cells (MOI 1) and $5.35x10^5$ pfu/10^6 cells (± $9x10^4$ pfu/10^6 cells) in the supernatants of C33A-RFP cells (MOI 1). In the supernatant the titer of cells infected with the higher MOI was significantly higher at every time points than the titer in the supernatant of cells infected with the lower MOI for C33A cells and from 8-72 hpi for C33A-RFP cells.

Taken together the results demonstrate that the insertion of the gene encoding for RFP in the C33A genome did not affect the susceptibility of the cells for viral replication since there were no significant differences in the replication kinetics or efficiency between both cell lines.

4.1.2.2 Insertion of RFP does not impair the GLV-1h68-mediated lysis of C33A–RFP cells

The next step was to determine whether the insertion of RFP has any effects on the ability of GLV-1h68 to efficiently kill and lyse the C33A-RFP cells. Therefore, both C33A and C33A-RFP cells were infected with GLV-1h68 at MOIs of 0.1 and 1 and the relative survival was determined by XTT assay.

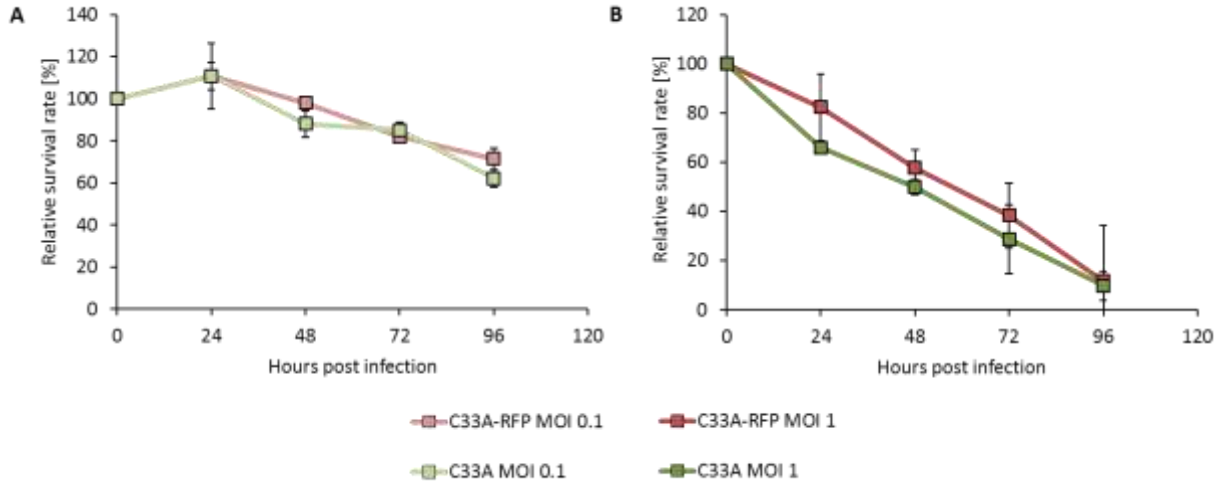

Figure 4-5: Relative survival of C33A and C33A-RFP cells after infection with GLV-1h68 at an MOI of 0.1 [A] and MOI 1 [B], respectively. All values were measured in triplicates 24, 48, 72, and 96 hpi in a XTT assay. At each time point non-infected cells served as a reference and were considered 100% viable. The test was performed in triplicates and repeated twice for both cell lines. (Two tailed, unpaired students t-test: * p>0.05; ** p>0.01; *** p>0.001).

Figure 4-5 shows that C33A as well as C33A-RFP cells were killed with equal efficiency by GLV-1h68 at both MOI 0.1 [A] and MOI 1 [B]. After infection with MOI 0.1 cell number was slightly increasing after the first 24 hours post infection but then cell lysis started and the number of living cells was decreasing down to 62% (C33A) (± 4%) and 70% (± 5%) (C33A-RFP), respectively, 96 hpi. Infection with a MOI of 1 was more efficient compared to MOI 0.1 in both cell lines. From the beginning the cell viability was decreasing continuously leading to only 9% (± 6%) (C33A) and 11% (± 22%) (C33A-RFP) viable cells at 96 hpi. There were no significant differences between both cell lines at both MOI, demonstrating that the insertion of RFP did not affect cell lysis by the vaccinia virus.

4.1.3 Monitoring of tumor and lymph node metastases formation after subcutaneous implantation of C33A-RFP cells

So far, it was demonstrated that the insertion of the gene encoding for RFP did not affect the susceptibility of the cells to viral infection, replication and cell lysis in vitro. By the insertion of RFP a new model was created with which it is possible to monitor the metastatic ability of this cell line in a xenograft mouse model. Therefore, the next step was to characterize in detail the metastatic behavior of C33A-RFP cells. For this, $5x10^6$ C33A-RFP cells were implanted subcutaneously into the right abdominal flank of immunocompromised female nude mice. From

week to week after implantation tumor and lymph node volume was monitored. Additionally, other organs known to be susceptible for metastatic invasion of tumor cells were screened for metastases by histological analysis. These experiments were performed in close collaboration with Dr. Ulrike Donat.

4.1.3.1 Tumor volume is increasing from week to week after implantation of C33A-RFP cells

To monitor the tumor growth after tumor cell implantation, the tumor volume was measured once a week and living mice were imaged to detect the RFP signal of the tumors.

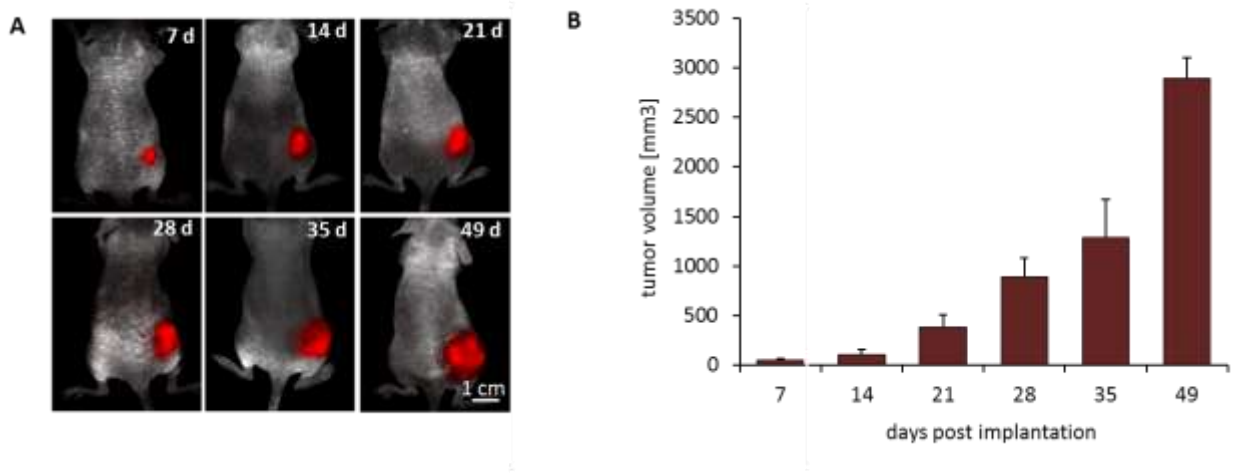

Figure 4-6: Formation of tumors after subcutaneous implantation of 5x10^6 C33A-RFP cells. Tumors of 6 to 7 mice per time point were analyzed (7 and 21 dpti: n=7; 14, 28, 35 and 49 dpti: n=6). [A] Representative images of C33A-RFP tumor-bearing mice at the indicated days post tumor cell implantation. Images of living mice were taken under anesthesia using the Maestro EX Imaging System. [B] Time curse of tumor development. Tumor size was measured with a digital caliper in two dimensions. Graph bars represent average tumor volume of all mice at one time point.

The steady increase of tumor volume is displayed in Figure 4-6. Already 7 dpti the RFP signal of the tumor was detectable and imaging revealed an expansion of RFP signal over time (Figure 4-6 [A]), associated with tumor growth. This was quantified by tumor measurement (Figure 4-6 [B]). Seven dpti the average volume of tumors was about 55 mm^3 (± 16 mm^3) rising up to an average of 3128 mm^3 (± 340 mm^3) at day 49 after implantation.

4.1.3.2 Lumbar and renal lymph node metastases appeared and increased over time according to tumor volume

Lumbar (LN) and renal (RN) lymph nodes were the first nodes which were found to be obviously enlarged like already seen in Figure 4-1. Therefore, those lymph nodes were analyzed primarily; however, the volume cannot be measured in living animals. Hence, every seven days six to seven mice were sacrificed. After opening of the abdomen and removing of the organs enlarged lymph nodes were observed. Lymph node volume was measured in two dimensions and RFP signal of metastasized lymph nodes was monitored and quantified.

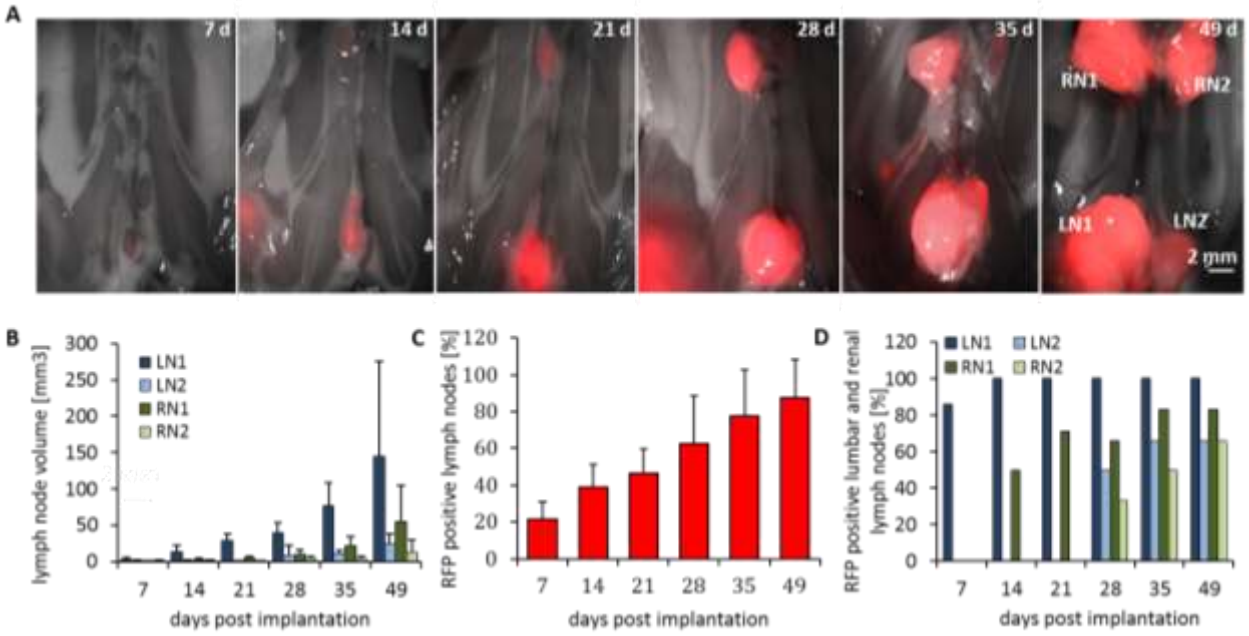

Figure 4-7: Formation of lymph node metastases after subcutaneous implantation of 5x10^6 C33A-RFP cells. Lumbar and renal lymph nodes of six to seven mice per time point were analyzed (7 and 21 dpti: n=7; 14, 28, 35 and 49 dpti: n=6). [A] Representative images of lymph nodes of C33A-RFP tumor-bearing mice at the indicated days post tumor cell implantation. Imaging of lumbar (LN1, LN2) and renal (RN1, RN2) lymph node metastases in the abdomen of tumor-bearing mice was performed *post mortem,* after opening the abdomen and removing organs. [B] Volume of lumbar and renal lymph nodes over time was measured in two dimensions. [C] Percentage of all LNs and RNs positive for RFP over time taken together. [D] Percentage of LN1, LN2, RN1 and RN2, respectively, positive for RFP per time point. Graph bars represent the total percentage of RFP positive LN1, LN2, RN1, and RN2 per time point.

From week to week after s.c. implantation of C33A-RFP cells, a steady increase in the volume of lumbar and renal lymph nodes as well as an increase in the amount of RFP positive lymph nodes was observed (Figure 4-7) accordingly to tumor volume increase. LN1, the lymph node located closest to the primary tumor was increasing first and strongest (Figure 4-7 [A]+[B]) and was the first to reveal a clear RFP signal (Figure 4-7 [D]). Naïve lymph nodes have a size of about 1.1

mm^3 (± 0.9 mm^3) (LN) and 0.4 mm^3 (± 0.03 mm^3) (RN), respectively. After 49 days post implantation, which was the end point of this experiment, lymph nodes were enlarged up to 145 mm^3 (± 130 mm^3) (LN1), 25 mm^3 (± 13 mm^3) (LN2), 56 mm^3 (± 50 mm^3) (RN1) and 12 mm^3 (± 17 mm^3) (RN2), respectively. Moreover, fluorescence imaging revealed a steady increase of the amount of all LNs and RNs positive for RFP taken together, starting with 21% (± 11%) at 7 dpti. The amount increased up to 88% (± 19%) lymph nodes positive for RFP expression at the end of the study (Figure 4-7 [C]). Furthermore, the percentage of RFP-positive LN1, LN2, RN1 and RN2 was analyzed per time point. The order in which RFP signal was detectable in the specific lymph nodes was accordingly to volume increase, as seen in (Figure 4-7 [A]). At day 7 post implantation 86% of all LN1s detected were positive for RFP, whereas no RFP signal was detectable in LN2, RN1 or RN2. 14 days post tumor cell implantation all detected LN1s (100%) and 50% of RN1s were positive for RFP. In LN2 and RN2 the RFP signal was first detectable at days 28 after tumor cell implantation. At the end 100% of LN1, 83% of RN2 and 67% of LN2 and RN2 displayed a RFP fluorescence signal.

4.1.3.3 Lymph nodes at distant sites can reveal RFP signal

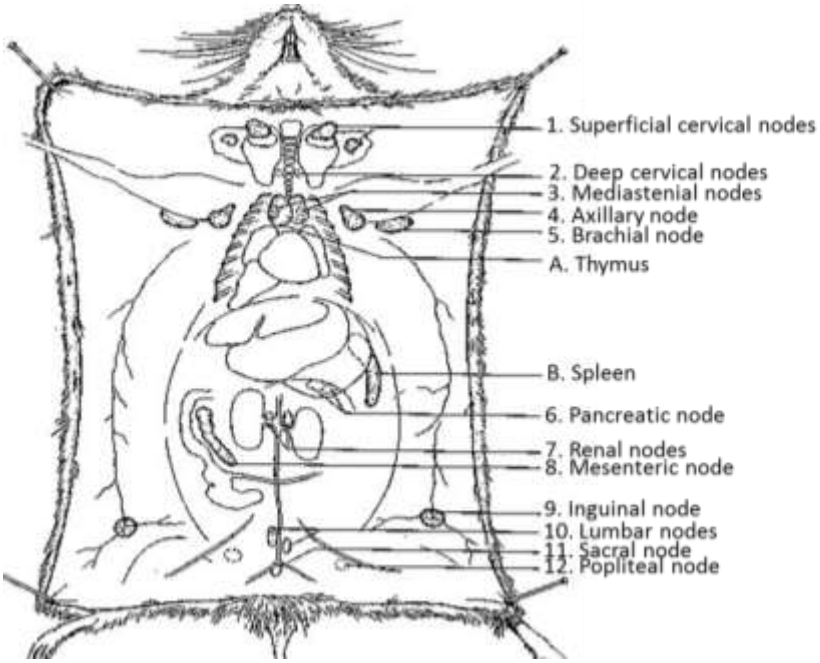

Figure 4-8: Lymph nodes of a mouse: Displayed is the anatomic localization of different lymph nodes (1-12) and lymphoid organs (A+B) of a mouse. The listed lymph nodes were further analyzed for the presence of RFP, indicating metastasis (modified from [140]).

Like already described, the enlargement of LNs and RNs was visible to the naked eye. Nevertheless, it was necessary to analyze whether other lymph nodes got metastasized as well. Therefore, other lymph nodes beside LN and RN were checked by fluorescence imaging for the presence of RFP signal as well. The anatomic localization of those lymph nodes is displayed in Figure 4-8.

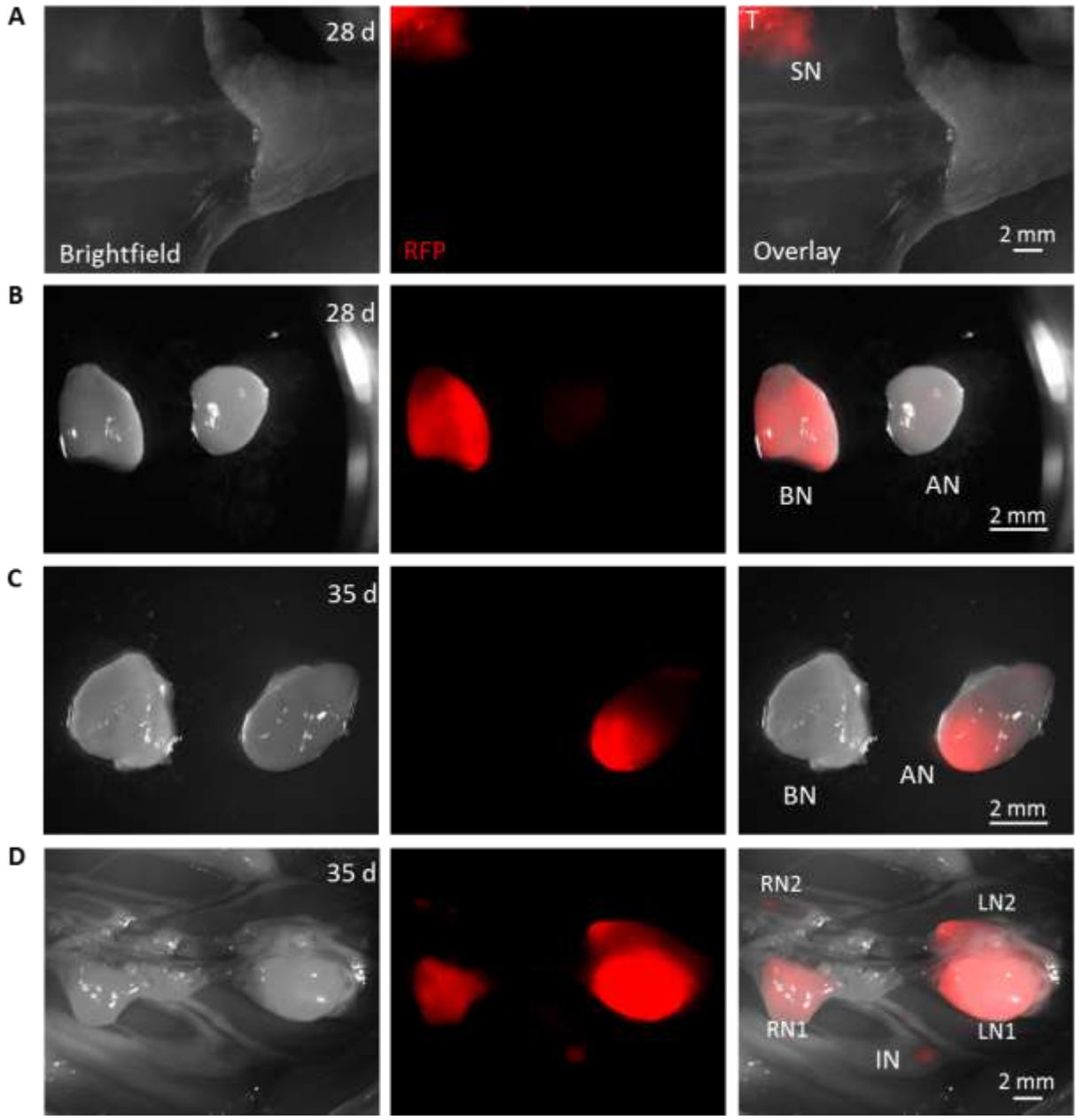

Figure 4-9: Formation of lymph node metastases at distant sites. Mice were analyzed for additional lymph node metastases. Brightfield and RFP fluorescence images were taken and merged to an overlay. Exemplary images are displayed. Metastases were detected in sacral (SN) [A], brachial (BN) [B], axillary (AN) [C] and inguinal (IN) [D] lymph nodes 28 and 35 days after implantation. Furthermore, displayed in [A] is a small part of the tumor (T) and the LN and RN pairs in [D].

RFP signal was detected in sacral (SN, Figure 4-9 [A]), brachial (BN, Figure 4-9 [B]), axillary (AN, Figure 4-9 [C]) and inguinal (IN, Figure 4-9 [D]) lymph nodes. Lymph node metastases at distant sites were observed at day 28 and 35 post tumor implantation. Overall metastasized SN were found in 5 mice, AN and BN in 2 mice each and metastasized IN was observed in 3 mice. All of these lymph node metastases were located at the tumor-bearing body side.

Generally, after subcutaneous implantation of C33A-RFP cells lymph node metastases do occur also in other lymph nodes than LN and RN but this is no common occurrence and does not happen with a high presumption.

4.1.3.4 Tumor cells migrate via the lymphatic and haematogenous route

The next step was to analyze how the metastatic spread of the C33A-RFP cells might occur. Therefore fluorescence imaging of the LN-RN containing part of the mouse body where big lymph and blood vessels are located, has been performed. Fluorescence imaging revealed in some mice a strong RFP signal in vessel shaped structures between lumbar and renal lymph node pairs (Figure 4-10 [A]). To further analyze this signal and find out whether these structures are lymph or blood vessels cryo cross sections of this part were performed and staining with an α-LYVE1 antibody to mark lymphatic vessels was done. Furthermore a staining with Hoechst was performed to label nuclei.

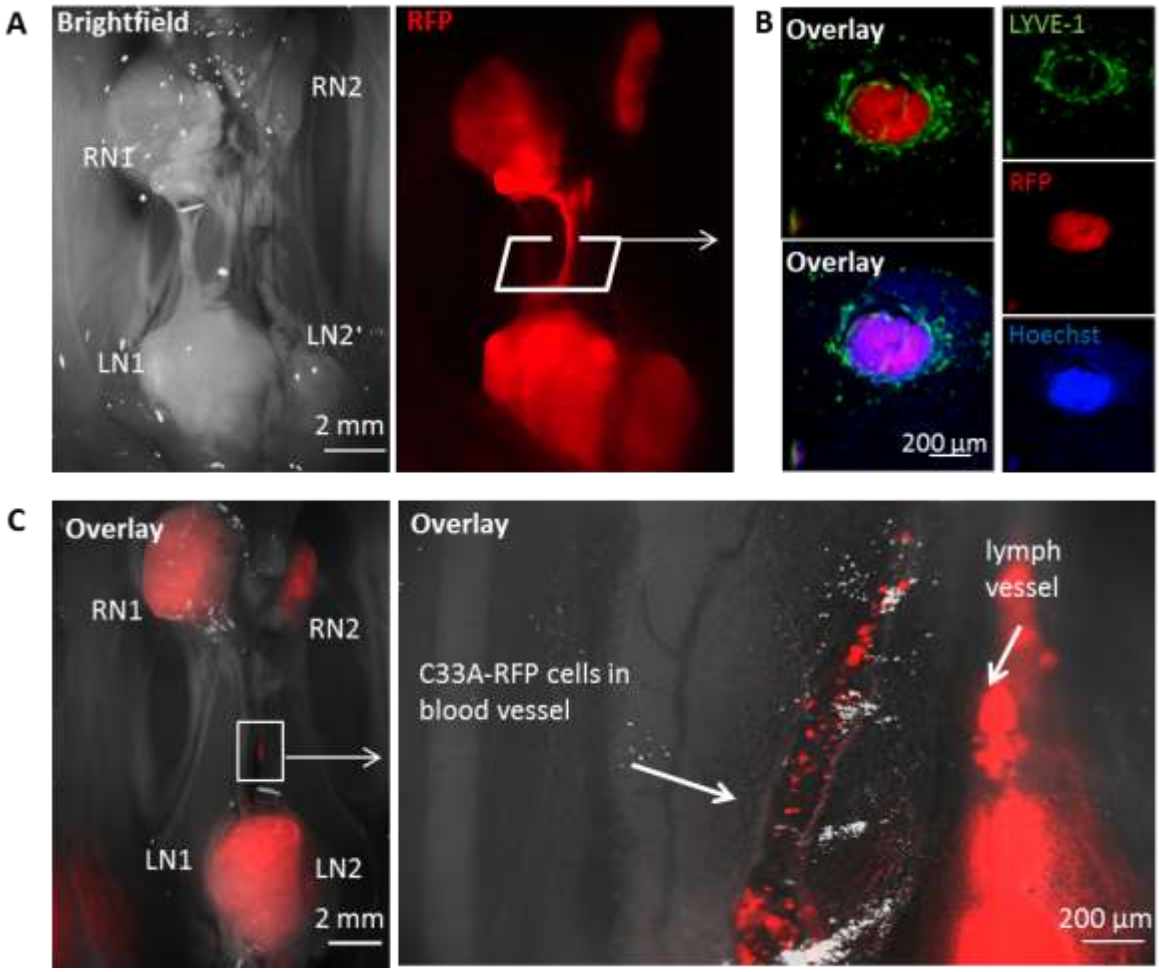

Figure 4-10: Metastatic migration of the C33A-RFP cells in tumor-bearing nude mice. [A] Migration of C33A-RFP cells in a vessel connecting LN1 and RN1 42 dpti was observed. [B] A cryo cross section of the LN-RN connecting vessel was prepared and stained with α-LYVE 1 antibody (green). RFP (red) and Hoechst-positive (blue) tumor cells were located within the stained lymph vessel. [C] Cells migrated in blood vessel (left arrow) and in a nearby located lymph vessel (right arrow).

Figure 4-10 [B] shows the cross section of a vessel between LN and RN. The image clearly reveals the localization of RFP- and Hoechst positive C33A tumor cells in the LYVE1-positive lymphatic vessel demonstrating tumor cell migration from lymph node to lymph node via the LN-RN connecting lymphatic vessel. Besides, RFP-positive tumor cells were also detectable in the erythrocyte containing blood vessel which is located next to this lymph vessel (Figure 4-10 [C]), demonstrating that the C33A tumor cells also use the haematogenous route additionally to the lymphatic route of spreading.

4.1.3.5 RFP signal is found in lungs and kidneys confirming the haematogenous spread of tumor cells

To confirm the spreading via the haematogenous route, described in the previous chapter, organs like lung, kidney, spleen and liver were screened for the presence of metastases by fluorescence microscopy.

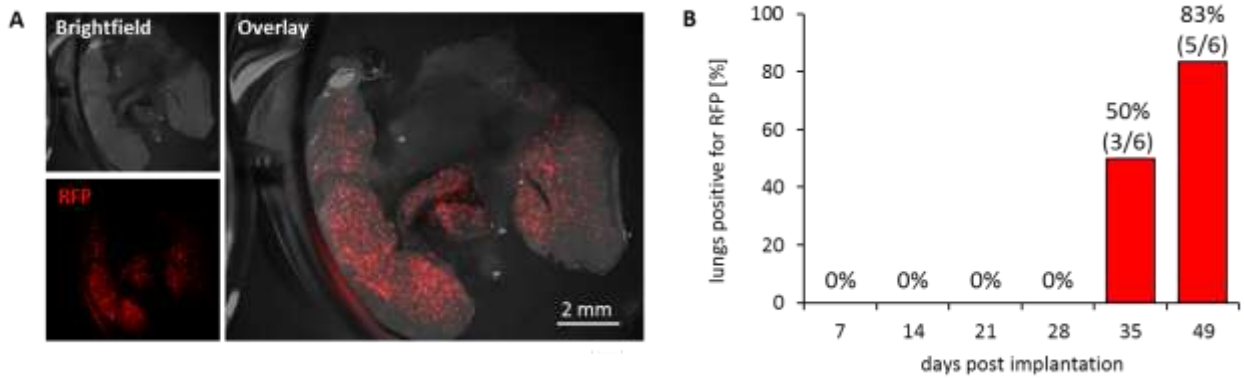

Figure 4-11: RFP signal in lungs of C33A-RFP tumor-bearing mice. Lungs of six to seven mice per time point were examined (7 and 21 dpti: n=7; 14, 28, 35 and 49 dpti: n=6). [A] Representative image of a lung 42 dpti. Brightfield and RFP fluorescence image were merged to an overlay. [B] Percentage of lungs tested positive for RFP spots over time.

Fluorescence microscopic studies revealed RFP signals in lungs (Figure 4-11) and kidneys (Figure 4-12) of C33A-RFP tumor-bearing mice. Up to day 28 post tumor cell implantation no lung was found to be positive for RFP, whereas at day 35 3 out of 6 (50%) and at day 49 5 out of 6 (83%) lungs were found to be positive for RFP (Figure 4-11 [B]). Thereby the RFP signal was distributed equally over the whole lung in spot like patterns (Figure 4-11 [A]).

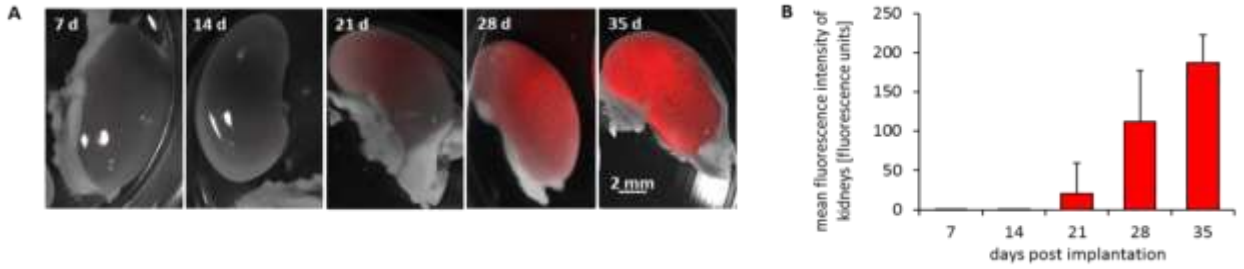

Figure 4-12: RFP signal in kidneys of C33A-RFP tumor-bearing mice. Six to seven mice were analyzed per time point (7 and 21 dpti: n=7; 14, 28 and 35 dpti: n=6) [A] Representative images of RFP signal in kidneys at the indicated days post tumor cell implantation. [B] Mean fluorescence intensity of the RFP signal in kidneys of C33A-RFP tumor-bearing mice over time was calculated using Image J, after RGB-images were converted into 8-bit gray scale with an intensity range from 0–255 using Photoshop.

In kidneys from days 14 post implantation on, RFP signal was found in almost all kidneys (Figure 4-12) of the C33A-RFP tumor-bearing mice. The signal intensity was increasing over time from 0.5 (± 0.7 units) fluorescence units at day 14 up to 187 (± 34 units) fluorescence units at the end of the study. In contrast to the RFP distribution in the lungs, the RFP signal in kidneys was not distributed in spot-like patterns, but equally throughout the whole kidney.

4.1.3.6 Histological analysis of lungs and kidneys revealing the origin of RFP signal

To further analyze the histological structures of RFP-positive kidneys and lungs, cryo and agarose sections of these organs and tumors and lymph nodes, respectively, were performed and stained with an α-CD31 antibody for labeling blood vessels and with Hoechst dye for labeling nuclei. Furthermore, a RT-PCR of RNA isolated from kidneys from C33A-RFP tumor-bearing mice 42 dpti was performed with primer for human and murine β-actin.

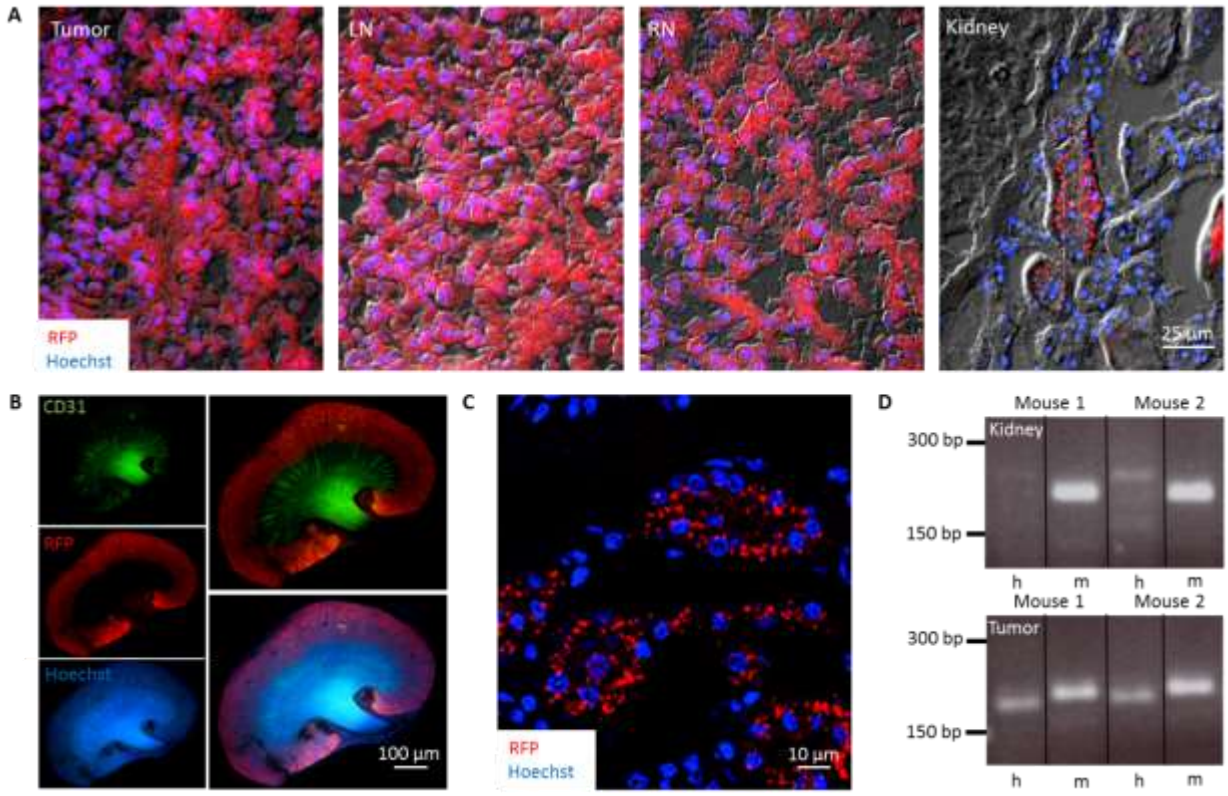

Figure 4-13: Histological analysis of tumors, LNs, RNs and kidneys of C33A-RFP tumor-bearing mice. Nuclei were stained with Hoechst dye (blue) and blood vessels with an α-CD 31 antibody (green). Representative images of tumors, lymph nodes and kidneys are displayed. [A] Overlays of bright field, RFP and Hoechst images of 10 µm cryo sections of tumor, LN, RN and kidney 31 dpti. [B] Images of 70 µm agarose sections of a kidney 31 dpti, stained with α-CD31 antibody and Hoechst dye. [C] 10 µm kidney cryo sections stained with Hoechst dye.[D] RT-PCR of RNA isolated from kidneys from C33A-RFP tumor-bearing mice 42 dpti was performed with primer for human (205 bp) and murine β-actin (216 bp). The

representative results of 2 mice are shown. RT-PCR of RNA isolated from tumors of C33A tumor-bearing mice is displayed as a control.

Histological analyses demonstrated a location of renal RFP signals mainly in the cortex of the kidney whereas CD31 labeled blood vessels were primarily located in the medulla and pelvis (Figure 4-13 [B]). Furthermore, higher magnification revealed that the RFP signal in C33A-RFP tumor cells in tumors and lymph nodes (LN and RN) showed a strong organized structure while this was not observed in kidneys (Figure 4-13 [A]). In the kidneys RFP is accumulated in nephrons, whereby RFP seemed to be located cell-independently in an aggregated pattern (Figure 4-13 [C]). Furthermore RT-PCR of kidney RNA of 2 exemplary mice is shown in Figure 4-13 [D] and revealed a strong and clear signal for murine (m) but not for human (h) β-actin. Additionally, the RT-PCR of C33A tumor RNA is displayed to illustrate the presence of both, the signal for murine and for human β-actin.

All these findings together lead to the conclusion, that the RFP signal in the kidneys is most likely not due to the invasion of intact human tumor cells, but due to the deposition of cell-independent RFP-fragments.

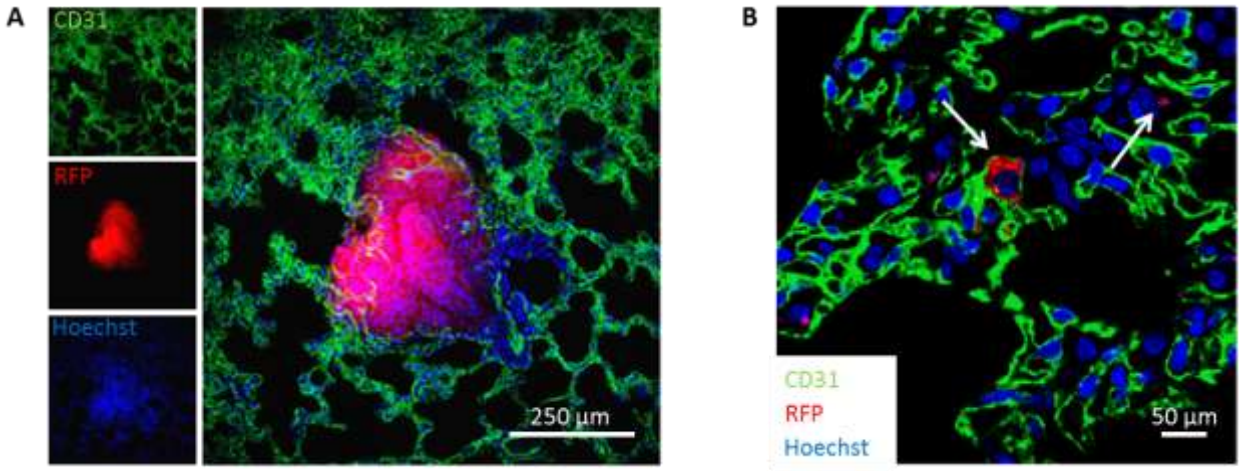

Figure 4-14: Histological analysis of lungs of tumor-bearing mice 42 dpti. 100 µm agarose sections were stained with Hoechst dye (blue) and α-CD 31 antibody (green). [A] Representative image of a lung metastasis. [B] Lung tissue containing RFP positive tumor cells within a blood vessel (left arrow) and cell-independent RFP fragments (right arrow).

In contrast to the observations in kidneys, in lungs micrometastases were detected (Figure 4-14 [A]). Additionally, both, RFP-positive cells within blood vessels in the lung tissue and cell-independent RFP spots similar to those observed in the renal cortex of the kidneys were visualized (Figure 4-14 [B]).

Overall the hypothesis of haematogenous spread by C33A-RFP tumor cells was confirmed by the fact that RFP fragments, RFP-positive cells or micrometastases consisting of a huge amount of tumor cells were detected in lungs. In contrast to that, no metastases were found in kidneys.

4.1.4 Combating tumors and metastases with the oncolytic vaccinia virus GLV-1h68

Since it was shown previously, that GLV-1h68 is able to efficiently infect, replicate in and lyse C33A-RFP cells in cell culture, the oncolytic virotherapy as a novel treatment option for C33A-RFP tumors and metastases was analyzed.

Therefore, $5x10^6$ C33A-RFP cells were implanted subcutaneously into the right abdominal flank of immunocompromised female nude mice. 21 days after tumor implantation one single dose of $1x10^7$ pfu GLV-1h68 was injected intravenously into the tail vein. PBS injected mice served as a control. Every week mice were analyzed for tumor volume and metastatic burden.

4.1.4.1 Influence of vaccinia virus GLV-1h68 on C33A-RFP tumors

To monitor the oncolytic effect of the virus tumor volume of GLV-1h68-injected and control mice (PBS-injected) was measured and compared twice a week. Furthermore, mice were imaged every week to quantify RFP and GFP signal of the tumor and the virus.

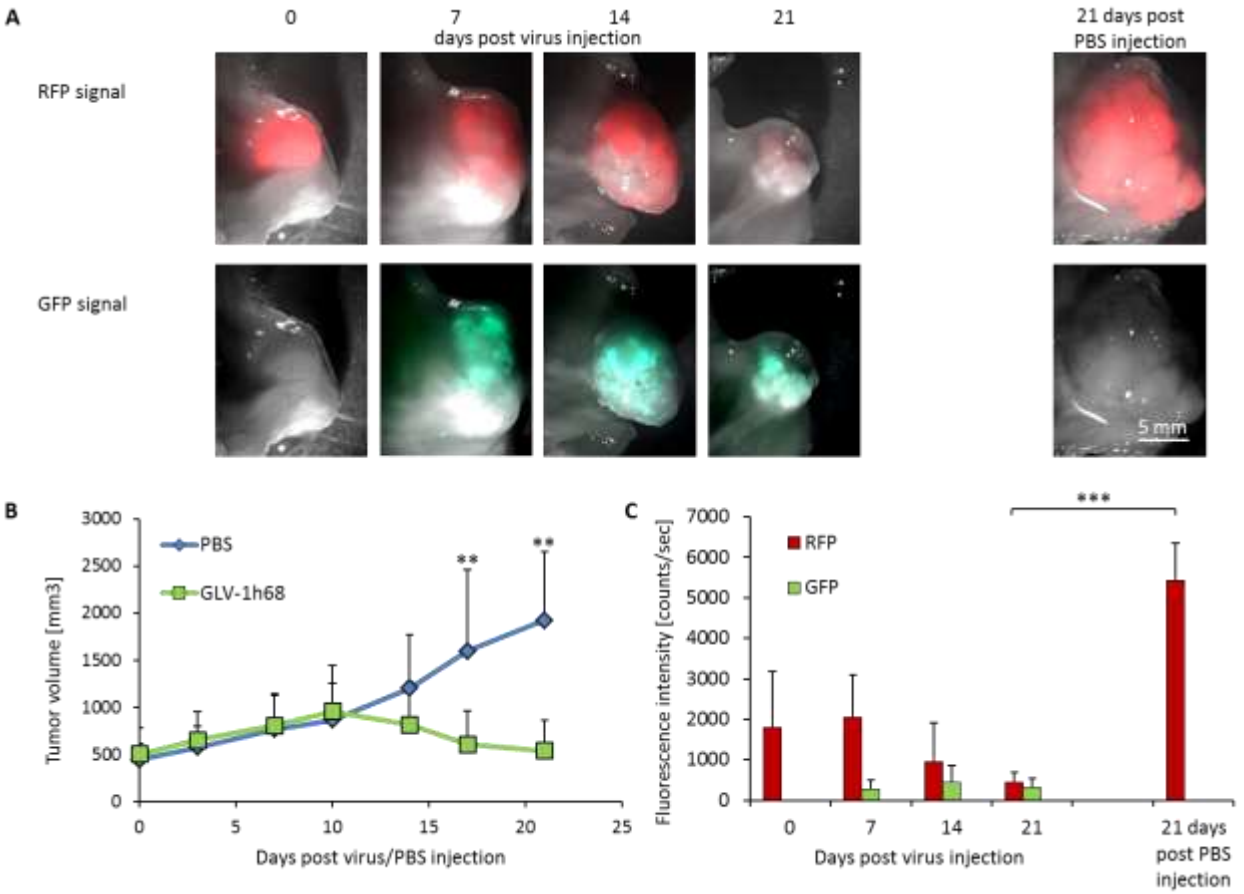

Figure 4-15: Regression of C33A-RFP tumors after virus injection, in accordance with regression of RFP and GFP signal. Virus or PBS was injected, when tumors reached a volume of about 500 mm^3. [A] Tumors of 5 mice were analyzed 0, 7, 14, and 21 days after virus administration, or 21 days after PBS administration. Representative images of C33A-RFP tumors at the corresponding time point are displayed. Upper row shows RFP signal caused by tumor cells. Lower row shows GFP signal in the tumor caused by GFP-expressing GLV-1h68. [B] Time curve of tumor size, measured with a digital caliper in two dimensions. Tumor size of 5 virus-injected and 5 PBS-injected mice was measured twice a week over 21 days after virus injection. [C] RFP and GFP signal was measured for 5 mice of each group at each time point. RFP and GFP signal of the surface tumor area was quantified using the Maestro EX Imaging System. (Two tailed, unpaired students t-test: * p>0.05; ** p>0.01; *** p>0.001)

Tumor regression after virus administration in accordance with the development of the RFP as well as the GFP signal caused by tumor cells and virus, respectively, is displayed in Figure 4-15. Within the first days after virus administration, both tumor size and RFP signal, caused by tumor cells, is increasing (Figure 4-15 [A]), while at 21 dpi tumors were very small and RFP signal was weaker. In accordance, the GFP signal, caused by the tumor-colonizing GLV-1h68 was increasing at early time points as well, and finally decreased up to 21 dpi. All three factors, tumor size, RFP signal and GFP signal were quantified (Figure 4-15 [B]+[C]). Tumor size measurement (Figure 4-15 [B]) revealed that after virus or PBS injection tumors of both groups continued to grow

until day 10 post injection. After this time point, tumor volume of mice in the virus-injected group started to shrink reaching almost the initial size at day 21 after virus injection. From day 17 dpi on, tumors of the virus-treated group were with 607 mm^3 (±350 mm^3) significantly smaller than tumors of the PBS-treated group with 1595 mm^3 (± 786 mm^3), which increased continuously reaching 2000 mm^3 (± 730 mm^3) at the end of this study.

Corresponding to the tumor development, the RFP signal in tumors was first increasing as well, up to 7 days (Figure 4-15 [C]). Afterwards RFP signal dropped down until the end of the study. The signal intensity at 21 days after virus/PBS injection was in tumors of PBS-treated mice significantly higher compared to tumors of virus-injected mice at the same time point. In parallel, the fluorescence intensity of GFP signal was increasing up to 14 dpi and decreased to 21 dpi, mainly caused by the lysis of tumor cells due to virus infection and therefore the clearance of the virus.

4.1.4.2 Influence of GLV-1h68 on C33A-RFP lymph node metastases

In order to analyze the influence of GLV-1h68 on the metastatic burden every 7 days 8 mice were examined. Lymph node volume was measured in two dimensions and RFP signal was monitored using the Maestro EX imaging system.

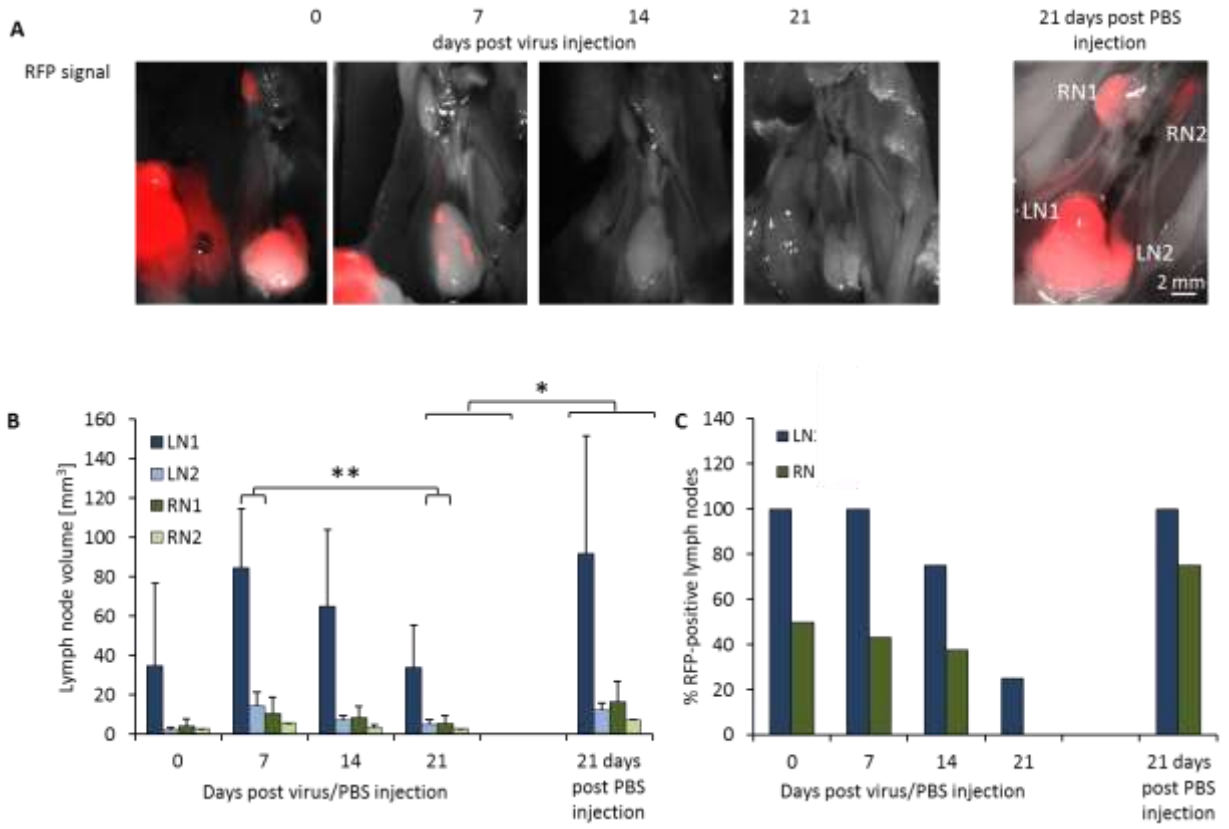

Figure 4-16: Influence of GLV-1h68 on the metastatic burden in LN and RN of C33A-RFP tumor-bearing mice after virus injection. Eight mice per time point were analyzed. [A] Representative images of RFP signal in LNs and RNs every seven days after virus injection and 21 days after PBS injection [B] Volume of lumbar and renal lymph nodes over time was measured in two dimensions. (Two tailed, unpaired students t-test: * p>0.05; ** p>0.01; *** p>0.001) [C] Percentage of RFP positive lumbar and renal lymph nodes.

Reduction of metastatic burden in lymph nodes after injection of one single dose GLV-1h68 is pictured in Figure 4-16. It is clearly visible, that after virus administration RFP signal was drastically decreasing in LNs and RNs (Figure 4-16 [A]). Additionally the volume of these lymph nodes was obviously smaller at 21 dpi compared to lymph nodes at the day of virus administration and compared to lymph nodes of the PBS treated control group at the same time point. Detailed quantification revealed that the volume of all four lymph nodes (LN1, LN2, RN1 and RN2) increased within the first 7 days after virus injection (Figure 4-16 [B]). Afterwards the volume started to decrease according to tumor volume, described in the previous chapter. 21 days after virus injection the volume of all four lymph nodes was significantly smaller as the ones 7 days after virus injection or the lymph node volume of untreated control mice at the same time point. Furthermore the amount of RFP-positive lymph nodes decreased over time from 100% RFP-positive LN and 50% RFP-positive RN at the day of virus injection down to 25%

RFP positive LN and 0% RN. Whereas the amount of RFP positive lymph nodes in untreated control mice increased up to 100% of all LNs and 75% of all RNs (Figure 4-16 [C]).

4.1.4.3 Regression of RFP signal in kidneys after virus administration

After the regression of metastatic burden in lymph nodes was demonstrated, the next step was to analyze the influence of virus administration on the amount of RFP in kidneys of tumor-bearing mice. Therefore the RFP signal in kidneys was measured and quantified.

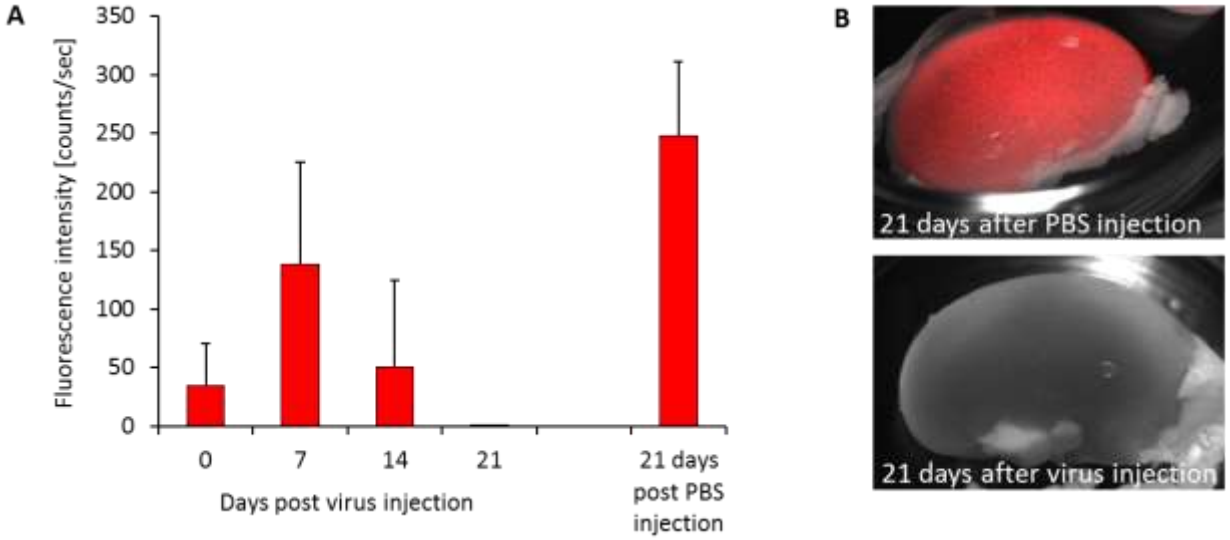

Figure 4-17: Regression of RFP signal in kidneys of C33A-RFP tumor-bearing mice after GLV-1h68-injection. Kidneys of eight mice per time point were analyzed. [A] RFP signal of kidneys was measured and quantified using the Maestro EX Imaging System. [B] Representative images of a kidney of a tumor-bearing mouse 21 days after PBS (upper image) or GLV-1h68 injection (lower image).

After administration of one single dose GLV-1h68 the RFP signal in the kidneys was increasing from days 0 to day 7 after injection, from 35 counts/sec (± 36 counts/sec)up to 140 counts/sec (± 86 counts/sec) (Figure 4-17 [A]), consistently with the observations already described for tumors or lymph node metastases. Further on, the RFP signal was decreasing till the end of the study, and at 21 dpi no RFP signal was detectable in any of the kidneys. In contrast, RFP signal in kidneys of PBS-treated mice was increasing up to 250 counts/sec (± 63 counts/sec) at 21 dpi. Kidneys of a C33A-RFP tumor-bearing mouse treated with PBS showed a strong RFP signal all over the whole organ, whereas in kidneys of virus treated mice at the same time point no RFP signal was detectable at all (Figure 4-17 [B]).

4.1.5 Tumor and lymph node colonization by GLV-1h68

For the PC-3 metastatic model a preferential colonization of lymph node metastases compared to primary tumor by GLV-1h68 was demonstrated.[137] The aim of the following experiment was to investigate whether this colonization order is also true for the C33A model and whether this might be a general colonization strategy. Therefore, $5x10^6$ C33A-RFP cells were implanted subcutaneously into the right abdominal flank of nude mice. 40 days after implantation one single dose $1x10^7$ pfu GLV-1h68 was injected into the tail vein. One, 3 and 7 days after virus injection 9 mice per time point were analyzed in plaque assay and histological analyses.

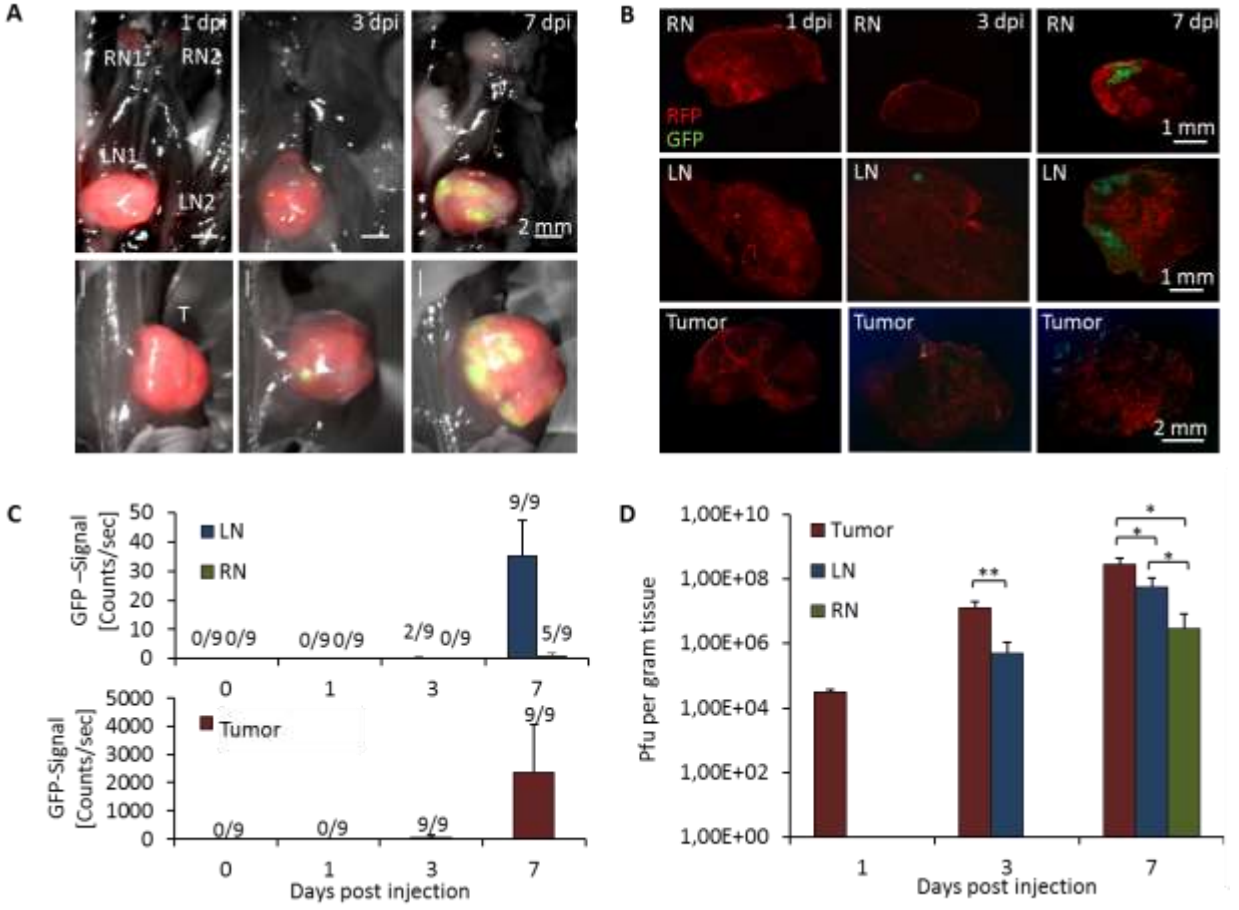

Figure 4-18: Colonization of tumors and lymph node metastases by GLV-1h68. [A] Representative images of lymph node metastases (LN1, LN2, RN1, RN2) and tumors (T) 1, 3 and 7 days after virus injection. Images were taken with the Maestro EX Imaging System. RFP caused by tumor cells (red) and GFP caused by virus (green) is displayed. [B] Representative images of 70 µm agarose sections. RFP positive tumor cells (red) and virus infected areas (green) are displayed. [C] RFP signal of lymph nodes (upper row) and tumors (lower row) was measured and quantified using the Maestro EX Imaging System. [D] Plaque forming units per gram tissue were determined by standard plaque assay. (Two tailed, unpaired students t-test: * p>0.05; ** p>0.01; *** p>0.001)

Fluorescence imaging studies showed GFP signal in lymph node metastases and tumors first at day 3 after virus administration (Figure 4-18 [A]+[C]). Whereas all tumors were positive for GFP at this time point, only 2 out of 9 LNs were positive. The mean fluorescence intensity of tumors was 46 counts/sec (± 106 counts/sec) while the mean intensity in LNs was only 2 counts/sec (± 0.2 counts/sec), increasing to 2350 counts/sec (± 1709 counts/sec) in tumors at day 7 and 35 counts/sec (±12 counts/sec) in LN at day 7. At this time point all LNs were positive for GFP. Additionally, RNs were first found to be GFP positive at this time point. In 5 out of 9 RNs, GFP signal was detectable with an average fluorescence intensity of 3 counts/sec (± 0.9 counts/sec). In contrast to whole body imaging, agarose sections of lymph node metastases and tumors revealed, that first GFP spots were detectable in tumors already 1 day after virus administration (Figure 4-18 [B]). GFP signal is caused by GLV-1h68 and is therefore a hint for successful viral colonization within the tissue. In LNs and RNs the GFP-signal was first detectable 3 dpi and 7 dpi, respectively. These findings were also confirmed by standard plaque assay of lymph nodes and tumors. By this, virus was detectable in tumors already 1 day after virus administration as well. At this time neither in LN nor in RN virus was detected. Plaque assay revealed again virus in LNs 3 days after virus injection and in RNs 7 days after injection. With $4.9x10^7$ pfu/gram tissue ($\pm 4.8x10^7$ pfu/gram tissue) and $3x10^6$ pfu/gram tissue ($\pm 5.4x10^6$ pfu/gram tissue) the virus titer in LN and RN was significantly lower compared to virus titer in tumors with $2.8x10^8$ pfu/gram tissue ($\pm 1.6x10^8$ pfu/gram tissue). Furthermore, virus titer was significantly lower in RNs compared to LNs.

Taken together, in contrast to the PC-3 metastatic model, for the C33A model a preferential colonization of the primary tumor compared to lymph node metastases by GLV-1h68 was observed.

4.1.6 Histological and FACS analysis of C33A tumors and lymph nodes

To analyze the characteristics of tumors and lymph nodes and to determine whether there are differences between tumors and lymph node metastases, which explains the preferential colonization of tumors by GLV-1h68, histological and FACS analyses were performed.

4.1.6.1 Higher necrotic areas in tumors compared to lymph nodes

It is postulated, that low levels of necrotic tissue seemed to be favorable for GLV-1h68-replication.[137] Therefore the necrotic area in tumors and lymph node metastases was determined. Hence 10 µm cryo sections of tumors, LNs and RNs of 4 mice, 35 days after implantation, were stained with Hoechst dye to label nuclei and by that viable, non-necrotic tissue. The necrotic area was determined by analyzing the fluorescence intensity of two slices each per sample. Necrotic area is characterized by non/weak stained regions.

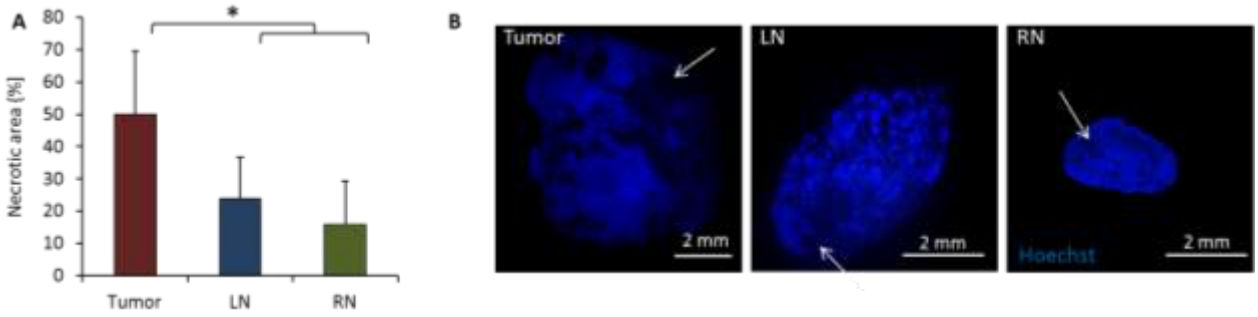

Figure 4-19: Amount of necrotic area in tumors, LNs and RNs 35 days after implantation. [A] Percentage of non-necrotic area in tumors, LNs and RNs was determined calculating the Hoechst stained area of cryo sections using ImageJ. The necrotic area was afterwards calculated by subtracting this area from 100% whole area. All in all the tumors of 8 mice were analyzed with 2 different slices per tumor. (Two tailed, unpaired students t-test: * p>0.05; ** p>0.01; *** p>0.001). [B] Representative images of tumor, LN and RN. Arrows indicate examples for the necrotic area.

Analysis of the sections revealed a significant difference in percentage of necrotic area between tumors and lymph node metastases (Figure 4-19 [A]). In primary tumors significantly more necrotic regions were detected compared to lymph nodes. Approximately 50% (± 19%) of the tumor tissue was necrotic, in contrast to 24% (± 12%) of the LN and 16% (± 13%) of the RN tissue, respectively. Additionally, there were no significant differences between LNs and RNs measurable. In fluorescence images, necrotic areas are displayed as regions with weaker Hoechst staining (Figure 4-19 [B]).

4.1.6.2 Higher proliferative status in lymph node metastases compared to primary tumor

Additional to the necrotic area, the proliferative status of tumor cells does influence the viral replication. Hence the proliferative status of tumor and lymph node cells was determined. This was on the one hand done by staining of Ki67 which is a cell proliferation marker. Therefor 10 µm cryo sections were prepared and stained with an α-Ki67 antibody. The average fluorescence

intensity of Ki67 positive regions was calculated in slices of primary tumors, LNs and RNs. On the other hand, single cell suspensions of primary tumor and lymph node metastases of 5 mice 42 dpti were prepared and $1x10^5$ living cells were seeded in triplicates into a 12 well plate. Four, 7 and 9 days after seeding, cells were harvested and cell number was counted.

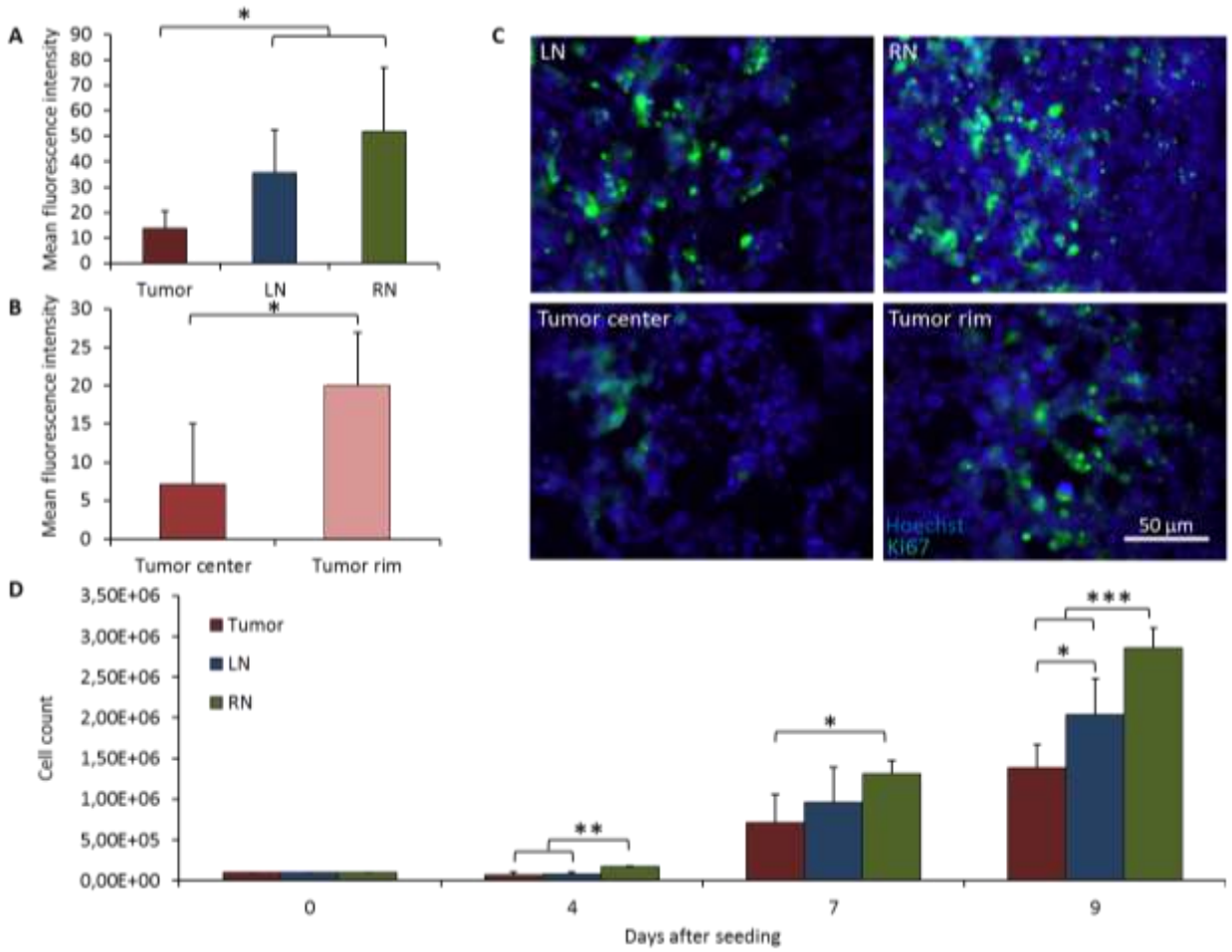

Figure 4-20: Proliferative status of cells in primary tumor and lymph node metastases. [A] C33A-RFP tumors, LNs and RNs of five mice were excised 42 dpti. 10 µm cryo sections were prepared and stained with α-Ki-67 antibody. The Ki67 positive area of each five images of two sections per sample for LN and RN was calculated using Image J. For tumor samples 10 images were taken, 5 from tumor center and 5 from tumor rim. Mean value were calculated. [B] Ki67 positive area was subdivided into tumor center and tumor rim. [C] Representative images of LN, RN, tumor center and tumor rim, stained with Hoechst (blue) and an α-Ki-67 antibody (green). [D] Single-cell suspensions of tumors, LN and RNs, excised 42 dpti, were prepared and $1x10^5$ viable cells per sample were seeded into 12 well plates. Each sample was seeded in triplicates. 4, 7 and 9 days after seeding cell number was counted (Two tailed, unpaired students t-test: * p>0.05; ** p>0.01; *** p>0.001).

Differences in fluorescence intensity of Ki67 stained areas were observed between tumors and lymph node metastases. (Figure 4-20 [A]+[C]) The mean fluorescence intensity was significantly higher in lymph nodes compared to the primary tumor. However, no remarkable differences

between LNs and RNs were found. Additionally, there were significant differences within the tumor itself. The mean fluorescence intensity and therefore the detected Ki67 amount in the center of the tumor was lower than in the tumor rim, indicating a higher proliferation rate in the rim compared to the center (Figure 4-20 [B]+[C]).

Moreover the amount of cells after seeding single-cell suspensions of tumors, LNs and RNs was determined. From day 4 on cell number of RNs was significantly higher than cell number of tumors or LNs. Until day 9 no significant differences between LNs and tumors were observed, but at this time point the amount of LN cells was higher than the amount of tumor cells.

All this findings indicate a higher proliferation rate in lymph node metastases, especially in RNs, compared to the primary tumor.

4.1.6.3 Immune cell status in tumors and lymph node metastases

Immune cells are described to have an impact on virus replication.[141,142] Hence the amount of different immune cells in tumors and lymph node metastases was determined. Therefor the single-cell suspensions already described in chapter 4.1.6.2 were stained with different antibodies and analyzed by FACS. The used antibodies were α-CD11b and α-CD45 to stain monocytes, α-CD19 to stain B cells and α-CD49 to stain natural killer (NK) cells.

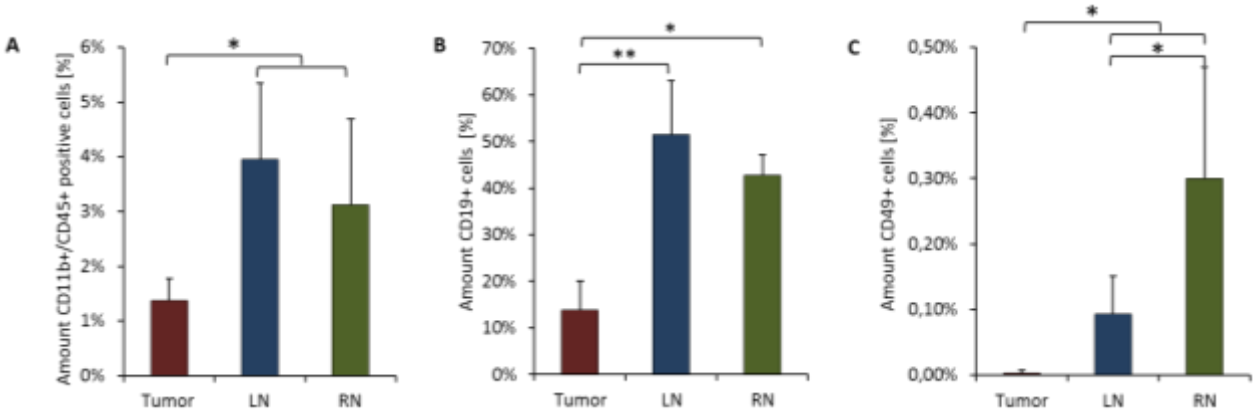

Figure 4-21: Quantification of immune cells in tumors, LNs and RNs by FACS analysis. Single-cell suspensions of tumors, LNs and RNs of 4 C33A tumor-bearing mice 42 dpti were analyzed for the amount of immune cells by FACS analysis. 10.000 cells per sample were measured. The used antibodies were α-CD11b and α-CD45 to stain monocytes [A], α-CD19 to stain B cells [B] and α-CD49 to stain NK cells [C]. (Two tailed, unpaired students t-test: * p>0.05; ** p>0.01; *** p>0.001)

FACS analysis revealed a much higher amount of immune cells in lymph nodes compared to primary tumor for all three tested immune cell populations (Figure 4-21). The total amount of

monocytes, which are CD11b and CD45 positive, in primary tumor was about 1.4% (± 0.4%) while it was significantly higher in LNs with almost 4% (± 1.4%) and in RNs with 3.2% (± 1.5%), as seen in Figure 4-21 [A]. However, no significant differences were detectable between both lymph node pairs. The same was true for the amount of CD19 positive B cells (Figure 4-21 [B]). While the amount was significantly higher in lymph nodes compared to primary tumors, no differences were observed between LNs and RNs. The highest amount was measurable in LNs with almost 52% (± 11%) $CD19^+$ cells, followed by RN with 43% (± 4%) and the lowest amount was found in tumors with 14% (± 6%). However, for $CD49^+$ NK cells it was different (Figure 4-21 [C]). The amount of these cells in primary tumor was 0.025%, meaning there were almost no NK cells in the primary tumor. Furthermore, the amount of $CD49^+$ cells in lymph nodes was very low as well. Nevertheless, with 0.1% (±0.06%) $CD49^+$ cells in LNs and 0.3% (± 0.17%) $CD49^+$ cells in RNs the amount in renal node was significantly higher compared to the amount in lumbar nodes.

Taken together, a significant higher amount of all three tested immune cell populations in lymph nodes compared to the primary tumor were detected.

4.1.6.4 Lymph and blood vessel density in tumors and lymph node metastases

The next step was to analyze whether differences occur in the vasculature regarding density and permeability of lymph and blood vessels between tumors and metastases, leading to a higher initial amount of viral particles within the different tumorous tissues. 10 µm cryo sections of tumors and lymph nodes 42 days after C33A-RFP implantation were prepared and slices were stained with an α-LYVE1 antibody or an α-CD31 antibody, to stain lymphatic vessels or blood vessels, respectively.

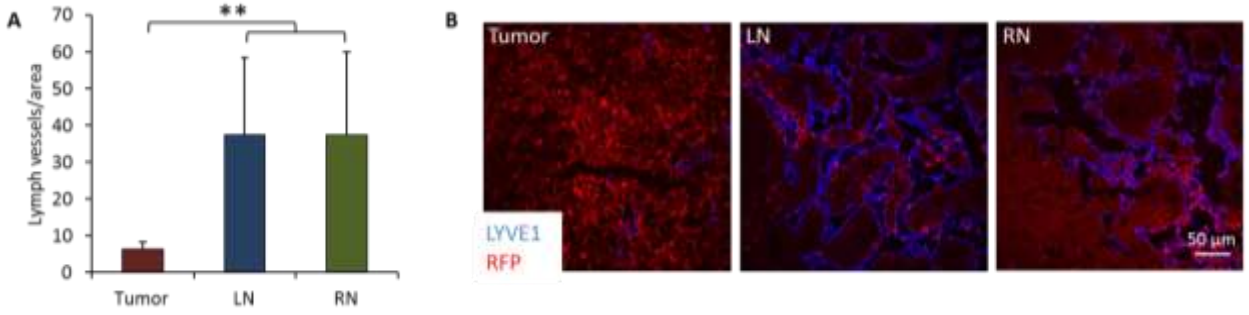

Figure 4-22: Lymph vessel density in primary tumors and lymph nodes 35 days after C33A-RFP tumor cell implantation. Cryo sections of tumors and lymph nodes were stained with an α-LYVE1 antibody. Five

images per sample (n=8) were analyzed by adding 8 equidistant horizontal lines using Photoshop 7.0. All lymph vessels crossing these lines per image were counted to obtain the vessel density per section. [A] Lymph vessel density per defined tumor/lymph node area. [B] Representative images of a tumor, LN and RN sections. Tumor cells are displayed by RFP signal (red), and lymph vessels by LYVE-1 staining (blue). (Two tailed, unpaired students t-test: * p>0.05; ** p>0.01; *** p>0.001)

Although no differences in lymph vessel density were found between the two lymph node pairs (LN and RN), the lymph vessel density in the tumor was significantly lower in primary tumors compared to the metastatic site (Figure 4-22 [A]). Whereas in tumors only 6 (± 2) lymph vessels were found per defined area, the amount in LNs and RNs was about 37 (± 19) lymph vessels per area. The higher lymph vessel density is clearly visible in the representative images (Figure 4-22 [B]). For LN and RN, the whole lymph node is traversed by big vessels, stained in blue. In contrast in tumor tissue, only few, small vessels were observed.

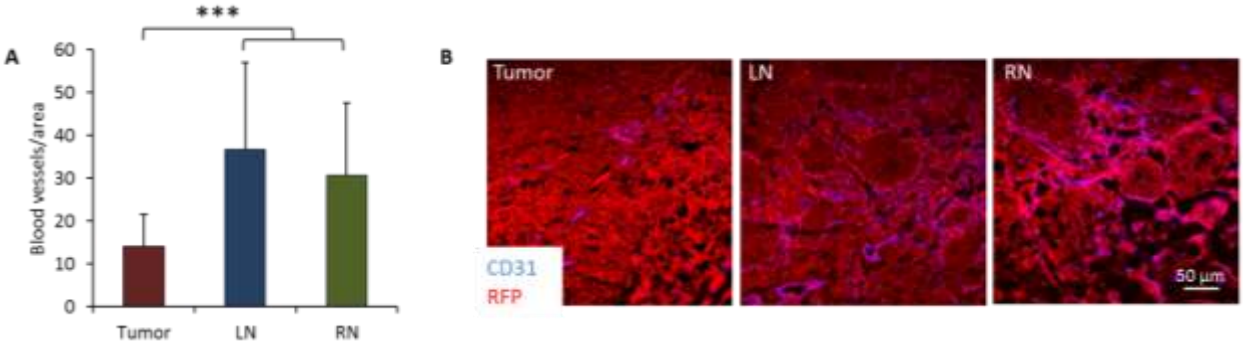

Figure 4-23: Blood vessel density in primary tumors and lymph nodes 35 days after C33A-RFP tumor cell implantation. Cryo sections of tumors and lymph nodes were stained with an α-CD31 antibody. Five images per sample (n=8) were analyzed by adding 8 equidistant horizontal lines per image using Photoshop 7.0. All blood vessels crossing these lines were counted to obtain the vessel density per section. [A] Blood vessel density per defined tumor/lymph node area. [B] Representative images of a tumor, a LN and a RN. Tumor cells are displayed by RFP signal (red), blood vessels by CD31 staining (blue). (Two tailed, unpaired students t-test: * p>0.05; ** p>0.01; *** p>0.001)

Blood vessel density showed the same pattern like lymph vessels, in both, tumors and lymph nodes (Figure 4-23). However, there were slightly more blood vessels per area in LNs than in RNs but these differences were not significant. Nevertheless, blood vessel density in both lymph node pairs was significantly higher compared to the primary tumor (Figure 4-23 [A]). While only 14 (±7) blood vessels were countable per tumor area, 37 (± 20) blood vessels per LN area and 31 (± 16) vessels per RN area, respectively, have been counted. The findings were also obviously visible in the representative images of tumors and lymph nodes (Figure 4-23 [B]). Many, clearly visible lymph vessels are located in both lymph nodes, while the primary tumor only displayed few, small lymphatic vessels.

Overall lymph node metastases have both, a higher lymph vessel and a higher blood vessel density compared to the primary tumor.

4.1.6.5 Vascular permeability in tumors and lymph node metastases

To find out whether these higher vessel densities indeed contributes to higher vascular permeability in lymph node metastases, the extravasation patterns of intravenously injected rat-IgGs of five mice were analyzed histologically. Therefor 70 µm agarose sections were stained with a Cy2-conjugated α-rat antibody to label extravagated IgG and IgG positive area per tissue was calculated.

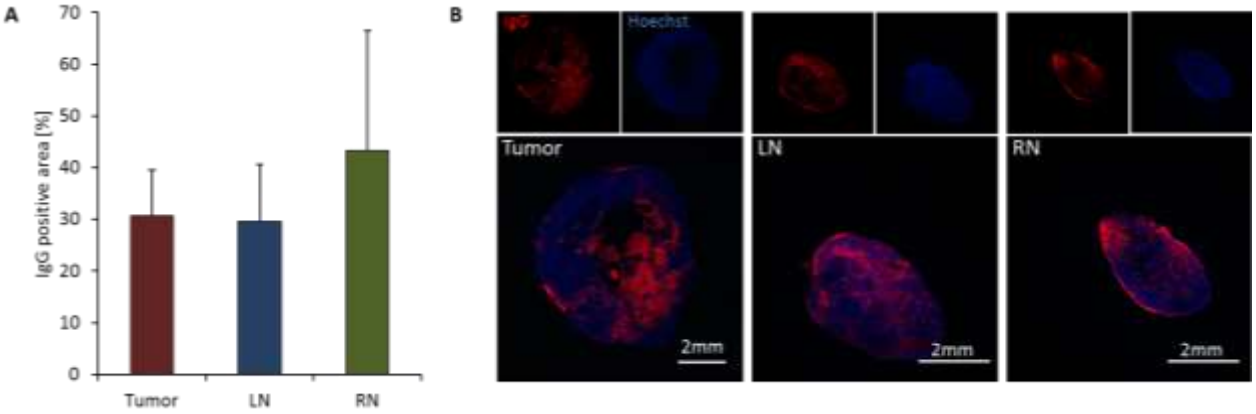

Figure 4-24: Extravasation of unspecific rat IgGs in C33A-RFP tumors, LNs and RNs 42 days post implantation. 5 Mice were injected with 10 mg/kg rat IgGs 4 h before tumors, LNs and RNs were excised and histology was performed. Extravagated IgG was visualized in 70 µm agarose sections with a Cy2-conjugated α-rat antibody. Areas positive for IgG were measured using ImageJ. [A] Percentage of IgG positive area in tumors, LNs and RNs. [B] Representative images of IgG distribution (red) and Hoechst staining (blue) in tumors, LNs and RNs (upper row) and the overlay of both images (lower row).

Surprisingly, the higher amount of blood vessels did not lead to a higher amount of extravagated IgG in lymph nodes (Figure 4-24). Actually the mean IgG area in both, tumors and LNs was about 30% (± 9%). The mean IgG-positive area in RNs was about 43% (± 23%) but no significant differences were detectable between RN and LN or RN and tumor.

Obviously the higher amount of lymph and especially blood vessels in lymph nodes compared to primary tumor did not lead to a higher vascular permeability in those tissues, demonstrated by the same levels of extravagated IgG in all tumorous tissues.

4.2 Characterization of metastases formation and virotherapy in the murine B16F10 melanoma model

In the first part it was possible to demonstrate the oncolytic effect of the recombinant vaccinia virus GLV-1h68 on the human cervical carcinoma cell C33A in an immunocompromised xenograft mouse model. However, in the past few years it became more and more obvious, that the immune system has a great impact on cancer and especially on cancer therapy.[143,144] Therefore the next step was to establish a new metastatic model in an immune competent mouse model. A promising candidate for this might be the metastatic melanoma cell line B16F10 implanted in the immune competent moues line C57BL/6.

4.2.1 Comparison of GLV-1h68 and LIVP 1.1.1 infection of B16F10 cells *in vitro*

To investigate whether the previously used GLV-1h68 or the less attenuated LIVP 1.1.1 are more suitable for efficient therapy of the murine melanoma cell line B16F10, first of all cell culture experiments were performed.

4.2.1.1 Replication of GLV-1h68 and LIVP 1.1.1 in B16F10 cells

A virus replication assay was performed to determine the ability of GLV-1h68 and LIVP 1.1.1 to efficiently infect and replicate in murine B16F10 melanoma cells in cell culture. For the analysis of the replication kinetics cells were infected with one of the virus strains at an MOI of 1 or 5. 8, 24, 48, and 72 hpi supernatants were collected, cells were harvested and viral titers were determined by standard viral plaque assay.

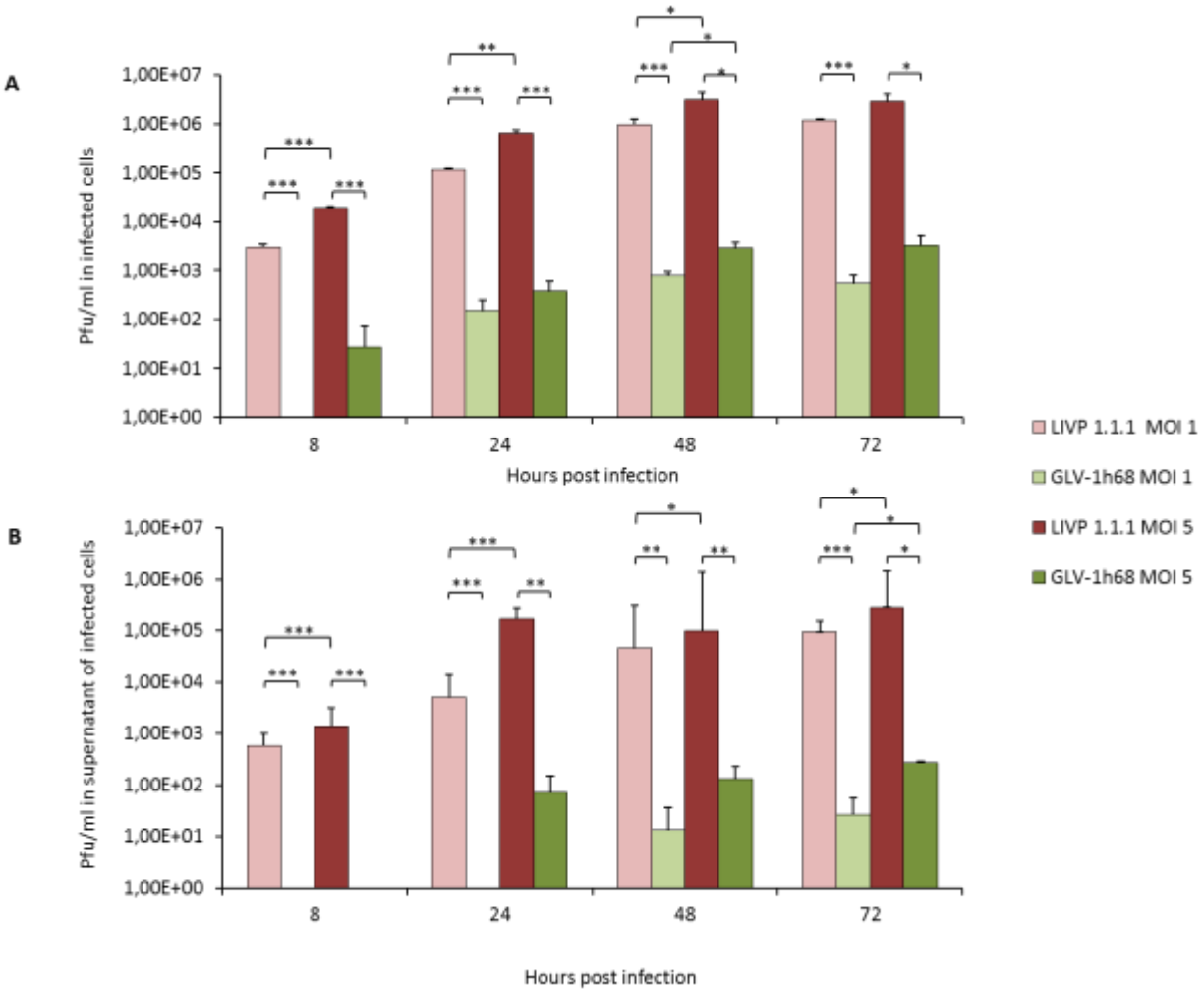

Figure 4-25: Analysis of viral titers in murine B16 F10 cells after infection with GLV-1h68 and LIVP 1.1.1 respectively, in cells [A] and supernatants [B]. Cells were seeded in 24-well plates and infected either with GLV-1h68 or LIVP 1.1.1 with MOI 1 or 5. 8, 24, 48, and 72 hpi cells and supernatants were collected and viral titers were determined in a standard plaque assay. Bar graphs represent mean values and standard deviations of three samples, analyzed in triplicates. (Two tailed, unpaired students t-test: * p>0.05; ** p>0.01; *** p>0.001)

Figure 4-25 [A] shows the viral titer in cell lysates of GLV-1h68 and LIVP 1.1.1 infected B16F10 cells at different time points after infection. It is clearly visible that the titers in LIVP 1.1.1-infected cells were significantly higher compared to the viral titer in GLV-1h68 infected cells, for both MOI 1 and MOI 5, at any time point. Additionally the viral titer in all infected cells, independent of the virus strain and MOI used, is increasing over time. The maximal viral titer was reached in LIVP 1.1.1-infected cells 72 hpi at MOI 1 with $1.17x10^6$ pfu/ml (± $6x10^4$ pfu/ml) and 48 hpi at MOI 5 with $3.07x10^6$ pfu/ml (± $1x10^6$ pfu/ml). In contrast, viral titers in GLV-1h68-infected cells were much lower, with the highest titer of $7.87x10^2$ pfu/ml (± $1.5x10^2$ pfu/ml) 48 hpi at MOI 1 and $3.23x10^3$ pfu/ml (± $2x10^3$ pfu/ml) 72 hpi at MOI 5. Additionally, after infection

with GLV-1h68 at MOI 1, virus was first detectable 24 hpi. In all other samples virus was already detectable 8 hours after infection. For LIVP 1.1.1 the titers in cells infected with MOI 5 were significantly higher compared to cells infected with MOI 1, except for 72 hpi. In GLV-1h68-infected cells no significant differences were detectable between both MOIs, except for 48 hpi.

Figure 4-25 [B] shows the viral titers in the supernatant of the infected cells. Like already described for the titer in cells, the titer in supernatants was significantly higher in those of cells infected with LIVP 1.1.1 compared to GLV-1h68-infected cells, at any time point and both, MOI 1 and MOI 5. In this case the highest titers were reached 72 hpi in all four cases, with $9.53x10^4$ pfu/ml (± $5x10^4$ pfu/ml) for LIVP 1.1.1 MOI 1, $2.91x10^5$ pfu/ml (± $6x10^4$ pfu/ml) for LIVP 1.1.1 MOI 5, $2.67x10^1$ pfu/ml (± $3x10^1$ pfu/ml) for GLV-1h68 MOI 1 and $2.73x10^2$ pfu/ml (± $1x10^1$ pfu/ml) for GLV-1h68 MOI 5. LIVP 1.1.1 was already detectable 8 hours after infection, irrespectively of the MOI. In contrast, GLV-1h68 was first detectable 24 hpi after infection with MOI 5 and 48 hpi after infection with MOI 1. Here, the viral titer of cells infected with LIVP 1.1.1 at MOI 5 were significantly higher compared to the titer in supernatant of cells infected with LIVP 1.1.1, MOI 1, at any time point. In contrast, the difference of viral titer in supernatant of cells infected with GLV-1h68 was not significant, except for 72 hpi.

In general the titers in LIVP 1.1.1-infected cells were up to 4 log10 levels higher compared to viral titers in GLV-1h68 infected cells, meaning LIVP 1.1.1 is replicating more efficiently in the murine cell line.

4.2.1.2 LIVP 1.1.1 lyses B16F10 cells more efficiently than GLV-1h68

To compare the ability of GLV-1h68 and LIVP 1.1.1 to infect and lyse murine B16F10 cells XTT assay was performed. Cells were infected with one of the virus strains at MOI 1 and MOI 5, respectively. 24, 48, 72 and 96 hpi, XTT assay was performed.

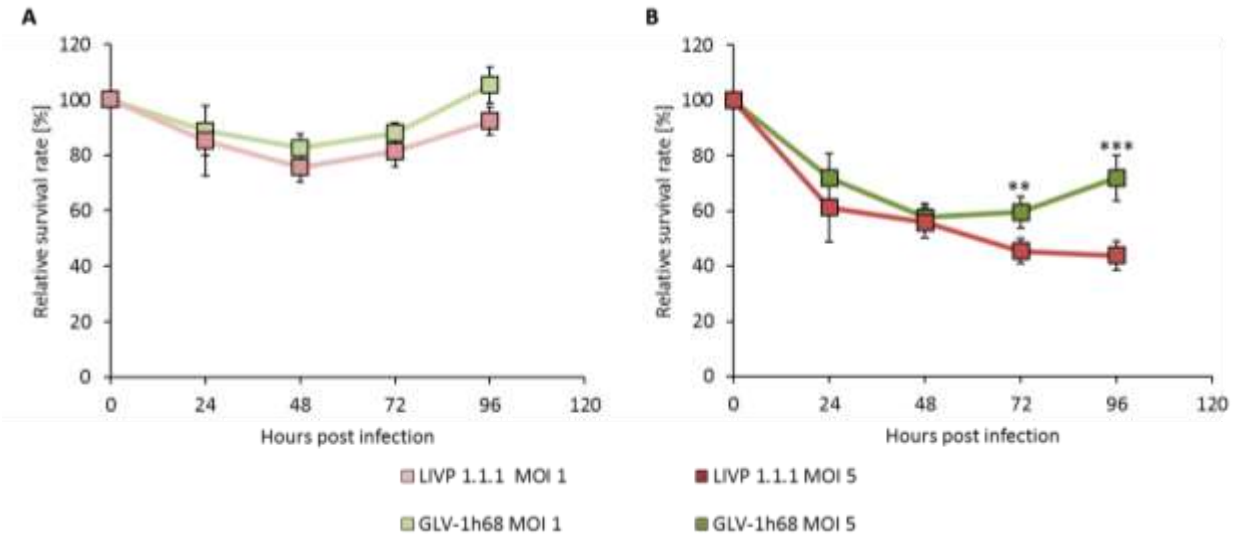

Figure 4-26: Viability of B16F10 cells after infection with GLV-1h68 or LIVP 1.1.1 with MOI 1 [A] and MOI 5 [B], respectively. Viability was monitored with a XTT assay over the course of 96 hours after infection. The experiment was performed three times in triplicates. At each time point non-infected cells served as a reference and were considered 100% viable (Two tailed, unpaired students t-test: * p>0.05; ** p>0.01; *** p>0.001).

Figure 4-26 [A] shows the cell viability after infection with GLV-1h68 or LIVP 1.1.1 with MOI 1. After infection with both viruses the cell viability decreased slightly until 48 hpi to 82% (± 5%) (GLV-1h68) and 75% (± 6%) (LIVP 1.1.1) viable cells respectively. Afterwards the amount of viable cells started to increase again, reaching up to 105% (± 5%) (GLV-1h68) and 91% (± 5%) (LIVP 1.1.1) at 96 hpi. Generally, marginally more of the cells infected with LIVP 1.1.1 were lysed compared to cells infected with GLV-1h68, but with no statistically significant differences at any time point.

After infection with a higher MOI, MOI 5, (Figure 4-26 [B]) cells were lysed more efficiently with both viruses. 48 hours after infection with GLV-1h68 cell viability reached a minimum with 57% (± 3%) living cells. Afterwards the amount started to increase again up to 71% (± 8%) viable cells 96 hpi. In contrast to that cell viability after infection with LIVP 1.1.1 steadily decreased to 43% (± 7%) 96 hpi. The difference between cell viability of cells infected with GLV-1h68 and those infected with LIVP 1.1.1 was significant 72 and 96 hpi.

Overall LIVP 1.1.1 displayed a stronger cytotoxic effect compared to GLV-1h68 in B16F10 cells. The cytotoxicity was MOI dependent.

4.2.2 *In vivo* experiments

In the first part it was possible to demonstrate that LIVP 1.1.1 is more efficiently replicating in and lysing of murine B16F10 tumor cells. The main object was to establish a new metastasizing tumor model in an immunocompetent mouse background. To investigate whether the immunocompetent mouse strain C57Bl/6 is as good as a FoxN1 nude mice as a model to analyze metastatic disease, both mouse strains were compared. Furthermore, different implantation methods, and different virus administration routes were compared.

4.2.2.1 Comparison of different implantation techniques: subcutaneous vs footpad

To analyze which tumor localization results in a higher metastatic burden two implantation sides were tested: subcutaneous (s.c.) implantation at the abdominal flank and implantation in the foodpad (f.p.) of female FoxN1 nude mice. For s.c. implantation $2x10^5$ B16F10 cells were implanted into the right abdominal flank. For f.p. implantation $2x10^5$ cells were injected into the footpad of the right hind leg. S.c. implanted mice were sacrificed when tumors reached a volume of about 2500-3000 mm^3 (between 17-21 dpti), f.p. implanted mice were sacrificed when tumor reached a volume of 100-120 mm^3 (between 17-22 dpti) (n=5). At this time point lymph nodes, like already described for the C33A model were analyzed for their metastatic burden. Based on the fact that LN and RN were first metastasized after the s.c. implantation of C33A at the right abdominal flank those were also of main interest after s.c. implantation of B16F10 cells. After f.p. implantation the PN is described as the first lymph node to get metastasized,[145] therefore this was the lymph node of main interest, here, but also other closely located nodes were screened. Lymph nodes of untreated mice at the same age served as control.

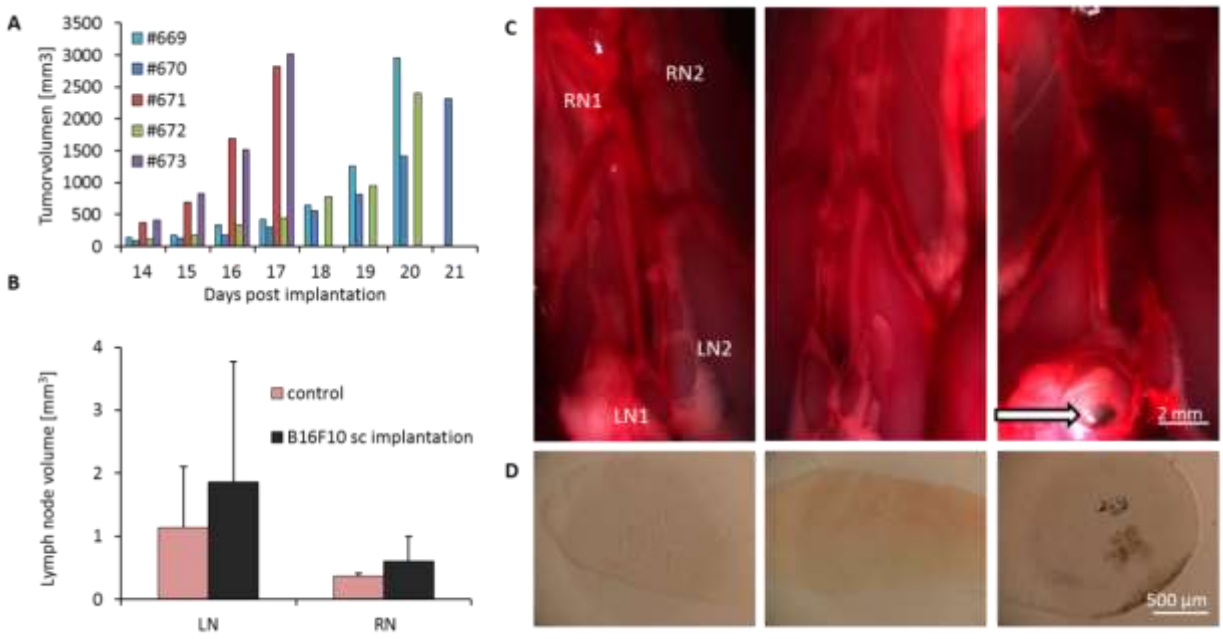

Figure 4-27: Subcutaneous implantation of 2x10^5 B16F10 tumor cells into the right abdominal flank of FoxN1 nude mice: [A] Tumor volume of all five mice (#669-673) was measured daily with a digital caliper in two dimensions. Bar graphs represent tumor volume of each single mouse. [B] Bar graphs represent mean volume and standard deviation of renal and lumbar lymph nodes of untreated control mice (nude) and of mice after implantation of B16F10 cells (black) (n=5) at the end point of the trial. Lymph node volume was measured in two dimensions. [C] Representative images of lumbar and renal lymph nodes of untreated mice (left) and of two different mice after implantation of B16F10 cells (middle and right). White arrow indicates blackish coloration of metastasized lymph node. [D] Agarose sections of LN1 of untreated mouse (left) and two different B16F10 tumor-bearing mice (middle and right).

Figure 4-27 [A] shows the tumor volume of all 5 subcutaneously implanted mice. It is clearly visible, that the tumor is growing very fast. After tumors started to grow the tumor volume doubled nearly every 24 hours. The first two mice had to be sacrificed at day 17 after implantation. At this time point tumor volume reached 3000 mm^3. For these two mice the volume doubling is clearly visible: from day 14 dpti the tumor volume was steadily doubling from 380 mm^3 (14 dpti) to 830 mm^3 (15 dpti) to 1580 mm^3 (16 dpit) finally reaching 3000 mm^3 (17 dpti). The other three mice were sacrificed at days 20 and 21, respectively, showing a similar tumor growth kinetic. In Figure 4-27 [B] the volume of LN and RN of untreated mice is compared to the lymph node volume of B16F10 tumor-bearing mice. Lymph node volume of tumor-bearing mice was only slightly increased compared to those of untreated mice. Volume of untreated mice was 1.1 mm^3 (±0.9 mm^3) for LN and 0.3 mm^3 (±0.04 mm^3) for RN. After implantation of B16F10 cells lymph node volume increased to an average of 1.9 mm^3 (±1.9 mm^3) for LN and 0.6 mm^3 (±0.4 mm^3) for RN, respectively. However there were no significant

differences in volume, neither for LN nor for RN. Only one out of five LNs showed a clear black coloration caused by metastatic B16F10 cells ([C] and [D]; right side). All other lymph nodes exhibited a brownish color seen in agarose sections. ([C] and [D]; middle). Furthermore it was clearly visible, that lymph node volume correlated with black coloration of lymph nodes, meaning the most black-colored lymph node was the biggest, whereas light brown-colored lymph nodes displayed no significant enlargement.

Obviously s.c. implantation of B16F10 in the abdominal flank is not an appropriate model to investigate metastatic behavior and oncolytic virus therapy because tumors a growing too fast and lymph nodes did not get metastasized. Therefore another implantation model was analyzed, the implantation in the footpad.

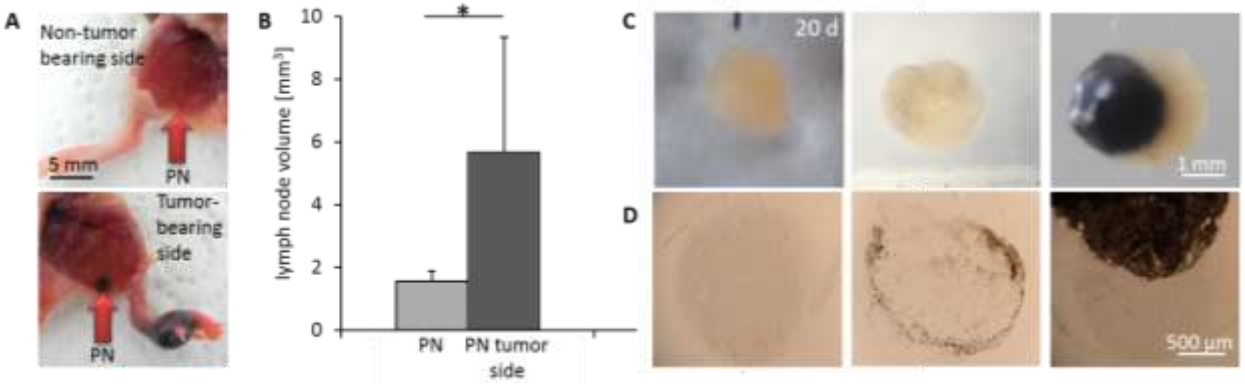

Figure 4-28: Footpad implantation of 2x10^5 B16F10 tumor cells into the left hind leg of FoxN1 nude mice. The popliteal lymph node at the tumor-bearing side and at the non-tumor-bearing side of five mice was analyzed. [A] Representative images of a mouse foot and PN of untreated control (upside) and a mouse foot with tumor and metastasized PN 20 dpti (downside). Arrows are indicating the PN. [B] Lymph node volume of the popliteal lymph node of untreated control mice (light grey) and volume of the PN of tumor-bearing mice (dark grey) 20 dpti. [C] PN of control mouse (left) and of metastasized PN of two different mice (middle and right). [D] Agarose sections of PN of an untreated mouse (left) and two different tumor-bearing mice (middle and right). (Two tailed, unpaired students t-test: * p>0.05; ** p>0.01; *** p>0.001)

Figure 4-28 [A] revealed the localization of tumor and PN after implantation of B16F10 cells into the footpad. The arrow in the upper image is pointing at a non-metastasized popliteal lymph node. This PN is not visible with bare eyes. In contrast, after tumor implantation both is clearly visible, the primary tumor in the footpad and the metastasized PN (arrow in the lower picture). In Figure 4-28 [B] the volume of PNs of untreated mice is compared to those of tumor-bearing mice. The average volume of former is 1.5 mm^3 (± 0.3 mm^3) whereas the volume of later is 5.7 mm^3 (± 3.3 mm^3). Overall the volume of PN after f.p. implantation of B16F10 cells is significantly

higher compared to those of untreated mice. All PN at tumor side had black spots which were clearly seen in both, whole lymph nodes (Figure 4-28 [C]) and agarose sections of lymph nodes (Figure 4-28 [D]) in contrast to untreated mice. Furthermore two PNs had completely black dyed areas like seen in the images on the right in Figure 4-28 [C]+[D]. In other lymph nodes, like LN, RN, IN or SN no melanoma cells were detected, neither in the whole lymph node, nor in agarose sections.

Overall this experiment revealed both, that footpad implantation of B16F10 cells lead to a higher metastatic burden compared to subcutaneous implantation represented by a significant higher enlargement of lymph nodes compared to untreated controls and visibly more black tumor cells within the affected lymph node. Therefore, in the following experiments tumors were implanted into the footpad.

4.2.2.2 Comparison of footpad implantation in FoxN1 nude and C57BL/6 mice

Hence, the next step was to determine whether there are differences in overall survival and metastatic burden between immunocompromised nude mice and immune competent C57BL/6 mice. Therefore $2x10^5$ B16F10 cells were implanted in the left hind footpad of 5 mice of every group. Mice were monitored and weighted every day to determine the health status of the mice. When tumors reached a volume of about 120 mm^3 mice had to be sacrificed because of the tumor burden. The volume of popliteal lymph nodes was determined and compared to control lymph nodes *post mortem*.

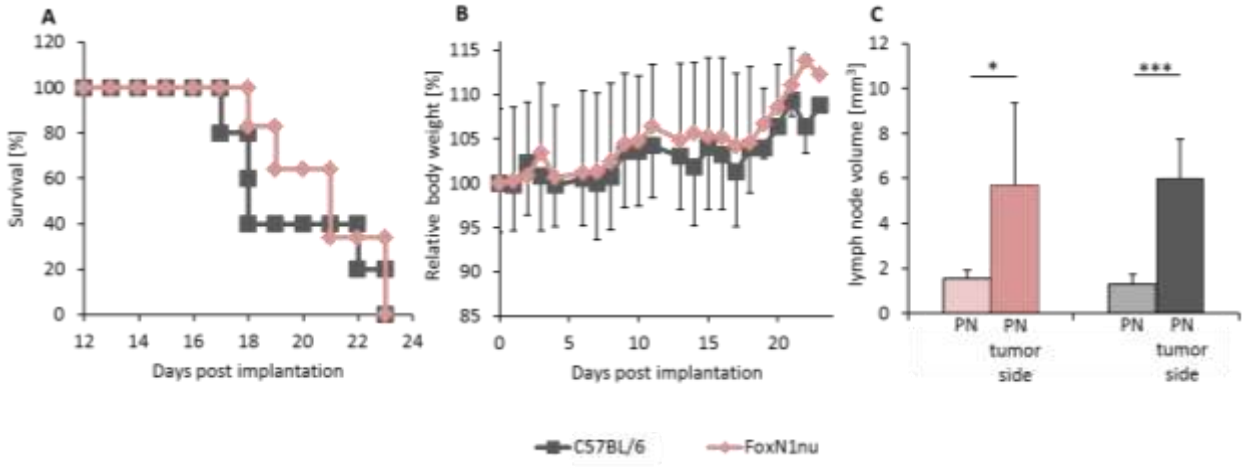

Figure 4-29: Comparison of footpad implantation of B16F10 cells in FoxN1^{nu} and C57BL/6 mice. 5 mice per group were analyzed. [A] Kapplan-Meier survival curve after tumor cell implantation. [B] Body weight was measured every day to control the health status of the mice. Changes in body weight were set

relative to body weight at the day of implantation (0 dpti). [C] Popliteal lymph node volume was measured in two dimensions at the tumor-bearing and at the non-tumor-bearing site *post mortem*. (Two tailed, unpaired students t-test: * p>0.05; ** p>0.01; *** p>0.001)

Figure 4-29 [A] shows a Kaplan-Meier survival curve, indicating how long mice survived after tumor cell implantation. The overall survival and therefore most likely the time course of tumor growth, respectively, metastatic spread was the same in both groups, with last mice being sacrificed 23 days after implantation in both groups. The average survival differed in less than one day with 19.8 days (± 2.3 days) survival for C57Bl/6 and 20.4 (±1.7 days) days for nude mice. Furthermore relative body weight was determined as an indication of the health status of the mice. The body weight at the day of implantation was set as 100%. Generally in both groups the relative body weight was increasing over time the same manner, indicating that implantation of B16F10 into the footpad had no negative effects on mice health status. Additionally, lymph node volume was measured after mice have been sacrificed. In both groups, the lymph node volume at the tumor-bearing site was significantly higher compared to lymph nodes of untreated mice. The volume of those PNs was 1.5 mm^3 (± 0.3 mm^3) for nude and 1.3 mm^3 (± 0.4 mm^3) for C57Bl/6 mice, respectively. After tumor implantation, lymph node volume increased up to 5.7 mm^3 (± 3.3 mm^3) (nude) and 5.9 mm^3 (± 1.7 mm^3) (C57BL/6), respectively.

Taken together, there were no differences in survival, health status or metastatic burden between nude mice and C57BL/6 mice detectable. Therefore, the immune competent C57BL/6 mouse model seems to be useful as a tumor model to investigate a suitable therapy for metastatic cancer with VACV, but also to analyze the influence of the immune system on virus therapy.

4.2.2.3 Characterization of tumor and lymph node metastases formation after footpad implantation of B16F10 cells

To analyze the formation of lymph node metastases over time 32 mice were implanted with $2x10^5$ B16F10 cells into the footpad of the right hind leg. Every 5 days 8 mice were sacrificed and tumors and popliteal lymph nodes were analyzed.

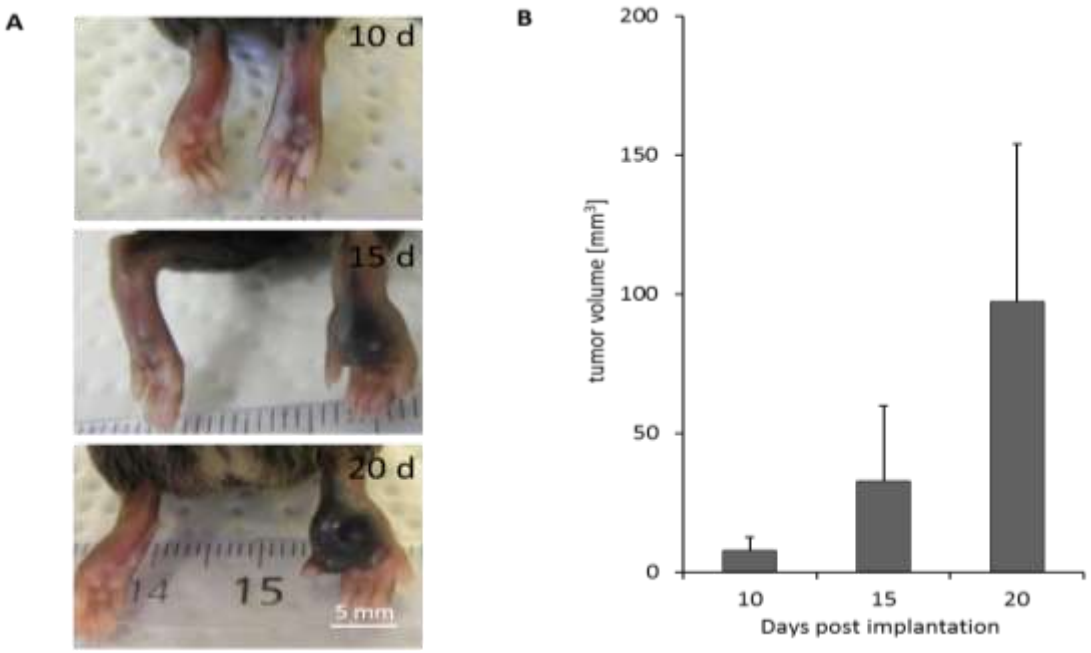

Figure 4-30: Tumor growth over time after implantation of B16F10 cells into the food pad of C57BL7/6 mice: Tumor volume was measurable from day 10 on. Therefore volume of tumors was measured at 10, 15 and 20 days after tumor implantation. [A] Representative images of mouse feet without (left foot) and with tumor (right foot) 10,15 and 20 days post f.p. implantation. [B] Bar graphs represent mean tumor volume of eight mice per time point at day 10 to day 20 after implantation. Tumor volume was measured with a digital caliper in two dimensions.

First tumors were visible 7-8 days after f.p. implantation. From day 10 on tumor volume was measurable. Figure 4-30 displays the steady tumor growth over time. In Figure 4-30 [A] both, the tumor-bearing foot as well as the non-tumor-bearing foot is shown. The expansion of the tumor over the whole footpad after 20 days can be clearly seen. Overall the average tumor volume was increasing from 8 mm3 (± 5 mm3) at 10 dpti to 98 mm3 (± 56 mm3) at the end of the experiment (Figure 4-30 [B])

Accordingly to the increase of tumor volume the development of PN metastases was monitored over time, as well.

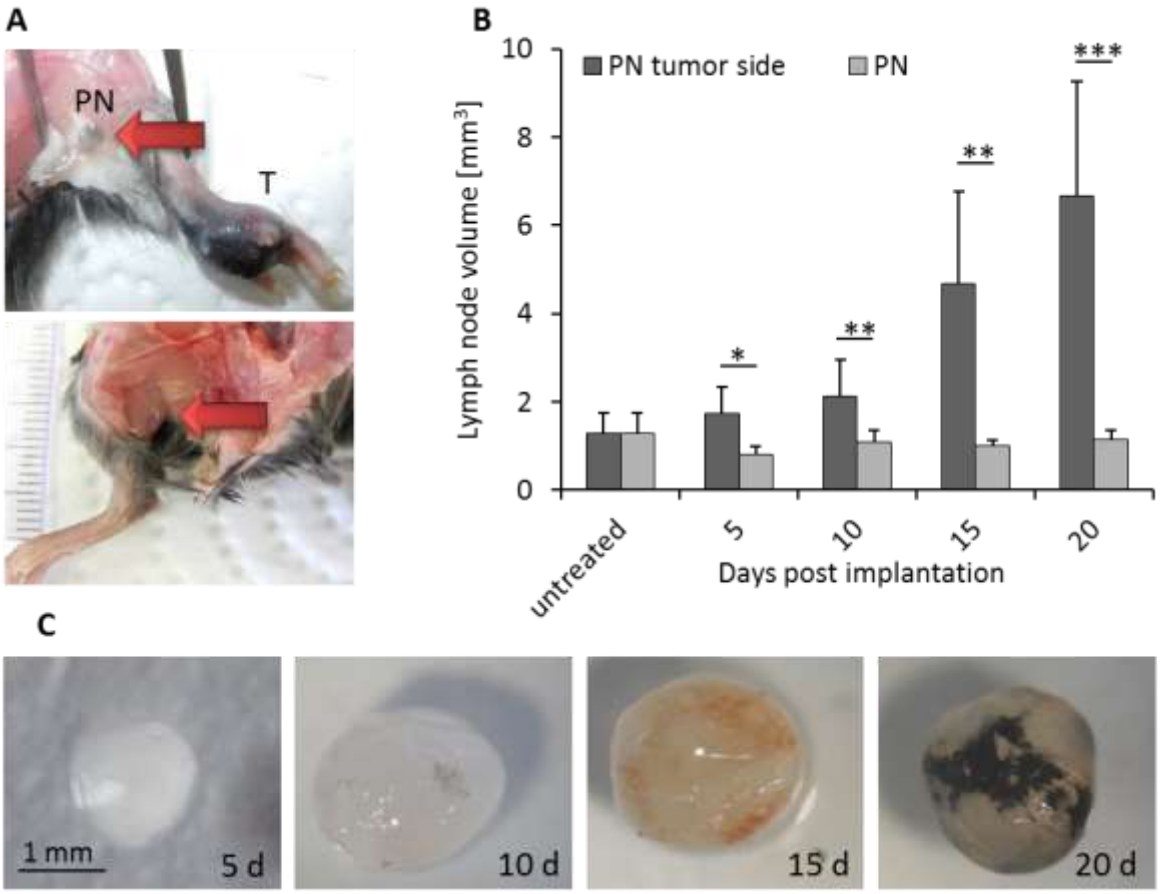

Figure 4-31: Enlargement of popliteal lymph nodes over time after f.p. implantation of B16F10 cells in C57BL/6 mice: [A] Representative images of the localization of tumor (T) and metastasized PN (arrow, upper image) and non-metastasized PN (arrow, lower image) 20 dpti. [B] Bar graphs represent mean volume of PN at the tumor-bearing side and the non-tumor-bearing site (n=8). Volume was measured in two dimensions [C] Representative images of PN from the tumor-bearing site at different time points after implantation.. (Two tailed, unpaired students t-test: * p>0.05; ** p>0.01; *** p>0.001)

In Figure 4-31 [A] the localization of tumors and PN is displayed. Metastasized popliteal lymph nodes are clearly visible by their blackish coloration within the fat tissue (arrow, upper image) due to the invasion of melanoma cells, while non-metastasized PN at the non-tumor-bearing site were not detectable visually (arrow, lower image). To analyze the increasing lymph node volume after tumor implantation, PNs on the tumor site were compared to PNs at the non-tumor site (Figure 4-31 [B]). There were no changes in PN volume at the non-tumorous site over time (light gray bars). At every time point the volume was about 1 mm^3 (± 0.2 mm^3). In contrast, already at day five after implantation the PN volume at the tumor side was significantly higher and increased steadily over time up to 6.7 mm^3 (± 2.6 mm^3) 20 dpti. Additionally, a change in color of the lymph nodes was observed, starting 10 days after implantation with small black

spots on the lymph node (Figure 4-31 [C]). Subsequently, at later time points either a brownish coloration was observed (like seen for the PN 15 dpti) or the PN exhibited a dark blackish dyeing (PN 20 dpti).

4.2.2.4 Comparison of different virus administration routes: intravenous vs. intratumoral

After intravenous virus administration vaccinia virus is quickly cleared from the blood by the immune system. [146,147] To find the most efficient way to deliver the virus to the primary tumor and lymph node metastases two different administration routes were compared: intravenous (i.v.) administration and intratumoral (i.t.) administration. For this $2x10^7$ pfu LIVP 1.1.1 were injected either intravenously in the tail vein or intratumoraly in B16F10-tumor-bearing C57BL/6 mice 18 days after footpad implantation. 48 hours after virus administration mice were sacrificed and virus titer in tumors and PNs was determined by standard plaque assay.

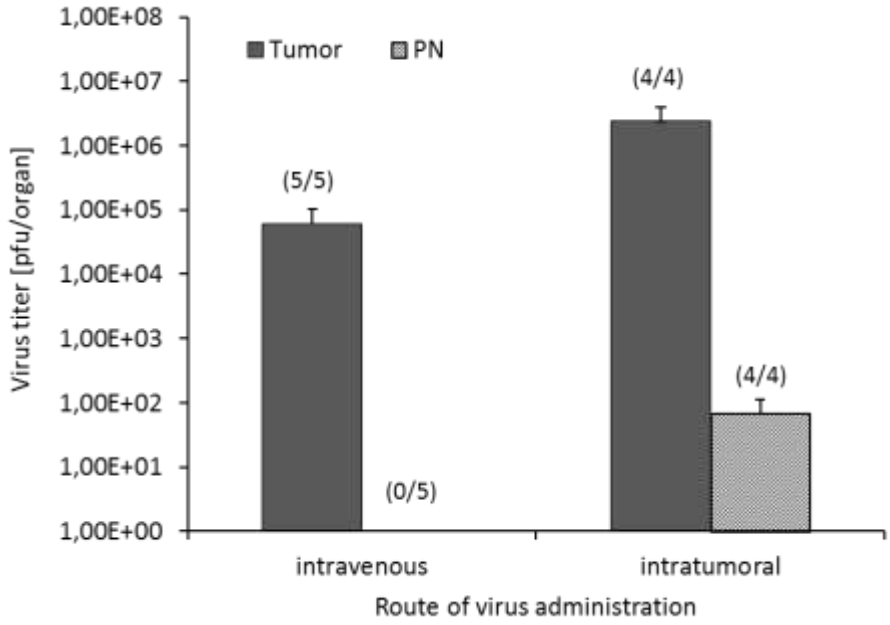

Figure 4-32: Virus titer in tumors and lymph nodes of B16F10 tumor-bearing C57BL/6 mice after intravenous and intratumoral virus administration: Virus was injected into tumor-bearing mice 18 days after tumor implantation. 48 hours after virus injection virus titer in tumors and metastases was determined by standard plaque assay (n=5 for i.v. injection; n=4 for i.t. injection)

Figure 4-32 shows the virus titer in tumors and lymph nodes after intravenous and intratumoral injection of virus respectively. In all 5 (i.v.) respectively 4 (i.t.) tumors virus was detectable. The average titer in tumors after i.v. injection was $6x10^4$ pfu/organ (± $4.2x10^4$ pfu/organ) and in

tumors after i.t. injection was $2.4x10^6$ pfu/organ (± $1.6x10^4$ pfu/organ). Furthermore, virus was verified after it administration in all 4 popliteal lymph node metastases. The average virus titer amounted to $7.1x10^1$ pfu/organ (± $4.2x10^1$ pfu/organ) per PN. In contrast no virus was detectable in any of the 5 PN metastases after intravenous administration.

Generally, the administration of virus directly into the tumor leads to higher titers in both, primary tumors and lymph nodes compared to intravenous injection.

5 Discussion

According to the WHO, cancer is one of the leading causes of death worldwide. Approximately 14 million new cases occur every year with 8.2 million of them dying.[1] However, most of those people affected by cancer do not die due to the effects of the primary tumor, but to the direct and indirect effects of metastases.[47,48] Therefore, the patient's prognosis is strongly connected to the stage of disease. Hence, it is very important to find a successful therapy for both, the primary tumor and distant metastases. So far, the treatment of choice is more or less the same like for the primary tumor: mainly radiation and chemotherapy. Unfortunately, there are often enormous molecular differences between the solid tumor and metastases, making the tumor treatment unsuccessfully for metastases.[50] Based on the fact that research and development was focused on primary tumors for a long time, less effort was put on developing new therapies for metastases.[148] Thus, it is indispensable to find new treatment strategies to fight not only the primary tumor but also metastases. Therefore, the aim of this work was to analyze two different metastatic tumor cell lines as promising models to finally investigate oncolytic virus therapy with vaccinia virus as a new tool to fight metastases.

5.1 Characterization of metastases formation and virotherapy in the human C33A cervical cancer model

Cervical cancer is one of the leading cancers in women worldwide. If the cervical cancer is diagnosed and treated at an early time point survival rate is with 90-95% very high, but unfortunately, the survival rate can drop rapidly beyond 5% when metastases occur. Therefore, it is important to find successful treatment options for cervical cancer and metastases. During a screening study of cervical cancer cell lines, where different cell lines were tested for the therapeutic responsivity for the oncolytic vaccinia virus, the C33A cell line became a promising model to investigate metastatic behavior of cervical carcinomas.

5.1.1 The human cervical cancer cell line C33A as a new metastatic model

The HPV-negative human cervical cancer cell line C33A is a commonly used tumor cell model in cell culture and mouse experiments, but it has not been described as a metastatic cell line so far.[149–151] Surprisingly, during the course of the study, enlarged lymph nodes were found 35 days

after C33A cells were implanted subcutaneously into the abdominal flank of nude mice. These enlarged lumbar and renal lymph nodes were visible with bare eyes. The volume expansion might have had different causes, like the invasion of immune cells as a response to tumor growth or even the invasion of tumor cells. The hypothesis of enlargement due to infiltrating tumor cells was encouraged by the fact that also for other tumor models these two lymph node pairs were described to get metastasized after the subcutaneous implantation of tumor cells.[92,152] To confirm this hypothesis for the C33A model, RNA of enlarged lumbar and renal lymph nodes was isolated, cDNA synthesized and the presence of tumor cells with human origin was proven with primers specific for human β-actin. By this, it was possible to detect human mRNA in 100% of all lumbar and 50% of all renal lymph nodes. So, obviously the enlargement of RN and LN was effected by the invasion of human tumor cells from the primary tumor and thereby the metastatic spread of C33A in an animal model was demonstrated for the very first time.

The next aim was to characterize the metastatic ability of C33A cells in detail. To facilitate this intention, the gene encoding for the red fluorescence protein (RFP) was stably inserted into the genome of C33A cells by lentiviral transduction.[139] Afterwards, it was possible to visualize the RFP-labeled tumor cells by fluorescence microscopy and thereby detecting migrating cancer cells and metastases in tumor-bearing mice more easily.

5.1.2 Insertion of RFP in C33A cells has no effects on infection, replication and cell lysis by GLV-1h68

The main object of this project was to investigate whether the oncolytic vaccinia virus GLV-1h68 is suitable for the therapy of C33A tumors and metastases in a mouse xenograft model. Since the insertion of the RFP gene is a stable insertion into the cell genome and it has been reported, that lentiviral transduction can cause epigenetic changes in cells and alter their properties.[153] Thus, the next step was to see whether the insertion of the gene encoding for RFP had any influence on the susceptibility of the cells to viral infection, replication and lysis by the virus. Therefore, a replication assay to analyze viral infection and replication and XTT assay to analyze virus-mediated cell lysis were performed.

The replication capability of GLV-1h68 in C33A-RFP cells was analyzed by a standard plaque assay and compared to that, obtained in studies with C33A cells. Viral titer in lysates of infected cells and supernatants were determined after virus infection at MOI 1 or MOI 0.1.

The experiments revealed that there were no differences between the infection efficacy of GLV-1h68 in C33A and C33A-RFP cells, for MOI 1 and MOI 0.1. That indicates, the viral titer in C33A and C33A-RFP cells after virus infection did not differ significantly. These findings demonstrate that the insertion of the RFP gene into the genome of C33A had no negative effects on the susceptibility of the cells to virus infection, replication and assembly of progeny virus. GLV-1h68 replicated as efficient in C33A-RFP cells as in the parental C33A cell line.

Moreover, the XTT assay revealed that the ability of GLV-1h68 to lyse cancer cells was similar in C33A and C33A-RFP cells, for both MOI 1 and MOI 0.1. This indicates that the insertion of the RFP gene did also not lead to a reduced susceptibility of the cells to GLV-1h68-mediated cell lysis.

Generally, the experiments demonstrated that the insertion of the gene encoding for RFP into the genome of C33A cells did not alter the behavior of the cells towards infection, replication and cell lysis by GLV-1h68. Therefore, the newly generated cell line C33A-RFP is a valuable tool for evaluating the effects of the oncolytic vaccinia virus on metastases in a xenograft mouse model.

5.1.3 C33A-RFP cells form tumors and migrate to lymph nodes after subcutaneous implantation

Generation of xenograft tumors by subcutaneous implantation of tumor cells in mice is a common model to study tumor development or treatment modalities. Also C33A(-RFP) forms solid tumors after the implantation in the abdominal flank of nude mice. But in contrast to many other cell lines, it was observed, that after implantation of C33A-RFP cells lymph nodes were enlarged. Moreover, it was shown, by RT-PCR that the enlargement was due to the invasion of tumor cells. Additionally, it was possible to monitor the metastatic spread of tumor cells and development of these lymph node metastases by inserting the cDNA encoding for RFP into the genome of C33A cells. Most obvious was the invasion of tumor cells in lumbar and renal lymph nodes. A metastatic invasion into these lymph nodes was already described in detail for other

tumor cell line, like the human prostate cancer cell line PC-3.[92] With aid of the RFP signal of tumor cells and fluorescence microscopy it was possible to follow the migration of C33A-RFP cells after generation of subcutaneous tumors. Generally, an increase in volume of all four lymph nodes (LN1, LN2, RN1 and RN2) from week to week, in accordance to tumor volume expansion was observed. Moreover, the amount of RFP positive lymph nodes was constantly increasing in parallel. Analyzing the lymph node volumes, it was remarkable that the volume of LN1 was increasing first and strongest. LN1 was also the first lymph node of these four, revealing RFP signal. Obviously, LN1 is the first target of metastasizing tumor cells. This is due to the fact, that carcinoma cells commonly metastasize to the regional lymph nodes, which is called the draining or sentinel lymph node.[154,155] In case, the sentinel lymph node is not affected, other lymph nodes are also likely to be free of metastases.[156] Surprisingly, the order in which the lymph nodes were getting enlarged and RFP-positive after LN1 was RN1, followed by LN2 and finally RN2. Although LN2 is closer located to LN1 and therefore is likely to be the next lymph node to get metastasized. This was in fact the same order in which lymph nodes got metastasized in the PC-3 model.[138]

The order, in which these lymph nodes get metastasized after the generation of subcutaneous C33A-RFP tumors, was always the same and in every mouse these four lymph nodes were affected with regularity. Additionally, other lymph nodes, located at distant sites were also affected by metastasis, however this happened infrequently. Those lymph nodes were the inguinal node, the axillary node, the brachial node and the sacral node, but only at the tumor-bearing site. These lymph nodes were found to be metastasized only in a few mice and moreover, metastases in these lymph nodes occur only at later time points after implantation, compared to metastases in LNs and RNs. They were first detectable from 28 dpti on. Commonly, at later stages of the disease and with progression of tumor growth more and more disseminating tumor cells occur resulting in distant lymph node metastases. Therefore, the C33A represents a suitable model to investigate the progression of metastases, because it reflects the outcome of a metastatic disease in human patients.

5.1.4 C33A cells use the lymphatic as well as the haematogenous route of migration

So far, it was possible to prove that the enlargement of lymph nodes was due to the invasion of metastatic cancer cells. Moreover, migrating tumor cells were directly detected in lymph vessels

connecting lumbar and renal lymph nodes demonstrating the lymphatics as route of metastasis. This was shown by staining cross sections of the area between LN and RN with an α-LYVE1 antibody labeling lymphatic endothelial cells. By this, the red tumor cells were detected within the main LN-RN connecting lymph vessel. This process of tumor cells dissociating from metastases and entering the circulation and forming new metastases is known as metastasis from metastases and is very well described.[157] Additionally, this lymphatic spread as the pattern of metastasis is a common feature for almost all carcinomas.[22,158]

In addition, migrating tumor cells were detected by fluorescence microscopy in the blood vessel located next to the LN-RN connecting lymph vessel. By this, the haematogenous way of metastatic spreading was demonstrated. It is known that there is a strong connection between lymphatic and haematogenous metastasis, and in carcinomas haematogenous metastasis occur after lymphatic ones.[159,160] Furthermore, it was reported that in a PC-3 xenograft model haematogenous lung metastases only occur when lumbar and renal lymph nodes were metastasized independently of tumor size.[160] Also in the C33A-RFP model haematogenous metastases in the lung were detectable at later time points (from 28 dpti on). Microscopic studies revealed that the RFP signal in lungs came from aggregates formed by a bunch of tumor cells, so-called micrometastases

Additionally to the metastatic areas in the lungs, also a strong RFP signal was detectable in kidneys. But in contrast to RFP signal in lungs, the signal in kidneys was already detectable 14 dpti and the intensity was increasing over time. It was also remarkable that the distribution of RFP was different in both organs: while in lungs the signal was located in spot liked patterns, the signal in kidneys was equally distributed over the whole organ. Histological studies revealed that the RFP signal in kidneys did not originate from metastases. While the RFP expressing tumor cells showed a strictly organized structure in tumors and lymph node metastases, this was not observed in kidneys. Additionally, single-cell suspensions of kidneys of C33A-RFP tumor-bearing mice only contained small amounts of viable tumor cell, indicating that the RFP signal must rather be caused by cell-independent RFP fragments.[139] Besides, the RFP was mainly located in cell-independent fragments mainly in the nephrons, leading to the assumption that the signal is caused by the deposition of RFP in the renal cortex, after blood filtering in the nephrons. These RFP fragments might be discharged by dying tumor cells and afterwards released into the blood

stream. When the blood is then filtered in the nephrons RFP fragments might possibly stuck there. The reason why the tumor cells are dying might be due to hypoxia. The enormous growth of primary tumors can often lead to the development of hypoxic regions. Hypoxia can than act as a stressor which induces tumor cell death.[161]

5.1.5 Successful therapy of primary C33A-RFP tumors and metastases with the oncolytic vaccinia virus GLV-1h68

The vaccinia virus GLV-1h68 is a promising tool in the field of oncolytic virus therapy. So far, the successful regression of tumors in a mouse model was described for a variety of different types of tumors.[84,91–97] However, the effects of oncolytic vaccinia viruses on metastases are only poorly described. By now, the colonization of metastases was only demonstrated for the recombinant rVV-*RUC-GFP* in metastases of MCF-7 tumor-bearing mice,[162] and for GLV-1h68 in regional lymph nodes of B16F10 tumor-bearing mice.[96] Moreover, the successful therapy of metastases with GLV-1h68 was only proven for the prostate cancer cell line PC-3.[92] Therefore, it is indispensable to find new metastatic models for therapy with GLV-1h68.

After it was possible to establish C33A-RFP as a valid model to study metastatic process, the next step was to investigate whether administration of GLV-1h68 leads to the regression not only of the primary tumor but also of metastatic burden.

Virus was administered systemically in one single dose intravenously into the tail vein of tumor-bearing mice 21 dpti. At this time point lymph node metastases in lumbar and renal lymph nodes were already established. Indeed, the administration of GLV-1h68 in C33A-RFP tumor-bearing mice led to the drastic reduction of primary tumor size, indicating that the C33A cervical cancer model is responding well to oncolytic vaccinia virus treatment. There were concerns, that a therapy of a HPV-negative cell line might not have any clinical relevance. Hence, it was demonstrated in a cervical cancer screening study (with HPV-positive and HPV-negative cancer cell lines) that this effect is not dependent on the presence of HPV-DNA in the genome.[139] It was found, that neither the presence nor the copy number of HPV-DNA has any impact on how the cell line responds to treatment with vaccinia virus.

Moreover, it was observed that GLV-1h68 is able to reduce the metastatic burden in C33A-RFP tumor-bearing mice. This was demonstrated by the significant reduction of lymph node volume

and RFP signal of lumbar and renal lymph nodes over time following virus treatment. Already 3 weeks after virus treatment all four lymph nodes (LN1, LN2, RN1 and RN2) were significantly smaller compared to these lymph nodes in untreated mice at the same time point. Additionally, a reduction of RFP fluorescence intensity in kidneys was observed. 21 dpi no RFP signal was detectable in kidneys any more. However, at early time points the RFP signal was drastically increasing. These findings support the hypothesis that the RFP signal is due to the deposition of RFP fragments described above. At early time points after virus administration, the majority of cancer cells in the primary tumor and the metastases got lysed, releasing more RFP into the blood stream. At later time points, when metastatic burden was already drastically reduced, the amount of tumor cells being lysed was diminished and therefore, no more RFP was released into the blood stream. Hence, the reduction of RFP signal in kidneys might not be caused by direct virus colonization with following viral replication and tumor cell lysis in the kidney.

Taken together, it was possible to demonstrate, that GLV-1h68 is not only able to successfully lead to the regression of primary tumors but also can reduce the metastatic burden in C33A-RFP tumor-bearing mice. Moreover, it was shown that GLV-1h68 can also prevent formation of lymph node and lung metastases, when given at early time points after tumor cell implantation (11 dpti).[139] So far the successful reduction of primary tumor mass in the C33A model was described for Sindbis virus and adenovirus.[163,164] However, none of these publications reported metastases. In contrast, in this thesis, it was possible to demonstrate for the very first time that GLV-1h68 is not only a successful tool to fight primary tumors, moreover it is a promising candidate to fight lymphatic as well as haematogenous metastases in cervical cancer models.

5.1.6 Preferential colonization of primary tumors compared to lymph node metastases by GLV-1h68

Intravenous injection of GLV-1h68 in PC-3-RFP tumor-bearing mice led to a certain infection pattern: the virus preferentially colonized renal lymph nodes, followed by lumbar nodes and the primary tumor showed the lowest colonization rate.[137] Moreover, this order of colonization was also observed with different administration routes, like intraperitoneal or even intratumoral injection.[138] Hence, it was interesting to find out whether this is a general colonization patter for GLV-1h68 in metastatic tumor models. Therefore, C33A-RFP tumor-bearing mice were injected intravenously with GLV-1h68 and lymph nodes and primary tumor were analyzed for the

presence of virus at early time points after injection by quantification of the GFP signal on the surface of primary tumors or metastases caused by the virus. Surface imaging revealed in both, primary tumor and LN metastases the first GFP signal at 3 days after virus injection. In contrast, histological analysis of cryo sections and plaque assay revealed virus in tumors already 1 day after virus injection, while in LNs virus was first detectable 3 dpi and in RNs 7 dpi. This is not surprising, since optical imaging is not a deep tissue imaging method and signals can only be detected on the surface. The histological analysis of sections and plaque assays are more sensitive methods to detect virus in any part of the tumor. Additionally, viral titers in tumor were always higher compared to those in lymph nodes. The virus colonization pattern in C33A-RFP tumor-bearing mice was exactly the other way round of what was described for the PC-3-RFP model. In the C33A model, the virus clearly preferred the primary tumor as the first target for colonization, while lymph node metastases were colonized later on. Additionally, after the primary tumor, first the draining lymph node metastases were colonized followed by distant ones. In contrast, in the PC-3-RFP model first RNs got colonized, followed by LNs and at the end, virus was detected in the primary tumor. Although, PC-3 and C33A have different colonization patterns they are both suitable to study virus therapy on metastases. Nevertheless, there seem to be different mechanisms by which metastases and tumors get colonized and it would be very interesting to find differences and therefore maybe optimize the treatment of metastases by understanding the factors, which contribute to viral colonization.

5.1.7 Histological analysis reveal the differences between primary tumor and lymph node metastases

After the preferential colonization of C33A-RFP tumors compared to lymph node metastases was demonstrated, it was interesting to investigate whether there are differences between primary tumor and metastases which might explain these findings. In the publication by Donat *et al*. it was hypothesized that the preferential colonization of PC-3 lymph node metastases might be influenced by different factors:[137] first of all, the proliferative status of cells in tumor and metastatic tissue was determined. It was shown that there were higher amounts of proliferative cells in lymph node metastases, compared to primary tumor while the amount of necrotic area was significantly higher in tumor tissue. Additionally, the amount of immune cells was higher in lymph nodes compared to primary tumors. And finally the diameter of blood

vessels in lymph nodes was higher compared to those in tumors, strongly correlating with a higher vascular permeability. All these findings are supposed to have an impact on preferential virus colonization of lymph nodes.

Therefore, these factors were analyzed for the C33A-RFP model as well, to find differences explaining the different order of viral colonization in this model.

First of all, the proliferative status of cells in solid tumors and lymph node metastases was determined, by staining with Ki67. GLV-1h68 has a deletion in the locus encoding for TK.[84] Therefore, the virus is strongly dependent on cellular TK for successful virus replication.[165] Highly proliferative cells do have higher cellular TK levels offering better replication modalities for GLV-1h68 than non-proliferating cells. The levels of proliferative cells in tumors and lymph node metastases of C33A-RFP were comparable to those of PC-3. In lymph node metastases significantly more Ki67 stained areas were found compared to the primary tumor. These findings were confirmed by the fact that single-cell suspension cells isolated from lymph node metastases divided faster compared to those isolated from solid tumors. Both, indicating, that lymph node metastases have a higher proliferative status compared to solid tumors in the C33A-RFP model. However, the necrotic area which is not favorable for viral replication was significantly higher in tumors compared to metastases.

In conclusion, the proliferative status alone does not have a crucial impact on viral replication, but there might be more factors, influencing viral replication. One of those might be the amount of immune cells in the particular tissue. It was found, that the amount of monocytes, B cells and natural killer cells, was significantly higher in lymph node metastases compared to primary tumors. However, this is no surprise, because lymph nodes represent not only a venue for lymph filtration but also for antigen surveillance, lymphocyte production, and antibody secretion and therefore represent essential organs of the immune system.[166] However there is evidence, that vaccinia virus is able to infect immune cells, the virus does not replicate in monocytes, NK cells and B cells efficiently.[167] The function of the immune system is to protect the body from viral and bacterial infections. Therefore, high amounts of immune cells might lead to faster clearance of the virus. However, enough virus seems to reach lymph nodes and find a suitable niche with enough infectable cancer cells to lyse, so lymph node metastases are

successfully reduced. Thus, the immune cells in lymph nodes might influence viral colonization, for example by clearing the virus from the tissue or by forming targets for viral infection.

The next factor analyzed was the blood and lymph vessel density and vascular permeability. In the C33A-RFP model, the vessel density, for both lymph and blood vessels, was significantly higher in lymph node metastases compared to solid tumors, however, surprisingly, no differences of extravagated protein were detected, indicating the vascular permeability in these two tissues. These findings of same levels extravagated protein combined with the lower amount of vessels in the primary tumor tissue lead to the assumption, that the blood vessels in tumor are leakier compared to those in metastases, leading to higher viral titers in tumors.

Taken together, the colonization pattern in the C33A model can be explained by the analyzed factors. The tumor has a greater mass than metastases correlating with a higher amount of infectable tumor cells. The virus can easier reach the tumor where it can infect a bigger amount of tumor cells and replicate within. Afterwards, the virus spreads to lymph node metastases, via lymph and/or blood vessels draining from the tumor to lymph nodes. Here, the conditions are most likely not that favorable, like an active immune system or less tumor cells to infect, but nevertheless, the virus is able to infect and lyse metastatic cancer cells. Unfortunately, the factors analyzed so far do not explain the different colonization pattern in C33A and PC-3.

5.1.8 Conclusion

Summing up the first part of this thesis, it was possible to establish the cervical cancer cell line C33A-RFP as a new metastatic xenograft mouse model. After implantation of C33A-RFP cells in immune compromised nude mice tumors developed, together with lymph node and lung metastases. Furthermore, the administration of the oncolytic vaccinia virus GLV-1h68 led to the reduction of primary tumor size, but also to a massive regression of metastatic burden, for both, lymph node metastases and haematogenous metastases in the lung. Finally, it was demonstrated, that GLV-1h68 preferentially colonizes the primary tumor. The reason for this are yet unclear, but it is hypothesized that the high vascular permeability and the high amount of different immune cell populations might contribute to these findings.

5.2 B16F10 as a promising tool to analyze oncolytic virus therapy in an immune competent mouse model

In the first part of this thesis a new metastatic model to study the influence of oncolytic vaccinia virus on metastases was successfully established. Unfortunately, the C33A cell line is a human cancer cell line and can therefore only be implanted into immune compromised mice. However, it is indispensable to find a metastatic model in an immune competent mouse model background, because the immune system has a great impact on the virus, especially the complement system.[168] A possible cell line to study oncolytic virus therapy might be the murine metastatic melanoma cell line B16F10, because it is described to metastasize to sentinel lymph node and organs like lungs.[145,169] Moreover, it was already possible to detect GLV-1h68 in draining lymph nodes after intratumoral administration.[96] Therefore, it was considered to use the B16F10 cells in a C57BL/6 immune competent mouse strain to analyze the effects of oncolytic virus therapy.

5.2.1 LIVP 1.1.1 is more efficiently infecting, replicating in and lysing B16F10 cells compared to GLV-1h68 in cell culture

To treat the metastatic human cancer cell line C33A the attenuated oncolytic vaccinia virus GLV-1h68 was used. Unfortunately, this virus might be too attenuated for treatment of murine cancer. Chen *et al.* postulated that the insertion of the three expression cassettes lead to a reduced efficiency of viral replication together with antitumor efficacy and virulence.[170] Therefore, it was considered to use the parental strain LIVP 1.1.1 which has indeed different mutations, among them in the gene for thymidine kinase, but no inserted expression cassettes.

First of all, it was confirmed in cell culture experiments, that LIVP 1.1.1 is more efficient in infection, replication, and cell lysis in mouse cells than GLV-1h68. The replication capability of both viruses in B16F10 cells was analyzed by a standard plaque assay, with MOI 1 and MOI 5. Like already expected the viral titer in cells infected with LIVP 1.1.1 was significantly higher compared to those infected with GLV-1h68. This was on the one hand true for cells and supernatant and on the other hand for infection with MOI 1 and MOI 5. These findings confirm that LIVP 1.1.1 is more efficiently in infecting and replicating in B16F10 cells.

Moreover, the cytotoxic effect of LIVP 1.1.1 was compared to the one of GLV-1h68, by XTT assay. Like the previous experiment indicated, LIVP 1.1.1 was also more efficiently lysing infected B16F10 cells. However, this was only true for infection with MOI 5. After infection with MOI 1, the cell amount decreased at the beginning, but at later time points cell amount started to increase again upon infection with both viruses. The explanation for this is that the doubling time of B16F10 cells is about 20 hours,[171] while the replication cycle of vaccinia virus, resulting in cell lysis may take up to 24 hours.[172] This means, cells were growing faster than they got lysed clarifying the increasing cell amount. This was also the case when infecting the cells with GLV-1h68 at an MOI 5. Nevertheless at MOI 5 cells infected with LIVP 1.1.1 were efficiently lysed. Nonetheless, these results indicate that infection of B16F10 is impaired, therefore, it has to be considered later in mouse experiments, that high amounts of virus have to be used to achieve efficient productive infection.

Taken together LIVP 1.1.1 was more efficiently infecting, replicating in and lysing B16F10 cells compared to GLV-1h68. This is the reason why in ongoing experiments LIVP 1.1.1 was used to study the effects of oncolytic virus therapy on tumors and metastases of B16F10 cells.

5.2.2 Implantation of B16F10 cells into the footpad of immunocompetent C57BL/6 mice as a model to study metastases

Prior fighting metastases it is necessary to establish a metastatic model, reflecting the outcome of a metastatic disease in human patients and providing metastases with a high presumption. Common implantation sites for B16F10 cells are subcutaneous on the abdominal flank,[173] or into the footpad of mice which is already described to result in sentinel lymph node metastases.[96,145,169] Therefore, it was first of all set out to compare the metastatic burden after subcutaneous and footpad implantation. The findings of these experiments indicate that obviously subcutaneous implantation into the flank did not lead to a suitable metastatic model. Based on the fact that B16F10 is a melanoma cell line, tumorous tissue is indicated by a blackish coloration. In five mice only one black colored lumbar lymph node was observed and no metastases in other organs. Moreover, lymph nodes were not significantly enlarged. B16F10 is described to be a highly aggressive and metastatic cell line,[174] although, hardly no metastases were observed. This might be due the rapid growth of the primary tumor. Due to ethical reasons the experiments had to be terminated when the tumor burden got too big. The short

time span did not result in efficient tumor cell dissemination and metastasis formation. In contrast, implantation of B16F10 cells into the footpad lead to a higher metastatic burden, at least in lymph nodes: lymph nodes were significantly enlarged and in all lymph nodes black cells or even whole black areas were detectable. Obviously, footpad implantation of B16F10 cells led to sentinel lymph node metastases with a high presumption and therefore B16F10 is a suitable model to study oncolytic virus therapy on metastases. The next step was to compare footpad implantation in nude and in C57BL/6 mice. All in all, no differences between both mouse strains were observed. On the one hand, survival and net body weight was equal, indicating that the general fitness was the same in both strains. On the other hand, the sentinel popliteal lymph node volume was in both cases significantly larger compared to untreated popliteal lymph nodes. Obviously, B16F10 implanted into C57BL/6 mice is as suitable as a metastatic model when compared to implantation in nude mice. Thus, the effects of LIVP 1.1.1 on metastases in these two models can be compared and by this, the influence of the immune system on the cancer treatment can be analyzed in detail.

5.2.3 Formation of tumors and sentinel lymph node metastases after implantation of B16F10 cells in the footpad

The next step was to characterize the formation of tumors and draining lymph node metastases after implantation into the footpad in detail.

Primary tumors started to develop from day 10 after implantation. Afterwards, the tumors showed a continuous growth until the end of the experiment. Like already described above, tumors were very fast growing, leading to a short time period for metastases to develop. Nonetheless, in accordance to tumor volume, the volume of the popliteal lymph node at the tumor-bearing site was also increasing in the course of the experiment. Moreover an invasion of colored melanoma cells was observed. Interestingly, not only black invaded cells were visible but also reddish-brown colored tumor cells. Generally, two different forms of melanin can be observed: the brownish black eumelanin and the reddish yellow pheomelanin.[175] Both types are present in hair and in the epidermis in different concentrations, dependent on the color. Besides, both types are also found in melanoma in general, including B16 melanomas.[176] Obviously both cell types, either containing eumelanin or pheomelanin, are able to migrate and form distant metastases. All in all, a coloration was observed in almost all popliteal lymph nodes

15 and 20 dpti indicating that this is a good metastatic model because sentinel lymph nodes got metastasized with a high presumption. The time point when lymph nodes got metastasized, which was 10-15 dpti in this case, is of importance when planning experiments with virus treatment of tumors and lymph node metastases. When virus is administered at earlier time points, it is possible to investigate whether virus treatment can prevent lymph node metastasis formation. When administration is done at later time points, the ability of the vaccinia virus to fight established lymph node metastases can be analyzed.

However, no distant lymph node metastases or lung metastases were detectable, although this implantation site was already described to result in lung metastases.[169] Nevertheless, also in this publication tumors were described as very fast growing and lung metastases developed only at later time points, after surgical resection of the primary tumor. Therefore, it was not surprising that in the mice in this present study no lung metastases were detected.

5.2.4 Intratumoral virus injection leads to higher titers in tumors and lymph node metastases compared to intravenous injection

B16F10 footpad implantation was established as a useful model to investigate the efficacy of virus treatment on metastases. However, prior to successful therapy, it was necessary to find the best virus administration route. Based on the fact, that B16F10 is a very fast growing model it is indispensable that as much virus as possible reaches the tumor and the metastases as fast as possible. Different modalities can be optimized to achieve this goal. One possibility is to find an optimal administration route. On the other hand, the immune system can help the virus fighting cancer but on the other hand the immune system can pose a challenge, because after intravenous administration virus is rapidly cleared from the blood stream by the immune system.[146,147] Before a successful therapy with the oncolytic virus is possible, these difficulties have to been overcome first. Therefore intravenous injection was compared to intratumoral injection. The advantage of latter administration route is that the virus is directly injected into the tumor. Thus, the virus can avoid the blood circulation and the clearance from the blood by the complement system.[168]

The results of this experiment revealed, that after intravenous injection 48 hpi virus is indeed detectable in tumors in the footpad of mice. However, no virus was found in any of the sentinel

PNs, indicating that this method is not useful for successful virus colonization in lymph node metastases. On the other hand, after intratumoral injection virus was detectable in tumors, even with a higher viral titer compared to intravenous injection. Obviously, more virus reached the tumor after intratumoral injection compared to intravenous injection, indicating that by injection into the tumor virus clearance from the blood stream by the complement system can be avoided. Moreover, virus was also found in PNs of all tumor-bearing mice, demonstrating that after intratumoral injection, virus does not only stay in the primary tumor, but spreads to sentinel lymph node metastases. Obviously intratumoral injection is a suitable administration route to study the effects of oncolytic virus therapy on metastases in the B16F10 footpad model.

5.2.5 Outlook

B16F10 cells implanted into the footpad of C57BL/6 mice offer a suitable platform to further analyze oncolytic virus therapy on metastases. Unfortunately, this model has some limitations. For example, only the sentinel lymph nodes got metastasized in this study as well as in others.[96] However, it would be favorable to have a metastatic model in which not only sentinel lymph nodes got metastasized, but also distant lymph nodes. Moreover, a model developing haematogenous metastases would be interesting. B16F10 tumors are growing too fast to develop lung metastases. Here, a well-established model would be the intravenous injection of B16F10 cell into the tail vein. For this method, the formation of lung metastases was already described.

6 References

1. WHO. *Cancer- Fact sheet N°297*.; 2014.

2. Deutsche Krebshilfe e.V. 2014.

3. Wagener C, Müller O. *Molekulare Onkologie*. 3rd Editio. Stuttgart - New York: Thieme Verlag; 2010.

4. Willett WC, Stampfer MJ, Colditz GA, Rosner BA, Speizer FE. Relation of meat, fat, and fiber intake to the risk of colon cancer in a prospective study among women. *N Engl J Med*. 1990;323:1664-1672. doi:10.1056/NEJM199012133232404.

5. Hoffmann D, Hecht SS, Ornaf RM, Wynder EL, Tso TC. Chemical studies on tobacco smoke. XLII. Nitrosonornicotine: presence in tobacco, formation and carcinogenicity. *IARC Sci Publ*. 1976;(14):307-320.

6. Schottenfeld D. Alcohol as a co-factor in the etiology of cancer. *Cancer*. 1979;43:1962-1966.

7. Emmett EA, Epstein JH. Ultraviolet Radiation as a Cause of Skin Tumors. *Crit Rev Toxicol*. 1973;2:211-255. doi:10.3109/10408447309025703.

8. Eslick GD, Lim LL, Byles JE, Xia HH, Talley NJ. Association of Helicobacter pylori infection with gastric carcinoma: a meta-analysis. *Am J Gastroenterol*. 1999;94(9):2373-9. doi:10.1111/j.1572-0241.1999.01360.x.

9. Zur Hausen H. Papillomaviruses in human cancer. *Appl Pathol*. 1987;5:19-24. doi:10.1046/j.1525-1381.1999.99723.x.

10. Caporaso N, Romano M, Marmo R, et al. Hepatitis C virus infection is an additive risk factor for development of hepatocellular carcinoma in patients with cirrhosis. *J Hepatol*. 1991;12:367-371. doi:10.1016/0168-8278(91)90841-X.

11. Murken J, Grimm T, Holinski-Feder E. *Taschenlehrbuch Humangenetik*. Thieme Verlag; 2006.

12. Hanahan D, Weinberg R a. Hallmarks of cancer: the next generation. *Cell*. 2011;144(5):646-74. doi:10.1016/j.cell.2011.02.013.

13. Benninghoff A, Drenkhahn D. *Taschenbuch Anatomie*. (Drenckhahn D, Waschke J, eds.). 1.Auflage Urban und Fischer; 2008.

14. Vittet D. Lymphatic collecting vessel maturation and valve morphogenesis. *Microvascular Research*. 2014.

15. Alitalo K, Carmeliet P. Molecular mechanisms of lymphangiogenesis in health and disease. *Cancer Cell*. 2002;1:219-227. doi:10.1016/S1535-6108(02)00051-X.

16. http://www.britannica.com/EBchecked/topic/352744/lymph-node.

17. Lüllman-Rauch R. *Histologie*. Thieme Verlag; 2003.

18. Von Andrian UH, Mempel TR. Homing and cellular traffic in lymph nodes. *Nat Rev Immunol*. 2003;3:867-878. doi:10.1038/nri1222.

19. Sahai E. Illuminating the metastatic process. *Nat Rev Cancer*. 2007;7:737-749. doi:10.1038/nrc2229.

20. Liebig C, Ayala G, Wilks JA, Berger DH, Albo D. Perineural invasion in cancer: A review of the literature. *Cancer*. 2009;115:3379-3391. doi:10.1002/cncr.24396.

21. Gil Z, Cavel O, Kelly K, et al. Paracrine regulation of pancreatic cancer cell invasion by peripheral nerves. *J Natl Cancer Inst*. 2010;102:107-118. doi:10.1093/jnci/djp456.

22. Bacac M, Stamenkovic I. Metastatic cancer cell. *Annu Rev Pathol*. 2008;3:221-247. doi:10.1146/annurev.pathmechdis.3.121806.151523.

23. Tan DS, Agarwal R, Kaye SB. Mechanisms of transcoelomic metastasis in ovarian cancer. *Lancet Oncol*. 2006;7:925-934. doi:10.1016/S1470-2045(06)70939-1.

24. Yamamoto Y, Yamada M, Nakamura K, Takahashi Y, Miyamoto T. *Nephroblastoma with transcoelomic metastasis in a Japanese black bull.* The Journal of veterinary medical science / the Japanese Society of Veterinary Science 68, 891-893 (2006). doi:10.1292/jvms.68.891.

25. Lee JJ, Lotze MT. Molecular basis of metastasis. *N Engl J Med*. 2009;360:1679; author reply 1679-1680. doi:10.1056/NEJMra0805239.

26. Chaffer CL, Weinberg RA. A perspective on cancer cell metastasis. *Science*. 2011;331:1559-1564. doi:10.1126/science.1203543.

27. Perl AK, Wilgenbus P, Dahl U, Semb H, Christofori G. A causal role for E-cadherin in the transition from adenoma to carcinoma. *Nature*. 1998;392:190-193. doi:10.1038/32433.

28. Fidler IJ. Metastasis: guantitative analysis of distribution and fate of tumor embolilabeled with 125 I-5-iodo-2'-deoxyuridine. *J Natl Cancer Inst*. 1970;45:773-782.

29. Wong CW, Song C, Grimes MM, et al. Intravascular location of breast cancer cells after spontaneous metastasis to the lung. *Am J Pathol*. 2002;161:749-753. doi:10.1016/S0002-9440(10)64233-2.

30. Hedley BD, Chambers AF. Chapter 3 Tumor Dormancy and Metastasis. *Adv Cancer Res*. 2009;102:67-101. doi:10.1016/S0065-230X(09)02003-X.

31. Jain RK. Transport of molecules across tumor vasculature. *CANCER METASTASIS Rev*. 1987;6:559-593. doi:10.1007/BF00047468.

32. Gunn MD, Tangemann K, Tam C, Cyster JG, Rosen SD, Williams LT. A chemokine expressed in lymphoid high endothelial venules promotes the adhesion and chemotaxis of naive T lymphocytes. *Proc Natl Acad Sci U S A*. 1998;95:258-263. doi:10.1073/pnas.95.1.258.

33. Shields JD, Fleury ME, Yong C, Tomei AA, Randolph GJ, Swartz MA. Autologous Chemotaxis as a Mechanism of Tumor Cell Homing to Lymphatics via Interstitial Flow and Autocrine CCR7 Signaling. *Cancer Cell*. 2007;11:526-538. doi:10.1016/j.ccr.2007.04.020.

34. Müller A, Homey B, Soto H, et al. Involvement of chemokine receptors in breast cancer metastasis. *Nature*. 2001;410:50-56. doi:10.1038/35065016.

35. Paget S. The distribution of secondary growths in cancer of the breast. 1889. *Cancer Metastasis Rev*. 1989;8:98-101. doi:10.1016/S0140-6736(00)49915-0.

36. SUGARBAKER ED. The organ selectivity of experimentally induced metastases in rats. *Cancer*. 1952;5:606-612. doi:10.1002/1097-0142.

37. Fidler IJ, Poste G. The “seed and soil” hypothesis revisited. *Lancet Oncol*. 2008;9:808. doi:10.1016/S1470-2045(08)70201-8.

38. Clarke MF, Dick JE, Dirks PB, et al. Cancer stem cells - Perspectives on current status and future directions: AACR workshop on cancer stem cells. In: *Cancer Research*.Vol 66.; 2006:9339-9344. doi:10.1158/0008-5472.CAN-06-3126.

39. Wellner UF, Hopt UT, Brabletz T. Tumorstammzellen und metastasierung. *Zentralblatt fur Chir - Zeitschrift fur Allg Visz und Gefasschirurgie*. 2010;135:318-322. doi:10.1055/s-0030-1247470.

40. Mani SA, Guo W, Liao MJ, et al. The Epithelial-Mesenchymal Transition Generates Cells with Properties of Stem Cells. *Cell*. 2008;133:704-715. doi:10.1016/j.cell.2008.03.027.

41. Zeisberg M, Neilson EG. Biomarkers for epithelial-mesenchymal transitions. *J Clin Invest*. 2009;119:1429-1437. doi:10.1172/JCI36183.

42. Morel A-P, Lièvre M, Thomas C, Hinkal G, Ansieau S, Puisieux A. Generation of breast cancer stem cells through epithelial-mesenchymal transition. *PLoS One*. 2008;3:e2888. doi:10.1371/journal.pone.0002888.

43. Wellner U, Schubert J, Burk UC, et al. The EMT-activator ZEB1 promotes tumorigenicity by repressing stemness-inhibiting microRNAs. *Nat Cell Biol*. 2009;11:1487-1495. doi:10.1038/ncb1998.

44. Brabletz T, Jung A, Spaderna S, Hlubek F, Kirchner T. Opinion: migrating cancer stem cells - an integrated concept of malignant tumour progression. *Nat Rev Cancer*. 2005;5:744-749. doi:10.1038/nrc1694.

45. Thiery JP. Epithelial-mesenchymal transitions in tumour progression. *Nat Rev Cancer*. 2002;2:442-454. doi:10.1038/nrc822.

46. Shimono Y, Zabala M, Cho RW, et al. Downregulation of miRNA-200c Links Breast Cancer Stem Cells with Normal Stem Cells. *Cell*. 2009;138:592-603. doi:10.1016/j.cell.2009.07.011.

47. Sporn MB. The war on cancer. *Lancet*. 1996;347(9012):1377-1381. doi:10.1016/S0140-6736(96)91015-6.

48. Sleeman J, Steeg PS. Cancer metastasis as a therapeutic target. *Eur J Cancer*. 2010;46:1177-1180. doi:10.1016/j.ejca.2010.02.039.

49. Suit HD. Local control and patient survival. *Int J Radiat Oncol Biol Phys*. 1992;23:653-660.

50. Steeg PS, Theodorescu D. Metastasis: a therapeutic target for cancer. *Nat Clin Pract Oncol*. 2008;5:206-219. doi:10.1038/ncponc1066.

51. Schroeder A, Heller DA, Winslow MM, et al. Treating metastatic cancer with nanotechnology. *Nat Rev Cancer*. 2011;12:39-50. doi:10.1038/nrc3180.

52. Wang J, Tian S, Petros RA, Napier ME, Desimone JM. The complex role of multivalency in nanoparticles targeting the transferrin receptor for cancer therapies. *J Am Chem Soc*. 2010;132:11306-11313. doi:10.1021/ja1043177.

53. Li Z, Xiang J, Zhang W, et al. Nanoparticle delivery of anti-metastatic NM23-H1 gene improves chemotherapy in a mouse tumor model. *Cancer Gene Ther*. 2009;16:423-429. doi:10.1038/cgt.2008.97.

54. Davis ME, Zuckerman JE, Choi CHJ, et al. Evidence of RNAi in humans from systemically administered siRNA via targeted nanoparticles. *Nature*. 2010;464:1067-1070. doi:10.1038/nature08956.

55. Li S-D, Chono S, Huang L. Efficient oncogene silencing and metastasis inhibition via systemic delivery of siRNA. *Mol Ther*. 2008;16:942-946. doi:10.1038/mt.2008.51.

56. Ivkov R, DeNardo SJ, Daum W, et al. Application of high amplitude alternating magnetic fields for heat induction of nanoparticles localized in cancer. In: *Clinical Cancer Research*.Vol 11.; 2005. doi:10.1158/1078-0432.CCR-1004-0016.

57. Lal S, Clare SE, Halas NJ. Nanoshell-enabled photothermal cancer therapy: Impending clinical impact. *Acc Chem Res*. 2008;41:1842-1851. doi:10.1021/ar800150g.

58. Miele E, Spinelli GP, Miele E, Tomao F, Tomao S. Albumin-bound formulation of paclitaxel (Abraxane® ABI-007) in the treatment of breast cancer. *Int J Nanomedicine*. 2009;4:99-105. doi:10.2147/IJN.S3061.

59. Eccles S, Paon L, Sleeman J. Lymphatic metastasis in breast cancer: importance and new insights into cellular and molecular mechanisms. *Clin Exp Metastasis*. 2007;24:619-636. doi:10.1007/s10585-007-9123-5.

60. Henderson DA, Moss B. Smallpox and Vaccinia Chapter 6. In: *Vaccines 3rd Edition*.; 1999:74-97.

61. Fenner F, Henderson DA, Arita I, Jezek Z, Ladnyi ID. Smallpox and its eradication. *WHO Geneva*. 1988.

62. Kirn DH, Thorne SH. Targeted and armed oncolytic poxviruses: a novel multi-mechanistic therapeutic class for cancer. *Nat Rev Cancer*. 2009;9(1):64-71. doi:10.1038/nrc2545.

63. Smith GL, Moss B. Infectious poxvirus vectors have capacity for at least 25,000 base pairs of foreign DNA. *Gene*. 1983;25(1):21-28.

64. Shen Y, Nemunaitis J. Fighting cancer with vaccinia virus: teaching new tricks to an old dog. *Mol Ther*. 2005;11(2):180-95. doi:10.1016/j.ymthe.2004.10.015.

65. Zeh HJ, Bartlett DL. Development of a replication-selective, oncolytic poxvirus for the treatment of human cancers. *Cancer Gene Ther*. 2002;9:1001-1012. doi:10.1038/sj.cgt.7700549.

66. Timiryasova TM, Chen B, Haghighat P, Fodor I. Vaccinia virus-mediated expression of wild-type p53 suppresses glioma cell growth and induces apoptosis. *Int J Oncol*. 1999;14:845-854. doi:10.3892/ijo.14.5.845.

67. Harrison SC, Alberts B, Ehrenfeld E, et al. Discovery of antivirals against smallpox. *Proc Natl Acad Sci U S A*. 2004;101(31):11178-92. doi:10.1073/pnas.0403600101.

68. Modrow S, Falke D, Truyen U, Schätzl H. *Molekulare Virologie*. Heidelberg: Spektrum Akademischer Verlag; 2010. doi:10.1007/978-3-8274-2241-5.

69. Smith GL, Vanderplasschen A, Law M. The formation and function of extracellular enveloped vaccinia virus. *J Gen Virol*. 2002;83(Pt 12):2915-31.

70. McFadden G. Poxvirus tropism. *Nat Rev Microbiol*. 2005;3(3):201-13. doi:10.1038/nrmicro1099.

71. Hsiao JC, Chung CS, Chang W. Vaccinia virus envelope D8L protein binds to cell surface chondroitin sulfate and mediates the adsorption of intracellular mature virions to cells. *J Virol*. 1999;73(10):8750-61.

72. Lin CL, Chung CS, Heine HG, Chang W. Vaccinia virus envelope H3L protein binds to cell surface heparan sulfate and is important for intracellular mature virion morphogenesis and virus infection in vitro and in vivo. *J Virol*. 2000;74(7):3353-65.

73. Vázquez MI, Esteban M. Identification of functional domains in the 14-kilodalton envelope protein (A27L) of vaccinia virus. *J Virol*. 1999;73(11):9098-109.

74. Chung CS, Hsiao JC, Chang YS, Chang W. A27L protein mediates vaccinia virus interaction with cell surface heparan sulfate. *J Virol*. 1998;72(2):1577-85..

75. Carter GC, Law M, Hollinshead M, Smith GL. Entry of the vaccinia virus intracellular mature virion and its interactions with glycosaminoglycans. *J Gen Virol*. 2005;86(Pt 5):1279-90. doi:10.1099/vir.0.80831-0.

76. Townsley AC, Weisberg AS, Wagenaar TR, Moss B. Vaccinia virus entry into cells via a low-pH-dependent endosomal pathway. *J Virol*. 2006;80(18):8899-908. doi:10.1128/JVI.01053-06.

77. Roberts KL, Smith GL. Vaccinia virus morphogenesis and dissemination. *Trends Microbiol*. 2008;16(10):472-9. doi:10.1016/j.tim.2008.07.009.

78. Law M, Carter GC, Roberts KL, Hollinshead M, Smith GL. Ligand-induced and nonfusogenic dissolution of a viral membrane. *Proc Natl Acad Sci U S A*. 2006;103(15):5989-94. doi:10.1073/pnas.0601025103.

79. Smith GL, Sanderson CM. Cell motility and cell morphology: How some viruses take control. *Expert Rev Mol Med*. 1999;1999(10):1-16. doi:10.1017/S1462399499000629.

80. Tolonen N, Doglio L, Schleich S, Krijnse Locker J. Vaccinia virus DNA replication occurs in endoplasmic reticulum-enclosed cytoplasmic mini-nuclei. *Mol Biol Cell*. 2001;12(7):2031-46.

81. Moss B, Ward BM. High-speed mass transit for poxviruses on microtubules. *Nat Cell Biol*. 2001;3(11):E245-6. doi:10.1038/ncb1101-e245.

82. Gentschev I, Adelfinger M, Josupeit R, et al. Preclinical evaluation of oncolytic vaccinia virus for therapy of canine soft tissue sarcoma. *PLoS One*. 2012;7(5):e37239. doi:10.1371/journal.pone.0037239.

83. Advani SJ, Buckel L, Chen NG, et al. Preferential replication of systemically delivered oncolytic vaccinia virus in focally irradiated glioma xenografts. *Clin Cancer Res*. 2012;18(9):2579-90. doi:10.1158/1078-0432.CCR-11-2394.

84. Zhang Q, Yu YA, Wang E, et al. Eradication of solid human breast tumors in nude mice with an intravenously injected light-emitting oncolytic vaccinia virus. *Cancer Res*. 2007;67(20):10038-46. doi:10.1158/0008-5472.CAN-07-0146.

85. Hengstschläger M, Knöfler M, Müllner EW, Ogris E, Wintersberger E, Wawra E. Different regulation of thymidine kinase during the cell cycle of normal versus DNA tumor virus-transformed cells. *J Biol Chem*. 1994;269(19):13836-42.

86. Buller RML, Smith GL, Cremer K, Notkins AL, Moss B. Decreased virulence of recombinant vaccinia virus expression vectors is associated with a thymidine kinase-negative phenotype. *Nature*. 1985;317(6040):813-815. doi:10.1038/317813a0.

87. Shida H, Hinuma Y, Hatanaka M, et al. Effects and virulences of recombinant vaccinia viruses derived from attenuated strains that express the human T-cell leukemia virus type I envelope gene. *J Virol*. 1988;62(12):4474-80.

88. Dehaven BC, Gupta K, Isaacs SN. The vaccinia virus A56 protein: a multifunctional transmembrane glycoprotein that anchors two secreted viral proteins. *J Gen Virol*. 2011;92(Pt 9):1971-80. doi:10.1099/vir.0.030460-0.

89. Izmailyan R, Chang W. Vaccinia virus WR53.5/F14.5 protein is a new component of intracellular mature virus and is important for calcium-independent cell adhesion and vaccinia virus virulence in mice. *J Virol*. 2008;82(20):10079-87. doi:10.1128/JVI.00816-08.

90. Zhang Q, Liang C, Yu YA, Chen N, Dandekar T, Szalay AA. The highly attenuated oncolytic recombinant vaccinia virus GLV-1h68: comparative genomic features and the contribution of F14.5L inactivation. *Mol Genet Genomics*. 2009;282(4):417-35. doi:10.1007/s00438-009-0475-1.

91. Gentschev I, Müller M, Adelfinger M, et al. Efficient colonization and therapy of human hepatocellular carcinoma (HCC) using the oncolytic vaccinia virus strain GLV-1h68. *PLoS One*. 2011;6(7):e22069. doi:10.1371/journal.pone.0022069.

92. Gentschev I, Donat U, Hofmann E, et al. Regression of human prostate tumors and metastases in nude mice following treatment with the recombinant oncolytic vaccinia virus GLV-1h68. *J Biomed Biotechnol*. 2010;2010:489759. doi:10.1155/2010/489759.

93. Kelly KJ, Woo Y, Brader P, et al. Novel oncolytic agent GLV-1h68 is effective against malignant pleural mesothelioma. *Hum Gene Ther*. 2008;19(8):774-82. doi:10.1089/hum.2008.036.

94. Yu Z, Li S, Brader P, et al. Oncolytic vaccinia therapy of squamous cell carcinoma. *Mol Cancer*. 2009;8:45. doi:10.1186/1476-4598-8-45.

95. Gentschev I, Ehrig K, Donat U, et al. Significant Growth Inhibition of Canine Mammary Carcinoma Xenografts following Treatment with Oncolytic Vaccinia Virus GLV-1h68. *J Oncol*. 2010;2010:736907. doi:10.1155/2010/736907.

96. Kelly KJ, Brader P, Woo Y, et al. Real-time intraoperative detection of melanoma lymph node metastases using recombinant vaccinia virus GLV-1h68 in an immunocompetent animal model. *Int J Cancer*. 2009;124(4):911-8. doi:10.1002/ijc.24037.

97. Adelfinger M, Gentschev I, De Guibert JG, et al. Evaluation of a new recombinant oncolytic vaccinia virus strain GLV-5b451 for feline mammary carcinoma therapy. *PLoS One*. 2014;9. doi:10.1371/journal.pone.0104337.

98. https://clinicaltrials.gov/ct2/results?term=GL-ONC+1&Search=Search.

99. WHO. Human papillomavirus (HPV) and cervical cancer- Fact sheet N° 380. 2014.

100. Stewart B, Wild CP. *World Cancer Report 2014 (WHO)*. WHO; 2014.

101. Jemal A, Center MM, DeSantis C, Ward EM. Global patterns of cancer incidence and mortality rates and trends. *Cancer Epidemiol Biomarkers Prev*. 2010;19:1893-1907. doi:10.1158/1055-9965.EPI-10-0437.

102. Boyle P, Levin B. *World Cancer Report 2008 (WHO)*. Lyon: WHO; 2008.

103. Haag P, Hanhart N, Müller M. *Gynäkologie und Urologie*. 4th Editio. Medizinische Verlags- und Informationsdienste; 2008.

104. Benedet JL, Bender H, Jones H, Ngan HY, Pecorelli S. FIGO staging classifications and clinical practice guidelines in the management of gynecologic cancers. FIGO Committee on Gynecologic Oncology. *Int J Gynaecol Obstet*. 2000;70:209-262. doi:10.1016/S0020-7292(00)90001-8.

105. Camisão CC, Brenna SMF, Lombardelli KVP, Djahjah MCR, Zeferino LC. Magnetic resonance imaging in the staging of cervical cancer. *Radiol Bras*. 2007;40. doi:10.1590/S0100-39842007000300014.

106. Gadducci A, Barsotti C, Cosio S, Domenici L, Riccardo Genazzani A. Smoking habit, immune suppression, oral contraceptive use, and hormone replacement therapy use and cervical carcinogenesis: a review of the literature. *Gynecol Endocrinol*. 2011;27:597-604. doi:10.3109/09513590.2011.558953.

107. Jensen KE, Schmiedel S, Frederiksen K, Norrild B, Iftner T, Kjær SK. Risk for cervical intraepithelial neoplasia grade 3 or worse in relation to smoking among women with persistent human papillomavirus infection. *Cancer Epidemiol Biomarkers Prev*. 2012;21:1949-1955. doi:10.1158/1055-9965.EPI-12-0663.

108. Appleby P, Beral V, Berrington De González A, et al. Carcinoma of the cervix and tobacco smoking: Collaborative reanalysis of individual data on 13,541 women with carcinoma of the cervix and 23,017 women without carcinoma of the cervix from 23 epidemiological studies. *Int J Cancer*. 2006;118:1481-1495. doi:10.1002/ijc.21493.

109. Vaisy A, Lotfinejad S, Zhian F. Risk of cancer with combined oral contraceptive use among Iranian women. *Asian Pacific J Cancer Prev*. 2014;14:5517-5522. doi:10.7314/APJCP.2014.15.14.5517.

110. Boshart M, Gissmann L, Ikenberg H, Kleinheinz A, Scheurlen W, zur Hausen H. A new type of papillomavirus DNA, its presence in genital cancer biopsies and in cell lines derived from cervical cancer. *EMBO J*. 1984;3:1151-1157.

111. Dürst M, Gissmann L, Ikenberg H, zur Hausen H. A papillomavirus DNA from a cervical carcinoma and its prevalence in cancer biopsy samples from different geographic regions. *Proc Natl Acad Sci U S A*. 1983;80:3812-3815. doi:10.1073/pnas.80.12.3812.

112. Gissmann L, Boshart M, Dürst M, Ikenberg H, Wagner D, zur Hausen H. Presence of human papillomavirus in genital tumors. *J Invest Dermatol*. 1984;83:26s-28s. doi:10.1111/1523-1747.ep12281143.

113. Muñoz N, Bosch FX, de Sanjosé S, et al. Epidemiologic classification of human papillomavirus types associated with cervical cancer. *N Engl J Med*. 2003;348:518-527. doi:10.1056/NEJMoa021641.

114. McLemore MR. Gardasil: Introducing the new human papillomavirus vaccine. *Clin J Oncol Nurs*. 2006;10:559-560. doi:10.1188/06.CJON.559-560.

115. Giralgi G, Martinoli L, De Luca d'Alessandro E. The human papillomavirus vaccination: a review of the cost-effectiveness studies. *Clin Ter*. 2014;165(6):426-432. doi:10.7417/CT.2014.1787.

116. Crosbie EJ, Kitchener HC. Cervarix--a bivalent L1 virus-like particle vaccine for prevention of human papillomavirus type 16- and 18-associated cervical cancer. *Expert Opin Biol Ther*. 2007;7:391-396. doi:10.1517/14712598.7.3.391.

117. Kardakis S. Fertility-preserving surgery in patients with early stage cervical carcinoma. *ISRN Oncol*. 2012;2012:817065. doi:10.5402/2012/817065.

118. Waggoner SE. Cervical cancer. In: *Lancet*.Vol 361.; 2003:2217-2225. doi:10.1016/S0140-6736(03)13778-6.

119. Tsao H, Chin L, Garraway LA, Fisher DE. Melanoma: From mutations to medicine. *Genes Dev*. 2012;26:1131-1155. doi:10.1101/gad.191999.112.

120. Jerant AF, Johnson JT, Sheridan CD, Caffrey TJ. Early detection and treatment of skin cancer. *Am Fam Physician*. 2000;62(2):357-368, 375-376, 381-382.

121. Garbe C, Leiter U. Melanoma epidemiology and trends. *Clin Dermatol*. 2009;27:3-9. doi:10.1016/j.clindermatol.2008.09.001.

122. Siegel R, Ma J, Zou Z, Jemal A. Cancer statistics, 2014. *CA Cancer J Clin*. 2014;64:9-29. doi:10.3322/caac.21208.

123. Robert-Koch-Institut. *Krebs in Deutschland 2009/2010*. Zentrum für Krebsregisterdaten; 2013.

124. http://www.melanoma.org.nz/about-melanoma/key-information/.

125. Balch CM, Gershenwald JE, Soong SJ, et al. Final version of 2009 AJCC melanoma staging and classification. *J Clin Oncol*. 2009;27:6199-6206. doi:10.1200/JCO.2009.23.4799.

126. Whiteman DC, Whiteman CA, Green AC. Childhood sun exposure as a risk factor for melanoma: a systematic review of epidemiologic studies. *Cancer Causes Control*. 2001;12:69-82.

127. Boniol M, Autier P, Boyle P, Gandini S. Cutaneous melanoma attributable to sunbed use: systematic review and meta-analysis. *BMJ*. 2012;345:e4757-e4757. doi:10.1136/bmj.e4757.

128. Garibyan L, Fisher DE. How sunlight causes melanoma. *Curr Oncol Rep*. 2010;12:319-326. doi:10.1007/s11912-010-0119-y.

129. Greene MH. The genetics of hereditary melanoma and nevi. 1998 update. *Cancer*. 1999;86:2464-2477. doi:10.1002/(SICI)1097-0142(19991201)86:11

130. Kennedy C, Ter Huurne J, Berkhout M, et al. Melanocortin 1 receptor (MC1R) gene variants are associated with an increased risk for cutaneous melanoma which is largely independent of skin type and hair color. *J Invest Dermatol*. 2001;117:294-300. doi:10.1046/j.0022-202X.2001.01421.x.

131. Rees JL. Genetics of hair and skin color. *Annu Rev Genet*. 2003;37:67-90. doi:10.1146/annurev.genet.37.110801.143233.

132. Shenenberger DW. Cutaneous malignant melanoma: A primary care perspective. *Am Fam Physician*. 2012;85:161-168.

133. http://newportplastic.com/skin-cancer-excision-reconstruction/.

134. Soengas MS, Lowe SW. Apoptosis and melanoma chemoresistance. *Oncogene*. 2003;22:3138-3151. doi:10.1038/sj.onc.1206454.

135. Finn L, Markovic SN, Joseph RW. Therapy for metastatic melanoma: the past, present, and future. *BMC Med*. 2012;10:23. doi:10.1186/1741-7015-10-23.

136. Robert C, Thomas L, Bondarenko I, et al. *Ipilimumab plus dacarbazine for previously untreated metastatic melanoma.*; 2011. doi:10.1056/NEJMoa1104621.

137. Donat U, Weibel S, Hess M, et al. Preferential colonization of metastases by oncolytic vaccinia virus strain GLV-1h68 in a human PC-3 prostate cancer model in nude mice. *PLoS One*. 2012;7(9):e45942. doi:10.1371/journal.pone.0045942.

138. Donat U. Detektion und Therapie von Metastasen des humanen Prostatakarzinoms durch das onkolytische Vaccinia-Virus GLV-1h68 - Dissertation. 2011.

139. Donat U, Rother J, Schäfer S, et al. Characterization of metastasis formation and virotherapy in the human C33A cervical cancer model. *PLoS One*. 2014;9(6):e98533. doi:10.1371/journal.pone.0098533.

140. http://www.oocities.org/virtualbiology/lymph2.html.

141. Dokun AO, Kim S, Smith HR, Kang HS, Chu DT, Yokoyama WM. Specific and nonspecific NK cell activation during virus infection. *Nat Immunol*. 2001;2(10):951-956. doi:10.1038/ni714.

142. Selin LK, Santolucito PA, Pinto AK, Szomolanyi-Tsuda E, Welsh RM. Innate immunity to viruses: control of vaccinia virus infection by gamma delta T cells. *J Immunol*. 2001;166(11):6784-6794. doi:10.4049/jimmunol.166.11.6784.

143. Domagala-kulawik J. The role of the immune system in non-small cell lung carcinoma and potential for therapeutic intervention. 2015;4(2):177-190. doi:10.3978/j.issn.2218-6751.2015.01.11.

144. Finn OJ. Immuno-oncology: Understanding the function and dysfunction of the immune system in cancer. In: *Annals of Oncology*.Vol 23.; 2012. doi:10.1093/annonc/mds256.

145. Harrell MI, Iritani BM, Ruddell A. Tumor-induced sentinel lymph node lymphangiogenesis and increased lymph flow precede melanoma metastasis. *Am J Pathol*. 2007;170(2):774-786. doi:10.2353/ajpath.2007.060761.

146. Alemany R, Suzuki K, Curiel DT. Blood clearance rates of adenovirus type 5 in mice. *J Gen Virol*. 2000;81(11):2605-2609.

147. MIMS CA. The response of mice to large intravenous injections of ectromelia virus. I. The fate of injected virus. *Br J Exp Pathol*. 1959;40:533-542.

148. Coghlin C, Murray GI. Current and emerging concepts in tumour metastasis. *J Pathol*. 2010;222(1):1-15. doi:10.1002/path.2727.

149. Wang N, Zhan T, Ke T, et al. Increased expression of RRM2 by human papillomavirus E7 oncoprotein promotes angiogenesis in cervical cancer. *Br J Cancer*. 2014;110(4):1034-44. doi:10.1038/bjc.2013.817.

150. Stone SC, Rossetti RAM, Lima AM, Lepique AP. HPV associated tumor cells control tumor microenvironment and leukocytosis in experimental models. *Immunity, Inflamm Dis*. 2014;2(2):63-75. doi:10.1002/iid3.21.

151. Bauerschmitz GJ, Kanerva A, Wang M, et al. Evaluation of a selectively oncolytic adenovirus for local and systemic treatment of cervical cancer. *Int J Cancer*. 2004;111(2):303-309. doi:10.1002/ijc.20217.

152. Takahashi K, Saga Y, Mizukami H, et al. Development of a mouse model for lymph node metastasis with endometrial cancer. *Cancer Sci*. 2011;102(12):2272-2277. doi:10.1111/j.1349-7006.2011.02099.x.

153. Yamagata Y, Parietti V, Stockholm D, et al. Lentiviral Transduction of CD34+ Cells Induces Genome-Wide Epigenetic Modifications. *PLoS One*. 2012;7(11). doi:10.1371/journal.pone.0048943.

154. Mountain CF, Dresler CM. Regional lymph node classification for lung cancer staging. *Chest*. 1997;111(6):1718-1723. doi:10.1378/chest.111.6.1718.

155. Smith JA, Whitmore WF. Regional lymph node metastasis from bladder cancer. *J Urol*. 1981;126(5):591-593.

156. Wittekind C. Diagnosis and staging of lymph node metastasis. *Recent Results Cancer Res*. 2000;157:20-28.

157. Langley RR, Fidler IJ. Tumor cell-organ microenvironment interactions in the pathogenesis of cancer metastasis. *Endocr Rev*. 2007;28(3):297-321. doi:10.1210/er.2006-0027.

158. Sleeman JP. The lymph node as a bridgehead in the metastatic dissemination of tumors. *Recent Results Cancer Res*. 2000;157:55-81. doi:10.1007/978-3-642-57151-0_6.

159. Wong SY, Hynes RO. Lymphatic or hematogenous dissemination: How does a metastatic tumor cell decide? *Cell Cycle*. 2006;5(8):812-817. doi:10.4161/cc.5.8.2646.

160. Wong SY, Haack H, Crowley D, Barry M, Bronson RT, Hynes RO. Tumor-secreted vascular endothelial growth factor-C is necessary for prostate cancer lymphangiogenesis, but lymphangiogenesis is unnecessary for lymph node metastasis. *Cancer Res*. 2005;65(21):9789-9798. doi:10.1158/0008-5472.CAN-05-0901.

161. Vaupel P, Harrison L. Tumor hypoxia: causative factors, compensatory mechanisms, and cellular response. *Oncologist*. 2004;9 Suppl 5:4-9. doi:10.1634/theoncologist.9-90005-4.

162. Yu YA, Shabahang S, Timiryasova TM, et al. Visualization of tumors and metastases in live animals with bacteria and vaccinia virus encoding light-emitting proteins. *Nat Biotechnol*. 2004;22(3):313-320. doi:10.1038/nbt937.

163. Unno Y, Shino Y, Kondo F, et al. Oncolytic viral therapy for cervical and ovarian cancer cells by sindbis virus AR339 strain. *Clin Cancer Res*. 2005;11(12):4553-4560. doi:10.1158/1078-0432.CCR-04-2610.

164. Kim JH, Lee YS, Kim H, Huang JH, Yoon AR, Yun CO. Relaxin expression from tumor-targeting adenoviruses and its intratumoral spread, apoptosis induction, and efficacy. *J Natl Cancer Inst*. 2006;98(20):1482-1493. doi:10.1093/jnci/djj397.

165. Parato KA, Breitbach CJ, Le Boeuf F, et al. The Oncolytic Poxvirus JX-594 Selectively Replicates in and Destroys Cancer Cells Driven by Genetic Pathways Commonly Activated in Cancers. *Mol Ther*. 2012;20(4):749-758. doi:10.1038/mt.2011.276.

166. Willard-Mack CL. Normal structure, function, and histology of lymph nodes. *Toxicol Pathol*. 2006;34(5):409-424. doi:10.1080/01926230600867727.

167. Sánchez-Puig JM, Sánchez L, Roy G, Blasco R. Susceptibility of different leukocyte cell types to Vaccinia virus infection. *Virol J*. 2004;1:10. doi:10.1186/1743-422X-1-10.

168. Smith GL, Benfield CTO, Maluquer de Motes C, et al. Vaccinia virus immune evasion: Mechanisms, virulence and immunogenicity. *J Gen Virol*. 2013;94(PART 11):2367-2392. doi:10.1099/vir.0.055921-0.

169. Okamoto Y, Ohwaki T, Kawase S, et al. Inhibition of growth and pulmonary metastasis of B16-F10 murine melanoma by N-1554, a polyprenyl phosphate. *Cancer Lett*. 1991;57(2):159-163. doi:10.1016/0304-3835(91)90210-9.

170. Chen NG, Yu YA, Zhang Q, Szalay AA. Replication efficiency of oncolytic vaccinia virus in cell cultures prognosticates the virulence and antitumor efficacy in mice. *J Transl Med*. 2011;9(1):164. doi:10.1186/1479-5876-9-164.

171. Ohira T, Ohe Y, Heike Y, et al. In vitro and in vivo growth of B16F10 melanoma cells transfected with interleukin-4 cDNA and gene therapy with the transfectant. *J Cancer Res Clin Oncol*. 1994;120(11):631-635.

172. Patel N, Diven D. Vaccinia - Medscape Reference. *Medscape- Drug Dis*. 2012.

173. Kim SY, Kim MK, Kwon SB, Na JI, Park KC, Kim DS. Tumor apoptosis by indole-3-acetic acid/light in B16F10 melanoma-implanted nude mice. *Arch Dermatol Res*. 2009;301(4):319-322. doi:10.1007/s00403-009-0938-6.

174. Nicolson GL, Brunson KW, Fidler IJ. Specificity of arrest, survival, and growth of selected metastatic variant cell lines. *Cancer Res*. 1978;38(11 II):4105-4111.

175. Thody AJ, Higgins EM, Wakamatsu K, Ito S, Burchill SA, Marks JM. Pheomelanin as well as eumelanin is present in human epidermis. *J Invest Dermatol*. 1991;97(2):340-344. doi:10.1111/1523-1747.ep12480680.

176. Ito S, Jimbow K. Quantitative analysis of eumelanin and pheomelanin in hair and melanomas. *J Invest Dermatol*. 1983;80(4):268-272. doi:10.1111/1523-1747.ep12534616.

7 Appendix

7.1 Abbreviations

°C	degree Celsius
%	Percent
α	anti; alpha
β	beta
µ	micro
AN	axillary lymph node
approx.	approximately
BN	brachial lymph node
bp	base pairs
cDNA	complementary desoxyribonucleic acid
CEV	cell-associated enveloped virus
cm	centimeter
CMC	carboxymethylcellulose
CPE	cytopathic effect
CSC	cancer stem cells
DMSO	dimethyl sulfoxide
DNA	desoxyribonucleic acid
dNTP	deoxynucleoside triphosphates
dpi	days post injection
dpti	days post tumor implantation
ECM	extracellular matrix
EDTA	diaminoethanetetraacetic acid
EEV	extracellular enveloped virus
EMT	epithelial-mesenchymal transition
EU	European Union
f.p.	footpad
FCS	fetal calf serum
FDA	Food and Drug Administration
FIGO	Federation of Gynecology and Obstetrics
FSC	forward scatter

GAG	glucosoaminoglycan
GFP	green fluorescence protein
gusA	β-Glucuronidase
h	hour; human
HA	hemagglutinin
hpi	hours post infection
HPV	*human papilloma virus*
i.t.	intratumoral
i.v.	intravenous
IEV	intracellular enveloped virus
IL	interleukin
IMV	intracellular mature virus
IN	inguinal lymph node
kbp	kilo base pairs
lacZ	β-Galaktosidase
LN	lumbar lymph node
m	murine
mA	milli ampere
MALT	mucosa-associated lymphoid tissue
MCSC	migrating cancer stem cells
MET	mesenchymal-epithelial transition
min	minute
mm	millimeter
MOI	multiplicity of infection
mRNA	messenger ribonucleic acid
NK	natural killer
nm	nanometer
OC	oral contraceptives
PCR	polymerase chain reaction
PFA	paraformaldehyde
pfu	plaque forming units
PN	popliteal lymph node
RFP	red fluorescence protein
RN	renal lymph node

RNA	ribonucleic acid
ROS	reactive oxygen species
rpm	rounds per minute
RT	room temperature
RT-PCR	reverse transcriptase polymerase chain reaction
RUC-GFP	Renilla luciferase-*Aequorea* green fluorescence protein
rVACV	recombinant vaccinia virus
s.c.	subcutaneous
SCSC	stationary cancer stem cells
sec	second
siRNA	small interfering RNA
SN	sacral lymph node
SSC	side scatter
TFR	transferrin receptor
TK	thymidine kinase
TNM	tumor thickness, number of regional lymph nodes, distant
UV	ultraviolet
UVR	ultraviolet radiation
WHO	World Health Organization

7.2 Danksagung

An dieser Stelle möchte ich die Gelegenheit nutzen mich bei allen zu bedanken, die zu der Entstehung meiner Doktorarbeit beigetragen und mich in den letzten drei Jahren unterstützt haben.

Als erstes möchte ich mich bei Prof. Dr. Aladar Szalay bedanken, dass er mich in seine Arbeitsgruppe in Würzburg aufgenommen hat, mir einen kreativen Freiraum in der Forschung gewährt hat und mir die Möglichkeit gegeben hat, an diesem interessanten Thema zu arbeiten.

Des Weiteren danke ich Prof. Dr. Frieder Grummt für das Korrekturlesen und sein Interesse an meiner Arbeit. Mit seiner konstruktiven Kritik hat er sehr beim Entstehen dieser Arbeit geholfen.

Außerdem gilt mein Dank Prof. Dr. Thomas Dandekar für die Übernahme des Zweitgutachtens dieser Arbeit.

Darüber hinaus möchte ich Herrn Prof. Dr. Fischer und den Mitarbeitern des Lehrstuhls für Biochemie danken, besonders auch Frau Dambach für die Unterstützung in allen organisatorischen Dingen.

Ein ganz großes Dankeschön gilt der gesamten Arbeitsgruppe Szalay in Würzburg, für die viele Hilfe und Unterstützung, die ich von euch erhalten habe. In erster Linie danke ich hier meiner Betreuerin Dr. Ulrike Donat, die mir das spannende Feld der Metastasen eröffnet hat und mich in meiner Anfangszeit eingearbeitet hat. Ein besonderer Dank gilt Dr. Barbara Härtl für die große Hilfe und Unterstützung, und dass sie immer Zeit und gute Ratschläge für mich hatte. Ein großer Dank gilt auch Johanna und ihrem Organisationstalent, für alles was sie im Labor und darüber hinaus für uns macht. Auch für die zahlreichen Stunden die wir zusammen am Kryotom verbracht haben. Meiner Mitdoktorandin Christina danke ich für die gegenseitige Unterstützung, die konstruktiven Gespräche und natürlich für die gemeinsam verbrachten Zumbastunden. Des Weiteren danke ich Barbara, Johanna und Christina für eine Freundschaft weit über das Labor hinaus. Lorenz möchte ich danken für die Gespräche über Melanin und die gute Laune die er immer verbreitet hat. Auch Ivo und Marion möchte ich für die wissenschaftlichen Gespräche und Ratschläge danken. Darüber hinaus möchte ich mich noch

ganz herzlich bei Tanja bedanken, die immer ein offenes Ohr für Sorgen und Probleme hatte und sich immer für uns eingesetzt hat.

Außerdem möchte ich Frau Kaiser stellvertretend für das Zentrale Frauenbüro der Universität Würzburg danken, für die Vergabe eines Stipendiums, welches mir die Beendigung meiner Doktorarbeit ermöglicht hat.

Zum Schluss gilt ein ganz besonderer Dank meiner Familie, meinen Freunden und meinem Mann, der immer viel Geduld mit mir hatte und mich die letzten Jahre immer unterstützt und motiviert hat.

7.3 Eidesstattliche Erklärung

Erklärung gemäß § 4 Absatz 3 der Promotionsordnung der Fakultät für Biologie der Julius-Maximilians-Universität Würzburg:

Hiermit versichere ich, dass ich die vorliegende Dissertation selbstständig und nur mit den angegebenen Hilfsmitteln und Quellen angefertigt habe.

Ich erkläre weiterhin, dass diese Dissertation weder in gleicher noch in anderer Form bereits in einem anderen Prüfungsverfahren vorgelegt wurde.

Neben den akademischen Graden „Bachelor of science“ und „Master of science“ habe ich keine weiteren akademischen Grade erworben oder zu erwerben versucht.

Würzburg, den _____ _____

(Juliane Meir)

7.4 Lebenslauf

7.5 Publikationsliste

Donat U*, Rother J*, Schäfer S, Hess M., Härtl B., Kober C., Langbein-Laugwitz J., Stritzker J., Chen N., Aguilar R., Weibel S., Szalay A.

Characterization of metastasis formation and virotherapy in the human C33A cervical cancer model. *PLoS One*. 2014;9(6):e98533. doi:10.1371/journal.pone.0098533.

*contributed equally